

NASA Contractor Report 4047  
DOT/FAA/PM-86/50, II

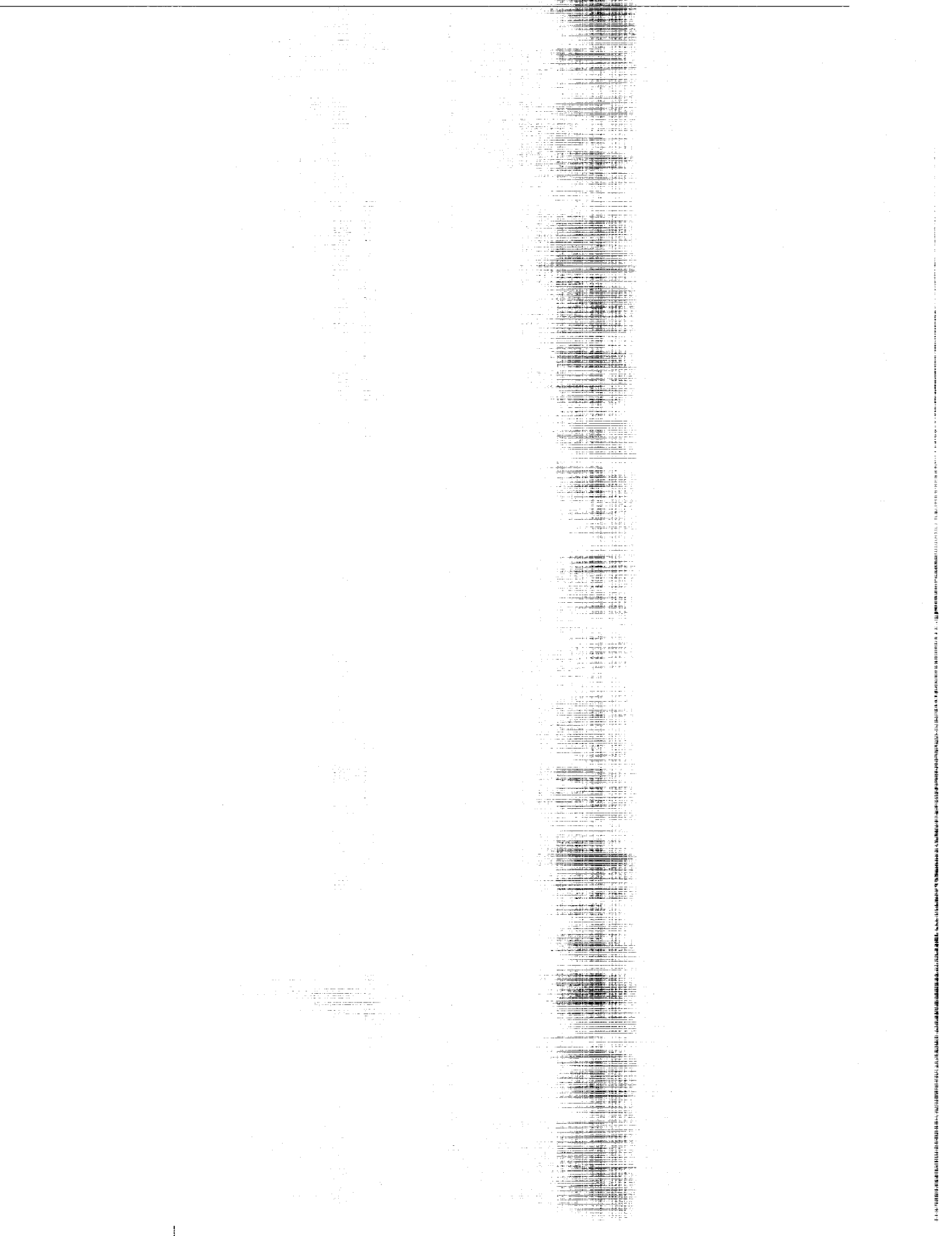
# The Terminal Area Simulation System

*Volume II: Verification Cases*

F. H. Proctor

CONTRACT NAS1-17409  
APRIL 1987





NASA Contractor Report 4047  
DOT/FAA/PM-86/50, II

# The Terminal Area Simulation System

## *Volume II: Verification Cases*

F. H. Proctor  
*MESO, Inc.*  
*Hampton, Virginia*

Prepared by MESO, Inc., under subcontract  
to ST Systems Corporation (STX)  
for NASA Langley Research Center and  
the U.S. Department of Transportation,  
Federal Aviation Administration  
under Contract NAS1-17409

**NASA**  
National Aeronautics  
and Space Administration

Scientific and Technical  
Information Branch

1987



TABLE OF CONTENTS

1. INTRODUCTION .....	1
2. CASE I: CCOPE SUPERCELL HAILSTORM .....	8
Initial Conditions for Case I .....	8
Results From Case I .....	9
Summary and Conclusions for Case I .....	20
3. CASE II: SMALL CCOPE CUMULONIMBUS .....	24
Initial Conditions for Case II .....	24
Results for Case II .....	25
Summary for Case II .....	36
4. CASE III: DALLAS MICROBURST .....	39
Initial Conditions for Case III .....	39
Results for Case III .....	40
Summary for Case III .....	59
5. CASE IV: SOUTH FLORIDA CONVECTIVE COMPLEX .....	61
Initial Conditions for Case IV .....	61
Results for Case IV .....	62
Summary for Case IV .....	68
6. CASE V: OKLAHOMA TORNADIC THUNDERSTORM .....	72
Initial Conditions for Case V .....	73
Results for Case V .....	75
Summary for Case V .....	85

7. SUMMARY AND CONCLUSIONS .....	86
ACKNOWLEDGMENTS .....	90
REFERENCES .....	91

LIST OF TABLES

Table 1. Initial Specifications of Each of the Verification Cases .... 5

LIST OF FIGURES

Fig. 1. Skew-T diagram depicting temperature and dew point profiles observed at Knowlton, Montana on 2 August 1981 at 17:46 MDT. Winds plotted at model height levels. Each full wind-speed barb represents  $5 \text{ m s}^{-1}$ ..... 10

Fig. 2. Three-dimensional perspectives viewed from the southeast for Case I. Simulated clouds at times (a) 220 min, (b) 170 min, (c) 190 min, (d) 200 min, (e) 210 min, (f) 215 min, and (g) 240 min. Simulated hail region at (h) 200 min and (i) 220 min. The vertical dimension is in  $z'$  space. The horizontal area is windowed to 40 km x 40 km. The cloud perspectives are defined by the cloud droplet water and cloud ice crystal fields..... 12

Fig. 3. Schematic view of a tornadic supercell thunderstorm (copied from the National Weather Service Storm Spotter's Glossary and Supplemental Guide)..... 13

Fig. 4. Simulated horizontal cross section of wind vector field (ground relative) at 240 m AGL for Case I. The downdraft centers are designated by  $\odot$  ..... 15

Fig. 5. Horizontal cross section of simulated wind vector field (storm relative) and radar reflectivity at 3.5 km AGL for Case I. The contour interval is 5 dBZ..... 16

Fig. 6.	Observed radar reflectivity at approximately 4 km AGL. The contours start at 10 dBZ and increment by 10 dBZ. (Modified from Miller, 1985) .....	17
Fig. 7.	Vertical west-east cross sections of simulated radar reflectivity and storm relative wind field for Case I. The contour interval for radar reflectivity is 10 dBZ.....	18
Fig. 8.	Same as Fig. 7 but observed radar reflectivity and Doppler-derived wind field. The radar reflectivity contours start at 10 dBZ and increment by 10 dBZ. (From Miller, 1985) .....	19
Fig. 9.	Simulated vertical cross sections of equivalent potential temperature for Case I. The cross sections are (a) east-west and (b) north-south through the core of the storm updraft. The contour interval is 2°C. Contours having values greater than 400 K are not plotted.....	21
Fig. 10.	Same as Fig. 1 but observed at Miles City, Montana on 19 July 1981 at 1440 MDT.....	26
Fig. 11.	Model input sounding for Case II. Modified from Fig. 10 to agree with observed cloud-base temperature and pressure.....	27
Fig. 12.	Simulated maximum radar reflectivity at a given time and height above the ground for Case II. The contour interval is 10 dBZ.....	28

Fig. 13.	Simulated maximum vertical velocity (upper) and minimum vertical velocity (lower) at a given time and height above the ground for Case II. The contour interval is $2 \text{ m s}^{-1}$ .....	29
Fig. 14.	Simulated west-east vertical cross section of radar reflectivity and storm-relative vector wind field at 40 minutes for Case II. The contour interval for radar reflectivity is 10 dBZ.....	30
Fig. 15.	Same as Fig. 14 but for equivalent potential temperature. The contour interval is $1^{\circ}\text{C}$ .....	32
Fig. 16.	Simulated horizontal field of radar reflectivity in Case II at 6.1 km MSL (5.3 km AGL). Contour intervals are 1, 10, 25, 40, and 50 dBZ.....	33
Fig. 17.	Observed reflectivity from radar PPI sweep at 1939:11 MDT. Each tick mark represents 1 km. The solid contours start at -5 dBZ and increase by steps of 15 dBZ (from Dye et al., 1986).....	34
Fig. 18.	Maximum radar reflectivity at a given time and altitude: (a) observed (from Dye et al., 1986); (b) simulated. Contour interval is 10 dBZ.....	35
Fig. 19.	Simulated three-dimensional cloud perspectives at 20, 30, 35, 40, 50, and 60 min for Case II. Perspectives are viewed from northeast and do not include precipitation.....	37

Fig. 20.	Same as Fig. 1, but observed at Stephenville, Texas on 2 August 1985 at approximately 1800 CDT.....	41
Fig. 21.	Model input sounding for DFW on 2 August 1985 at 1800. Obtained from MASS preprocessor (see text).....	42
Fig. 22.	Simulated radar reflectivity for Case III at 3 km AGL at (a) 30 min and (b) 37 min. The contour interval is 10 dBZ.....	43
Fig. 23.	A sequence of radar photos from Stephenville radar (from Fujita, 1986).....	44
Fig. 24.	South-north vertical cross section of the simulated radar reflectivity at 30 min for Case III. The contours begin at 10 dBZ and increment by 10 dBZ.....	45
Fig. 25.	Simulated low-level vector field for Case III at (a) 28 min and (b) 30 min.....	47
Fig. 26.	Same as Fig. 25, but at (a) 31 min and (b) 32 min.....	48
Fig. 27.	Same as Fig. 25, but at (a) 34 min and (b) 37 min.....	49
Fig. 28.	Deviation of temperature from environment at 100 m AGL and 37 min. Contour interval is 0.5°C.....	51

Fig. 29.	Diameter of outflow at the ground as a function of time. Model data represented by squares. Solid circles represent estimated diameter of DFW microburst as computed from Fig. 5.9 in Fujita (1986).....	52
Fig. 30.	Distance from the initial microburst center to the southern- most boundary of the outflow as a function of time. Symbols same as in Fig. 29.....	54
Fig. 31.	South-north vertical cross section of the simulated wind vector field at 30 min for Case III. The thick curve outlines the 10 dBZ radar reflectivity contour, while the thin curve outlines $0.2 \text{ g m}^{-3}$ rainwater contour.....	55
Fig. 32.	Same as Fig. 31, but the field is for hail water. The contour interval is $0.2 \text{ g m}^{-3}$ of hail water.....	57
Fig. 33.	The horizontal cross section of the simulated deviation pressure at 100 m AGL and 28 min for Case III. The contour interval is 0.1 mb.....	58
Fig. 34.	Same as Fig. 1, but observed at Field Observing Site (FOS) in FACE network at 1345 EDT on 25 August 1975. Winds above 825 mb level taken from Miami 0800 EDT sounding.....	63
Fig. 35.	Simulated radar reflectivity at 33 min for Case IV. The fields are (a) horizontal cross section at 2 km AGL and (b) vertical north-south cross section at $x = -6.4$ . The contours begin at 10 dBZ and increment by 10 dBZ.....	64

Fig. 36. The radar reflectivity of cell observed in FACE network. Contours are 10, 20, 30, 40, 45, and 50 dBZ (taken from Cunning et al., 1986).....	65
Fig. 37. Same as Fig. 25, but for Case IV at 33 min.....	67
Fig. 38. Same as Fig. 19, but for Case IV at 40, 43, and 45 min. Perspectives viewed from southeast. The horizontal area is windowed to 40 km x 40 km.....	69
Fig. 39. Simulated north-south vertical cross sections of vertical velocity (left) and radar reflectivity (right) for Case IV. The top, middle, and bottom rows are taken at 40, 43, and 45 min, respectively. The contour interval for vertical velocity is $1 \text{ m s}^{-1}$ with negative values dashed, and the contours for radar reflectivity start at 10 dBZ and increment by 10 dBZ.....	70
Fig. 40. Composite sounding for Del City, Oklahoma on 20 May 1977. Above 444 m AGL, composite winds taken from Fig. 3 in Klemp et al. (1981). Below 444 m, winds taken from mean tower data presented in Fig. 1 of Johnson (1985).....	74
Fig. 41. Simulated radar reflectivity at 100 min and 1.5 km AGL for Case V. Area windowed to 30 km x 30 km. Contour interval is 5 dBZ.....	76

Fig. 42.	Three dimensional perspectives of the precipitation field within the modeled and observed storms as viewed from the southeast. The perspectives are (a) TASS model simulation, (b) Del City observed at 1833 CST, (c) Del City observed at 1847 CST, and (d) Klemp et al. (1981) model simulation. The contoured surfaces in (a)-(c) represent the 35 dBZ surface and in (d) represent the 0.5 g/kg rainwater surface. Figs. b-d are from Klemp et al. (1981) .....	78
Fig. 43.	Simulated low-level contour fields and superimposed wind vectors at 170 min for (a) vertical velocity and storm relative wind vectors, and (b) vertical vorticity and ground relative wind vectors for Case V. Area windowed to 6 km x 6 km. The contour interval for (a) is $0.5 \text{ m s}^{-1}$ , and (b) is $5 \times 10^{-2} \text{ s}^{-1}$ . Negative values contoured with a negative line. Labels in (b) scaled by a factor of 100.....	79
Fig. 44.	Simulated time history of peak 10 dBZ radar reflectivity heights (thick curve) and peak low-level vertical vorticity (thin curve) for Case V.....	81
Fig. 45.	Relative positions of simulated gust fronts at 120, 140, and 160 min in Case V.....	83
Fig. 46.	Same as Fig. 41, but at 3.5 km AGL and at (a) 100 min and (b) 120 min.....	84

## ABSTRACT

The numerical simulation of five case studies are presented and are compared with available data in order to verify the three-dimensional version of the Terminal Area Simulation System (TASS). A spectrum of convective storm types are selected for the case studies. They are: (1) a High-Plains supercell hailstorm, (2) a small and relatively short-lived High-Plains cumulonimbus, (3) a convective storm which produced the 2 August 1985 DFW microburst, (4) a South Florida convective complex, and (5) a tornadic Oklahoma thunderstorm. For each of the cases the model results compared reasonably well with observed data. In the simulations of the supercell storms many of their characteristic features were modeled, such as the hook echo, BWER, mesocyclone, gust fronts, giant persistent updraft, wall cloud, flanking-line towers, anvil and radar reflectivity overhang, and rightward veering in the storm propagation. Also in the simulated supercell storms, heavy precipitation including hail fell to the west and north of the storm updraft. In the simulation of the tornadic storm a horseshoe-shaped updraft configuration and cyclic changes in storm intensity and structure were noted. The simulation of the DFW microburst agreed remarkably well with sparse observed data. The simulated outflow rapidly expanded in a nearly symmetrical pattern and was associated with a ring vortex. A South Florida convective complex was simulated and contained updrafts and downdrafts in the form of discrete bubbles.

The numerical simulations, in all cases, always remained stable and bounded with no anomalous trends.



## 1. INTRODUCTION

The Terminal Area Simulation System (TASS) is a three-dimensional numerical cloud model which has been developed for the general purpose of studying atmospheric convection. Potential applications of the model range from the simulation of shallow cumulus to intense supercell cumulonimbus, including convective phenomena such as downbursts, gust fronts, hailstorms, and tornadoes. The TASS numerical model contains governing equations for momentum, pressure, potential temperature, water vapor, cloud droplet water, rainwater, cloud ice-crystal water, snow, and hail. The model includes open and nonreflective lateral boundary conditions, a diagnostic surface boundary layer based on Monin-Obukhov similarity theory, conventional first-order subgrid turbulence closure, and numerous microphysical interactions computed by Orville-type parameterizations. The TASS formulation also contains an algorithm which allows the domain to translate (at a variable speed) with the propagation of the simulated convection. A detailed documentation of the TASS model formulation is contained in Proctor (1987) hereinafter referred to as VOLUME 1.

The primary purpose of this report, VOLUME II, is to evaluate the TASS model's capability and performance, and to compare the TASS simulated results against actual observations. For this purpose, five case experiments of cumulonimbus convection have been chosen. The selection of each case is based on both the availability of observed data and the type of cumulonimbus convection that was observed. At least some observed data is available for many case studies, be it Doppler radar analysis, conventional radar data, measurements from ground based instrumentation, satellite imagery, measurements from instrumented research aircraft, aircraft flight recorder data, visual photography, or visual sightings. Although, complete

and detailed observed data sets (including rawinsonde launchings) are quite rare through the lifetime of a convective cell. The availability of data is a prime consideration in the selection of each case.

Convective storms are usually categorized into three basic storm types: short-lived single cell (e.g., Byers and Braham, 1949), multicell (e.g., Marwitz, 1972a), and supercell (e.g., Browning, 1964; Marwitz, 1972b). The single cell storms have relatively short lifetimes of usually less than 45 min; while, in contrast, the supercell storms consist of a giant and intense quasi-steady updraft which may persist for several hours. Multicell storms may also last for long periods of time, but are made up of several short lived single cells, with new cells being continually generated as the older cells die. These three modes of convective storms may occur in isolation or grouped together in mesoscale complexes and squall lines. Cumulonimbus convection is further categorized according to the weather phenomena that it may produce, such as hail, tornadoes, strong low-level winds, and downbursts. One important objective of this verification study is to demonstrate that the TASS model can successfully simulate different types or modes of cumulonimbus convection with reasonable comparison to observations.

Fortunately, complex initial conditions are not necessary in order to simulate the various modes of convection. Numerical experiments by Weisman and Klemp (1982, 1984) point to two parameters, namely, vertical wind shear and convective instability, as being particularly important in influencing cumulonimbus structure and evolution. For example, a combination of strong wind shear and strong convective instability favors supercell convection, while weak wind shear favors single cell convection. Thus, in many events, the evolution and structure of a convective storm is determined by its ambient vertical profiles of temperature, humidity, and wind speed and

direction. Other factors such as strong mesoscale features, terrain, and the presence of nearby cells, also affect storm structure and are less easy to incorporate in a cloud model. And as pointed out by Tripoli and Cotton (1986), storm structure in weak wind-shear cases is more dependent on how the cell was initiated. We therefore expect isolated supercell convection to be the easiest to verify (unless it is associated with intense mesoscale features); since in these cases, the storm structure and evolution is strongly determined by the vertical ambient profile. But less successful verification is expected in weak vertical wind-shear conditions. In these cases the observed convection is more likely to be influenced by weak to moderately intense mesoscale features, and the model convection is likely to be strongly affected by the initialization procedure.

The five cases that are chosen for the verification experiments are: (1) CCOPE Supercell Hailstorm -- which occurred in southeastern Montana on 2 August 1981; (2) Small CCOPE Cumulonimbus -- an isolated and relatively short-lived storm which also occurred in southeastern Montana, but on 19 July 1981; (3) Dallas Microburst -- an intense but relatively small thunderstorm on 2 August 1985; this storm produced an intense low-level wind shear which was a contributing factor in a commercial aircraft disaster; (4) South Florida Convective Complex -- a multicell storm which occurred on 25 August 1975; and (5) Oklahoma Tornadic Thunderstorm -- one of several tornadic supercell storms occurring on 20 May 1977. All of the above cases have been well documented and should give a good spectrum of convective storm types, which can be used to test and verify the realism of the TASS model.

In specifying the initial conditions, I have tried to minimize the changes in model parameters between each case. No attempt is made to

empirically adjust model parameters for a specific case, so as to obtain desired results. The model parameters which do vary between each case are: the coriolis parameter, the number concentration of cloud droplets ( $n_{CD}$ ), the dispersion coefficient for the cloud droplet spectrum ( $\sigma$ ), the horizontal radius of the initial thermal perturbation ( $R_0$ ), the peak magnitude of the initial thermal impulse ( $\Delta T$ ), and the peak magnitude of the initial velocity impulse ( $W_{max}$ ). The functions of each of these parameters are discussed in VOLUME I. The coriolis parameter is determined from the appropriate latitude in each of the case studies. The specific values of the other initial parameters, the dimensions of the modeled domain, the horizontal grid size, and the number of vertical levels (NL), for each of the five cases are shown in Table 1. Cumulus convection is triggered in each of the five cases by specifying an initial thermal or velocity impulse within an otherwise horizontally homogeneous domain. The radius for the initial impulse is set equal to 10 km in the cases having strong ambient wind shear, and 2.5 km in the cases having weak vertical wind shear. The assumed values are sufficiently large so as to trigger convection; and as already mentioned, the specification of the initial impulse may have some bearing on the convective structure in weakly-sheared environments. An extensive study of the sensitivity of each of the initial parameters has not yet been undertaken. The initial velocity impulse, which has the same horizontal dimensions of the initial thermal impulse, is applied only in Case V; prototype experiments have shown that the major effect of the velocity impulse is to slightly speed up the model cloud development. Details of the general initialization procedure can be found in VOLUME I. In the microphysics the only constants that are varied between each case

TABLE 1. INITIAL SPECIFICATIONS OF EACH OF THE VERIFICATION CASES

(See text for definition of symbols)

Case	Description	Domain size X × Y × Z (km)	Horizontal grid size (m)	Vertical layers NL	$n_{CD3}$ (#/m <sup>3</sup> )	$\sigma$	$R_{\theta}$ (m)	$\Delta T$ (°C)	$W_{max}$ (m/s)
I	CCOPE Supercell Hailstorm*	60 × 60 × 17.5	1000	31	$1000 \times 10^6$	0.15	10,000	3	0
II	Small CCOPE Cumulonimbus	10 × 10 × 12	250	27	$600 \times 10^6$	0.2	2,500	1.5	0
III	Dallas Microburst	12 × 12 × 18	200	31	$300 \times 10^6$	0.3	2,500	1.5	0
IV	South Florida Convective Complex	15 × 15 × 16	250	31	$100 \times 10^6$	0.35	2,500	1.5	0
V	Oklahoma Tornadoic Thunderstorm	45 × 45 × 18	750	31	$300 \times 10^6$	0.3	10,000	1.5	3

\*This experiment was conducted with an earlier version of the TASS model which did not include a production term for hail due to riming of snow.

experiment are  $n_{CD}$  and  $\sigma$ . Their values which are listed in Table 1 are based on actual observations or climatology of the specific location (e.g., maritime vs. continental). The size of the modeled domain for each of the cases is specified large enough to encompass the convective storm, but small enough to allow the best resolution (smallest grid size) possible. In all of the cases the vertical coordinate is stretched. The surface roughness parameter ( $z_0$ ) is not listed in Table 1, since it has a constant value of 10 cm in all of the cases. Microphysical parameters not listed in Table 1, such as the rain, hail, and snow intercepts, are not changed from their assigned values in VOLUME I.

Case I has been previously reported in Proctor (1985b), and was simulated with an earlier version of TASS model which did not contain a term for the production of hail due to the riming of snow. This term is included in the other four cases. Case I and the impact of omitting this production term for hail are further discussed in Chapter 2.

In assuming these five cases and comparing the simulated results with available data, we hope to verify the TASS model by asking:

- (1) Can the TASS model successfully simulate different modes or types of cumulonimbus convection? Are the characteristic features of each storm type captured in the model simulation?
- (2) How accurate are the storm fields simulated? Are the simulated fields consistent with observed data both aloft and near the ground?
- (3) Is hail simulated at the ground when it is actually observed? Does the model not simulate hail at the ground when it is not observed?

- (4) When simulating severe storms, can associated severe phenomena, such as downbursts, strong winds, and tornadoes, be simulated?
- (5) Does the model simulate the direction and speed of storm propagation correctly?
- (6) Is the orientation and speed of propagation correct for the storm induced gust fronts?
- (7) Does the model properly simulate the duration and life cycles of cumulonimbus convection? Are there any periodic tendencies or trends in the simulation of long-duration storms?
- (8) How do simulations with the TASS model compare to simulations with other numerical models?
- (9) How stable is the TASS model; does it remain numerically stable for long integrations? Are there any anomalous trends, such as in the pressure deviation field? Do the simulated results diverge from the observed data as the lifetime of the storm increases? Do the fields always remain bounded?

With the selection of the five named cases, this report will try to answer these questions.

In the next five chapters each of the case studies are discussed and compared with available observations. Each chapter is devoted to one case and first begins with an observational summary of that particular case; this is followed by a description of the model initial conditions, and then a discussion of the model results and comparisons with observations. Finally, each chapter concludes with a brief case summary. The general summary and conclusions of this model verification study is contained in the final chapter of this report.

## 2. CASE I: CCOPE SUPERCELL HAILSTORM

On 2 August 1981, a very large and severe hailstorm, whose lifetime exceeded 5 hours, moved across southeastern Montana. The storm was observed during its mature phase with Doppler radars, aircraft, and a dense network of field instruments as it moved through the Cooperative Convective Precipitation Experiment (CCOPE) network (Knight, 1982). Miller (1985) and Knight et al. (1985) have reported that the hailstorm exhibited many of the features typical of supercell storms. The hailstorm possessed an intense quasi-steady updraft with cyclonic rotation, a low-level radar hook echo appendage, and a mid-level radar vault coincident with the updraft. The storm veered right during the early stages of its lifetime and afterwards maintained a nearly continuous propagation to the right of the mean tropospheric wind. During this time it produced a broad swath of 1-3 cm diameter hail, with some sizes as large as 10 cm. Weisman et al. (1983b) reported that the storm produced at least one funnel cloud and that some damage reports were suggestive of tornadic activity.

The numerical simulation of this storm with the TASS model was reported in Proctor (1985b) and is summarized below. The version of the developing model used at that time did not include a term for the production of hail from the riming of snow (Eq. (69) in VOLUME I). The possible affect on the results due to the omission of this term are also discussed. [This term is included in the other four cases.]

### Initial Conditions for Case I

The initial conditions for this case (the CCOPE supercell hailstorm) are summarized in Table 1. The horizontal dimension of the domain is 60 km x 60 km and is resolved by a constant horizontal grid size of 1 km.

The depth of the domain is 17.5 km and is resolved vertically by 31 levels. The vertical grid size stretches with height and is given by Eq. (104) in VOLUME I, with  $C_1 = 0.168$ ,  $C_2 = 6.4 \times 10^{-6}$  m. This choice of parameters results in a vertical spacing which varies from approximately 240 m near the ground to approximately 900 m near the top boundary.

The reference environment is taken from the Knowlton, Montana, 17:46 MDT special sounding (Fig. 1). The sounding was observed when the hailstorm was roughly 80 km to the WNW (Wade, 1982). The only modification to the original sounding is a slight increase in boundary-layer moisture (from 12 g/kg to 13.5 g/kg), which is justified from surface measurements observed southeast of the hailstorm (see Wade, 1982).

#### Results From Case I

The simulated storm was triggered by a single 10 km radius temperature impulse. A cumulonimbus evolved with many characteristics of an actual supercell thunderstorm. The updraft of the storm approached maximum intensity within the first 30 minutes and was maintained throughout the 4 hour and 20 minute simulation. The propagation of the simulated storm after making a right turn at approximately 30 minutes was  $250^\circ$  to  $270^\circ$  at 8 to  $17 \text{ m s}^{-1}$ , which is to the right of the mean tropospheric wind ( $233^\circ$  at  $16.5 \text{ m s}^{-1}$ ). Before veering right, the average speed and direction of propagation was  $229^\circ$  at  $7.1 \text{ m s}^{-1}$ .

The modeled precipitation fields developed slowly with time. Autoconversion of cloud-droplet water into rain was ineffective due to the assumption of a continental cloud droplet spectrum (see Table 1). Rain was initially produced in the simulation by the melting of falling snow, and did not reach the ground until after 80 minutes. The simulation did produce

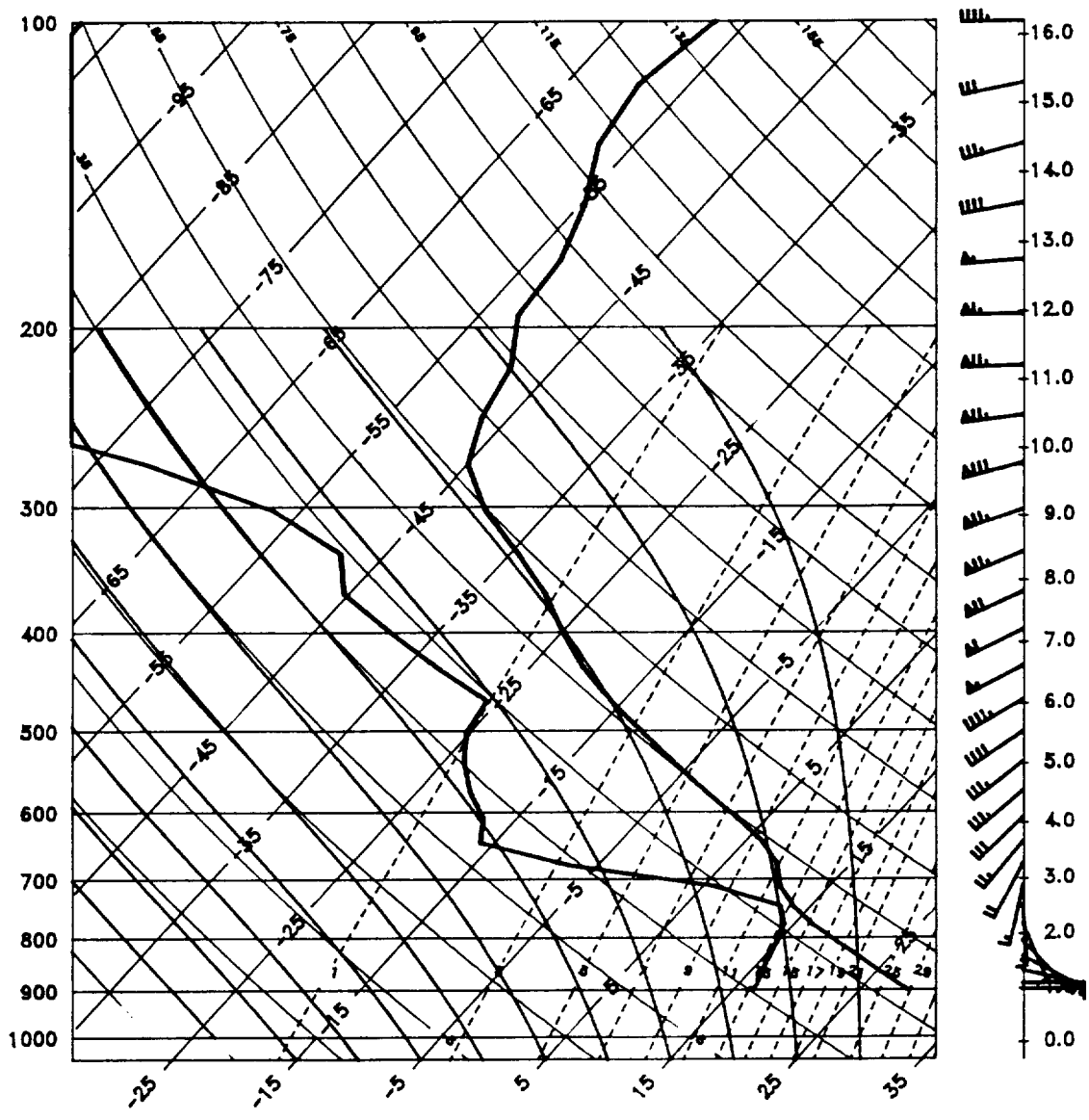


Fig. 1. Skew-T diagram depicting temperature and dew point profiles observed at Knowlton, Montana on 2 August 1981 at 17:46 MDT. Winds plotted at model height levels. Each full wind-speed barb represents  $5 \text{ m s}^{-1}$ .

hail, but it did not reach the ground until 160 minutes. The absence of the production term for hail due to snow riming may have contributed to the slow development of the hail field. A quasi-steady state was achieved in the simulation once the precipitation reached the ground. A well-defined hook echo and bounded weak echo region (BWER) (Chisholm, 1973) formed between 60 and 90 minutes and were maintained thereafter throughout the simulation.

Figure 2 shows three-dimensional perspectives of the cloud (Figs. 2a-2g) and hail (Figs. 2h and 2i) fields at various times in the simulation. The model was successful in simulating many of the visual features of a classic supercell. These include cumulus clouds along the flanking-line gust front (extending southwestward from the main storm tower) and a wall cloud with hail falling near its northern and western perimeter. [For comparison, a schematic view of a typical supercell thunderstorm is shown in Fig. 3.] The wall cloud developed after precipitation reached the ground and was maintained throughout the remainder of the simulation. Air within the wall cloud was found to have both temperatures and equivalent potential temperatures less than that of the environment -- indicating that downdraft air was being transported into the wall cloud. This is consistent with the explanation for wall-cloud development given by Rotunno and Klemp (1985).

Figure 4 shows the simulated low-level wind field and gust-front structure at 200 minutes. Note that the wind speeds are much greater (the vectors are longer) behind the flanking-line gust front than behind the forward-line gust front. The greatest low-level winds (in excess of  $20 \text{ m s}^{-1}$ ) occur behind the northern segment of the flanking-line gust front. The relative position of the flanking-line gust front agrees very well with Wade's (1982) analysis of the field measurements near the storm (see Wade's Fig. 9). Both observation and simulation agree that the flanking-line gust

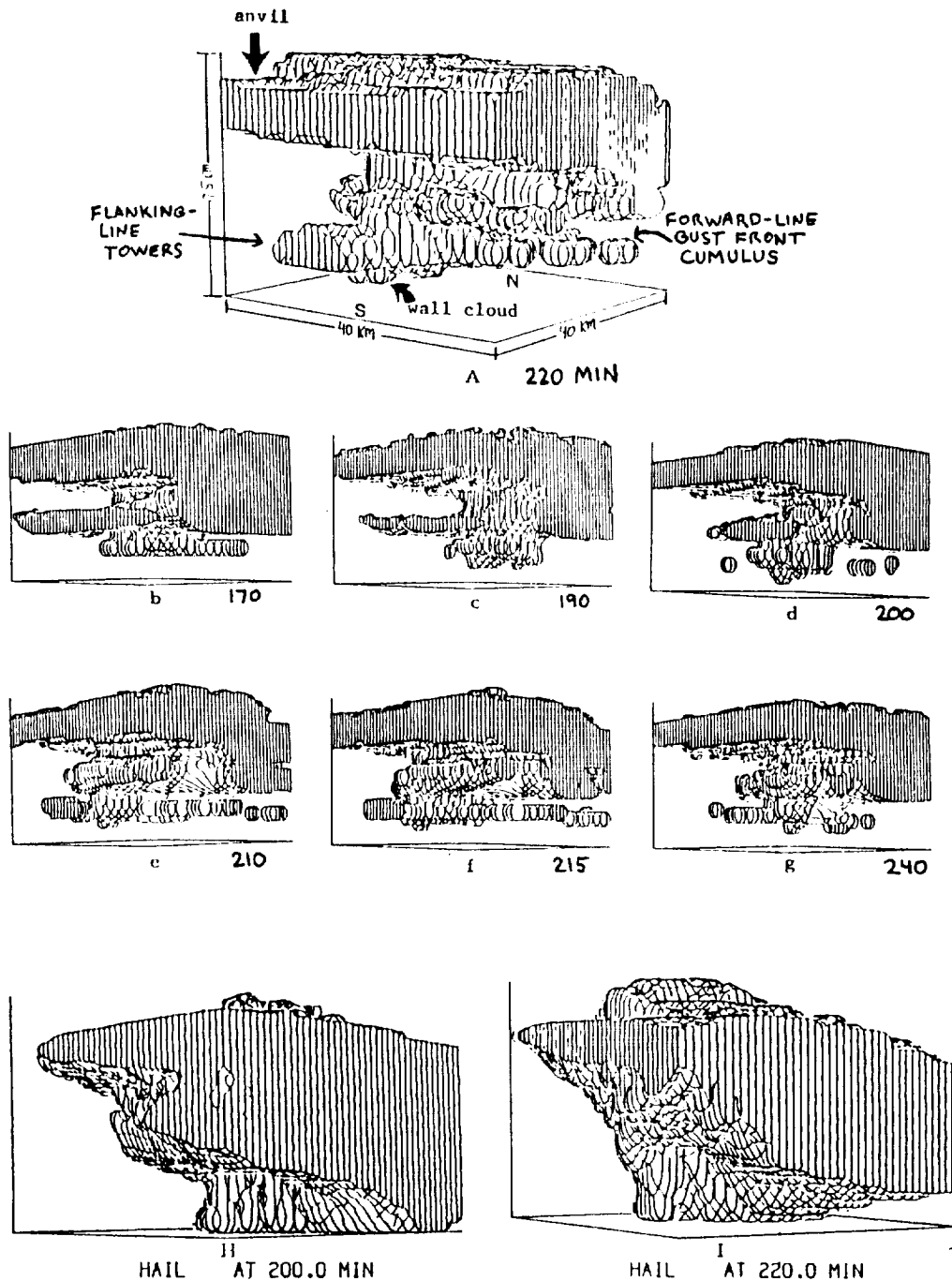


Fig. 2. Three-dimensional perspectives viewed from the southeast for Case I. Simulated clouds at times (a) 220 min, (b) 170 min, (c) 190 min, (d) 200 min, (e) 210 min, (f) 215 min, and (g) 240 min. Simulated hail region at (h) 200 min and (i) 220 min. The vertical dimension is in  $z'$  space. The horizontal area is windowed to  $40 \text{ km} \times 40 \text{ km}$ . The cloud perspectives are defined by the cloud droplet water and cloud ice crystal fields.

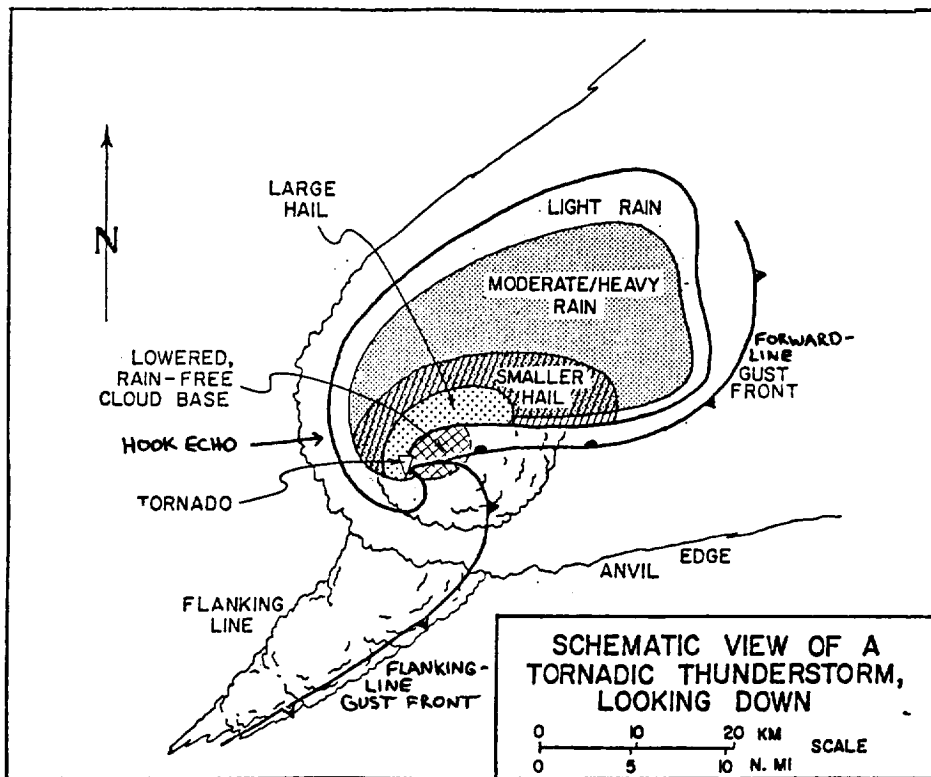
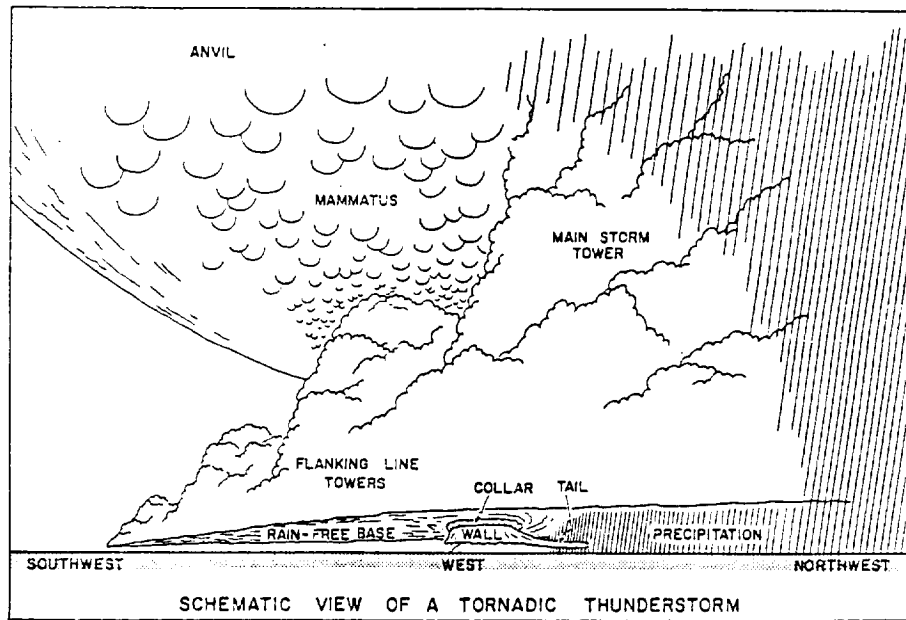


Fig. 3. Schematic view of a tornadic supercell thunderstorm (copied from the National Weather Service Storm Spotter's Glossary and Supplemental Guide).

Fig. 9). Both observation and simulation agree that the flanking-line gust front has a north-south orientation near its northern end, and then trails into a more east-west orientation away from the storm. Both observation and simulation also indicate strong winds behind the gust front and an apparent cold-frontal occlusion extending WNW from the point of occlusion. The gust front positions depicted in Fig. 4 are not unlike those portrayed in the schematic view of the supercell thunderstorm (Fig. 3). [One major difference, however, is that the schematic depicts a warm-frontal occlusion, rather than a cold frontal occlusion as in both the simulation and observation.]

Figure 5 shows the simulated storm-relative horizontal wind field and radar reflectivity at 3.5 km above ground level (AGL). A region of minimum reflectivity or BWER is located within the cyclonic circulation of the mesocyclone. An anticyclonic vortex is apparent in the high-reflectivity region to the northwest of the BWER. Anticyclonic eddies are common features in large supercell storms (Johnson and Brandes, 1986). For comparison, the observed radar reflectivity field at 5 km MSL (4 km AGL) is shown in Fig. 6. Features such as the hook echo, BWER, streamer, and V notch are present in both observation and simulation. Differences do occur in the magnitude of the radar reflectivity, with values typically being less in the simulation.

The model simulated radar-reflectivity and wind vectors occurring in the vertical west to east plane through the center of the BWER are shown in Fig. 7. The same fields as observed by Doppler radars are shown in Fig. 8. Many features of the simulated and observed fields match moderately well. The radar-reflectivity vault and overhanging echo curtain (or streamer) are present in both. Inflow from the east extends through a depth of roughly 4.5 km and outflow from east occurs above 9 km, in both modeled and observed

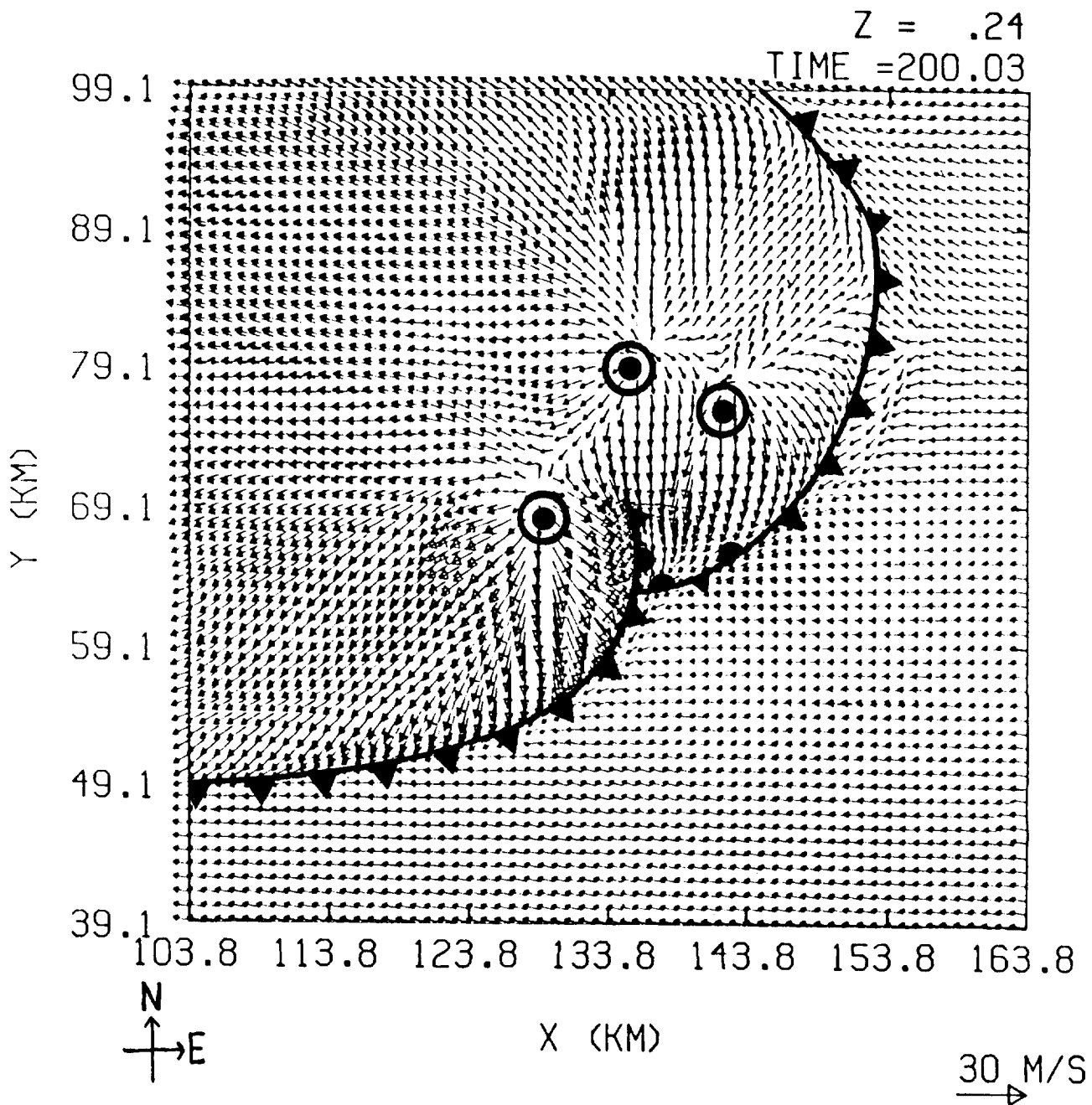


Fig. 4. Simulated horizontal cross section of wind vector field (ground relative) at 240 m AGL for Case I. The downdraft centers are designated by  $\odot$ .

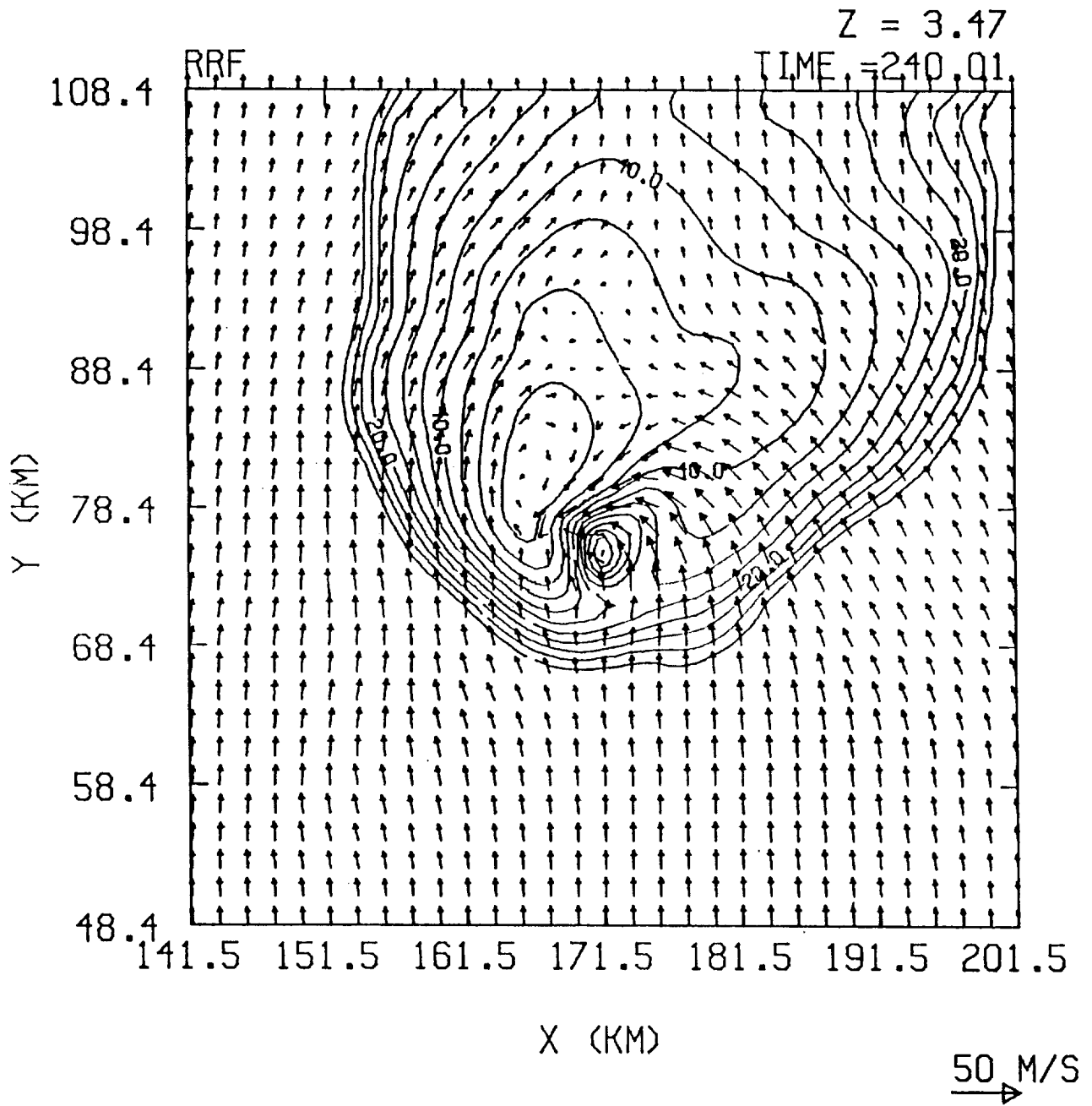


Fig. 5. Horizontal cross section of simulated wind vector field (storm relative) and radar reflectivity at 3.5 km AGL for Case I. The contour interval is 5 dBZ.

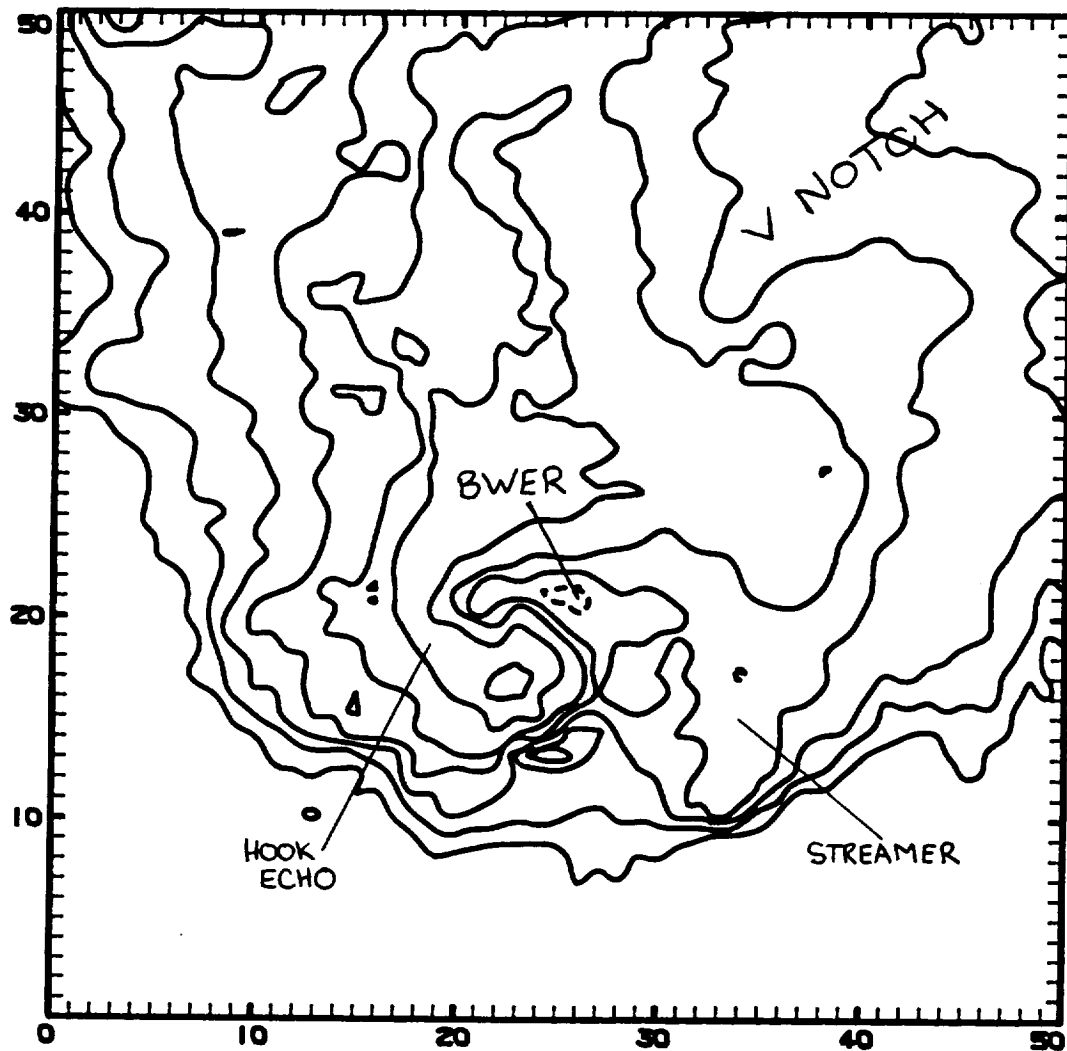


Fig. 6. Observed radar reflectivity at approximately 4 km AGL. The contours start at 10 dBZ and increment by 10 dBZ. (Modified from Miller, 1985)

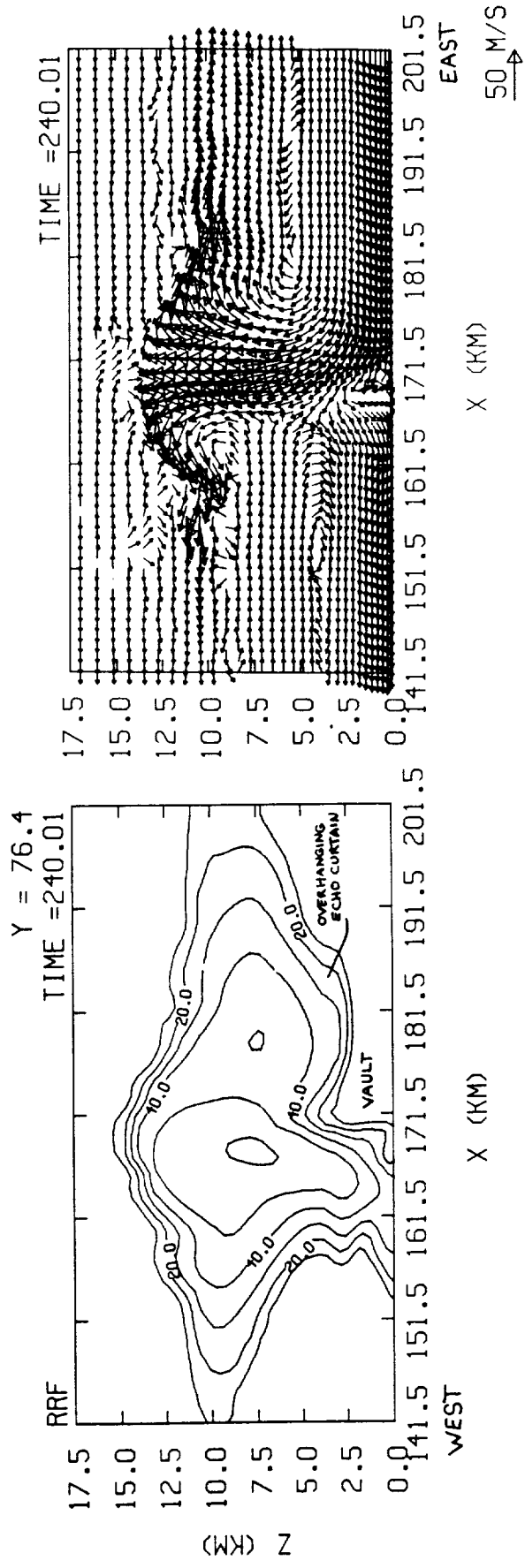


Fig. 7. Vertical west-east cross sections of simulated radar reflectivity and storm relative wind field for Case I. The contour interval for radar reflectivity is 10 dBZ.

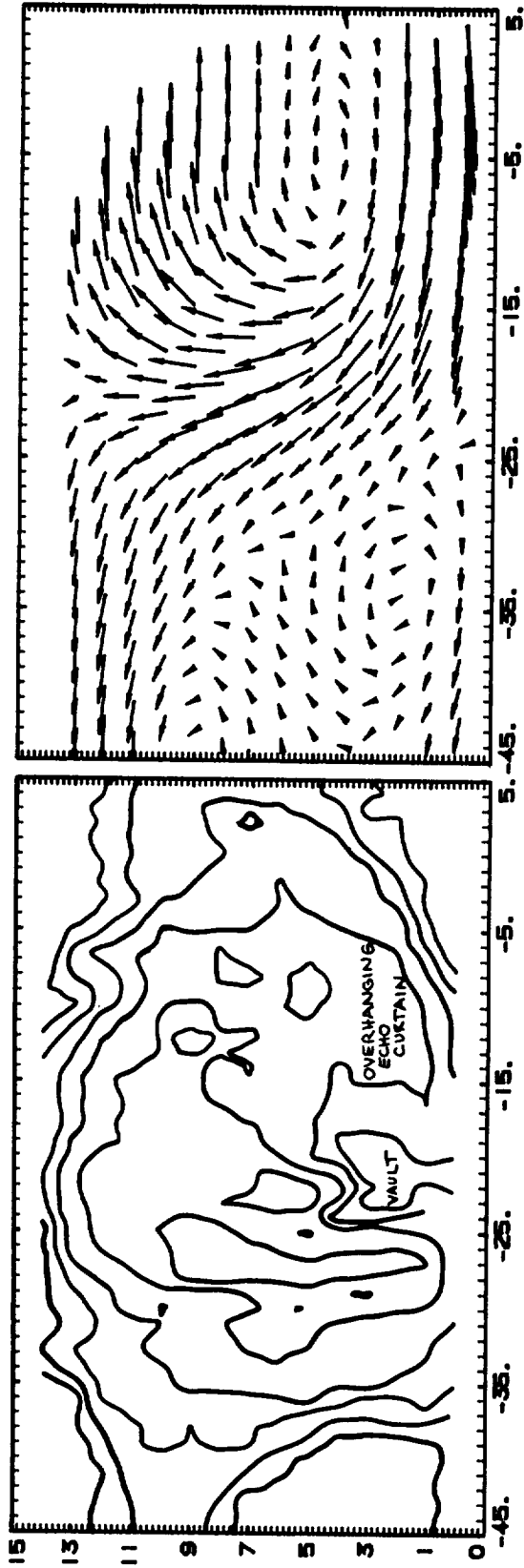


Fig. 8. Same as Fig. 7 but observed radar reflectivity and Doppler-derived wind field. The radar reflectivity contours start at 10 dBZ and increment by 10 dBZ. (From Miller, 1985)

and is collocated with the updraft. Most precipitation falling from the east side of the storm appears to be swept inward by the strong low-level inflow and is unable to reach the ground.

The equivalent potential is defined in the model diagnostics as

$$\theta_e = \theta \exp(L_v Q_v / C_p T_c)$$

where  $\theta$  is the potential temperature,  $L_v$  is the latent heat of vaporization,  $Q_v$  is the vapor mixing ratio,  $C_p$  is the gas constant for air at constant pressure, and  $T_c$  is the condensation temperature. Figure 9 indicates that  $\theta_e$  is nearly conserved along the core of the updraft -- indicating that there is no significant mixing of the environmental air into the center of the simulated storm. Measurements by a research aircraft indicated an adiabatic updraft core within the hailstorm (Musil et al., 1986).

#### Summary and Conclusions for Case I

Some discrepancies between the observed and simulated storms are likely to result from the neglect of horizontal variations present in the environment. For example, the observed storm propagated ESE along a cold front and ingested at least some of the air to the north of the front (see Wade, 1982). The inclusion of this cold front into the simulation would likely increase the rotation and pressure falls at storm low levels, since likely, there would be baroclinic generation of vorticity along the front and convergence of this vorticity into the updraft. Simulated pressure falls at the surface were between 1 to 2 mb as compared to an observed value of 6 mb. This discrepancy probably results from the neglect of temporal and

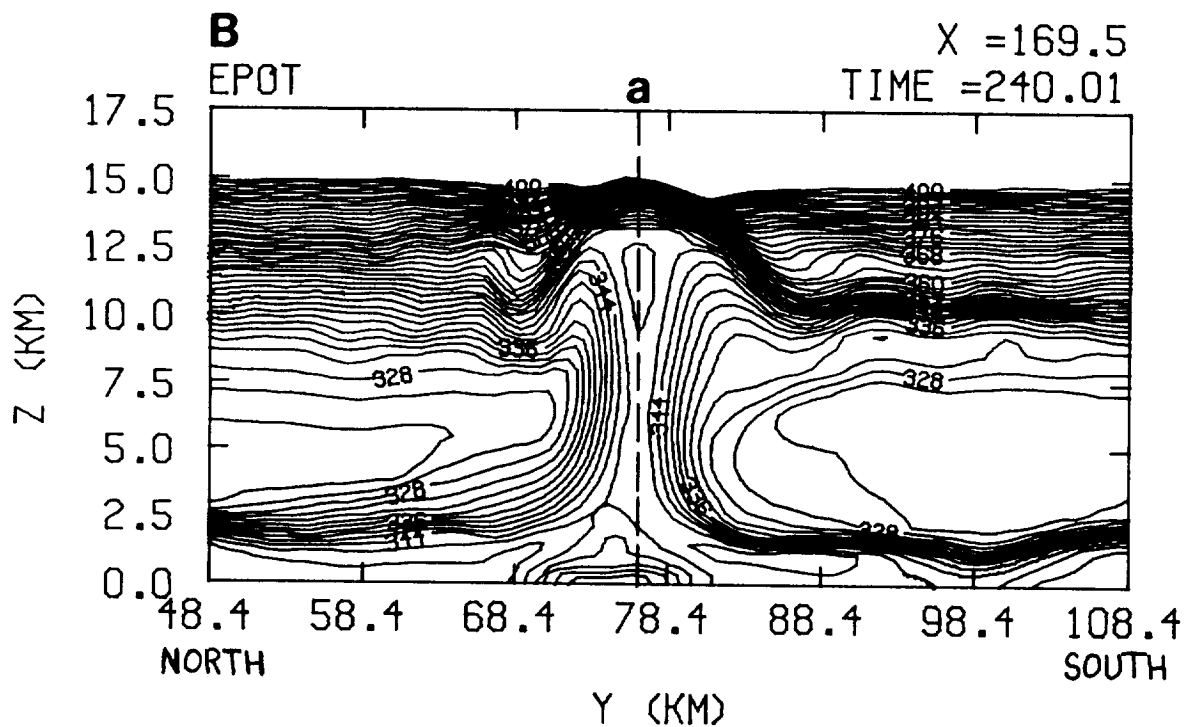
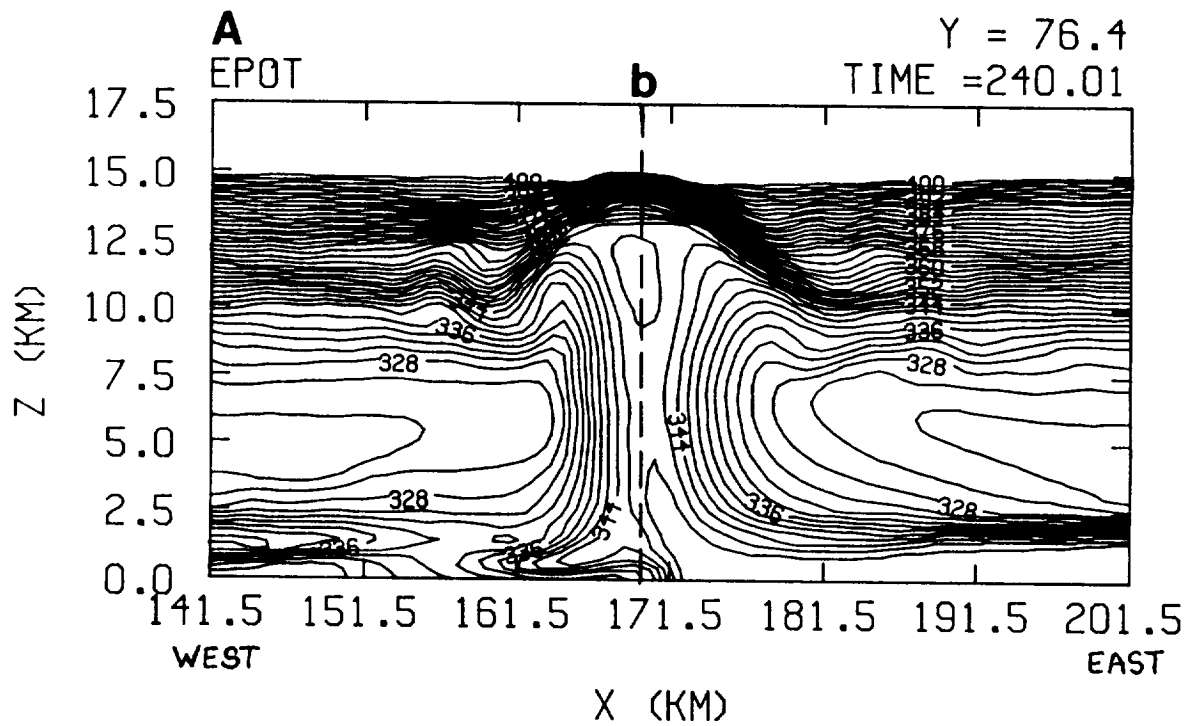


Fig. 9. Simulated vertical cross sections of equivalent potential temperature for Case I. The cross sections are (a) east-west and (b) north-south through the core of the storm updraft. The contour interval is  $2^{\circ}\text{C}$ . Contours having values greater than 400 K are not plotted.

horizontal variations in the environment, rather than from some basic model deficiency.

The neglect of the hail production term due to snow riming was at least partly responsible for the underestimate of radar reflectivity and the slow development of the hail field. Maximum simulated values of radar reflectivity were 60-65 dBZ, while observed values ranged up to 75 dBZ.

A simulation of this same case with the Klemp-Wilhelmsen model (1978) has been reported by Weisman et al. (1983a, 1983b). A comparison of the kinematic features between the two simulations shows some similarities and some discrepancies. Both models simulate an updraft with a maximum speed of  $50-55 \text{ m s}^{-1}$ , as well as some of the major storm features. However, one major discrepancy is the absence of an intense western-flank downdraft in the Weisman et al. simulation; instead, an intense downdraft was simulated north of the updraft. This discrepancy between the Weisman et al. simulation and the TASS simulation and observed data may be due to the absence of ice-phase microphysics in the Klemp-Wilhelmsen model.

Weisman et al. (1983a) reports that a key factor in producing the BWER is the entrainment of drier air from above the moist surface layer into the updraft. The TASS results of this case do not support their theory, but instead confirm the generally accepted explanation put forth by Browning and Donaldson (1963). The TASS simulated BWER was found to coincide with an intense and undiluted updraft (also see Proctor, 1985b). Little or no precipitation was found in the BWER for two reasons: (1) precipitation particles are swept upward into the storm upper levels before growing to detectable sizes; and (2) precipitation which is transported into the updraft is rapidly swept upwards before penetrating the updraft core.

The model was successful in simulating many of the observed features, such as (1) the low-level hook echo appendage, (2) the radar reflectivity vault, (3) the overhanging echo curtain, (4) a long-lasting and broad updraft with cyclonic rotation, (5) an unmixed updraft core, (6) an intense low-level downdraft within the high reflectivity region WNW of the updraft, (7) hailfall at the ground extending from the west to the north of the storm updraft, (8) intense updraft outflow within the anvil, (9) intense downdraft outflow near the surface behind the gust front, and (10) a rightward veering in the propagation of the storm. The model results also appear to confirm the theory for wall cloud development presented in Rotunno and Klemp (1985). The demise of the model storm did not occur anytime during the 4 hour and 20 minute simulation. More details on the simulation of this case have been presented in Proctor (1985b).

### 3. CASE II: SMALL CCOPE CUMULONIMBUS

The life cycle of a small isolated thunderstorm was observed within the CCOPE network on 19 July 1981. A description of the thunderstorm is summarized from Dye et al. (1986) as follows. The cumulonimbus, with a diameter of approximately 5-8 km, developed from towering cumulus upward to an altitude of 10-11 km mean sea level (MSL). A broad organized updraft persisted through the development stage of the thunderstorm, but dissipated soon after the onset of precipitation at the ground. During the active phase of the cloud, maximum updraft velocities were 10-15 m s<sup>-1</sup>. The character of the microphysics was essentially continental -- with no raindrops being observed above the melting level. Radar reflectivities (>5 dBZ) were first observed at 6-7 km (MSL) and were attributed to the formation of precipitation-sized ice particles in that region. Maximum radar reflectivities decreased during the dissipation stage, as only a trail of light precipitation falling from a widespread anvil remained.

The simulation of this case and a comparison with data presented in Dye et al. (1986) should determine how well TASS can model the life cycle of a short-lived continental cumulonimbus.

#### Initial Conditions for Case II

Since the thunderstorm in this case covers a much smaller area than in the previous case, a smaller computational domain area is used. The domain has a horizontal area of 10 km × 10 km and is resolved by a horizontal grid size of 250 m. The depth of the domain is 12 km and is resolved by 27 layers; the layers are separated by a vertical spacing which varies from approximately 220 m near the ground to approximately 700 m near the top boundary. The value for the cloud-droplet number density is assumed

as  $N_{CD} = 600 \times 10^6 \text{ m}^{-3}$ , which is taken from aircraft measurements within the actual storm (Dye et al., 1986). Other initial specifications for this case can be found in Table 1.

The observed sounding nearest the time and location of the thunderstorm is shown in Fig. 10. The sounding was observed approximately 1 hour and 40 minutes prior to and 35 km to the east of the initial cumulonimbus development. Aircraft data measured within the thunderstorm indicated that the cloud base pressure and temperature were approximately 635 mb and  $1^{\circ}\text{C}$ , respectively (Dye et al., 1986). The model input sounding (Fig. 11) is modified from the original sounding (Fig. 10) in order to be consistent with these values. Ground level in this simulation is assumed to be approximately 800 m MSL; hence cloud base level is approximately 3.1 km AGL.

#### Results for Case II

The development of the cloud was triggered by a 2.5 km radius thermal impulse at time zero in the model. The first echo developed shortly after 20 minutes (model time) at a height between 5 and 6 km AGL (see Fig. 12). The initial echo was associated with the formation of snow. Little, if any, rain was found above the cloud base, as was true in the actual thunderstorm.

Figure 13 indicates that the simulated updraft begins to dissipate once the precipitation reaches the ground (cf. Fig. 12). A downdraft which is primarily confined to below cloud-base levels ( $<3.1$  km AGL) is associated with the falling precipitation. In the actual storm, peak updraft speeds were observed between 10 to  $15 \text{ m s}^{-1}$  and diminished during the dissipation stage; no organized downdraft was indicated above the cloud-base level (Dye et al., 1986). As evidenced in Figs. 13 and 14, the model results are consistent with these observations.

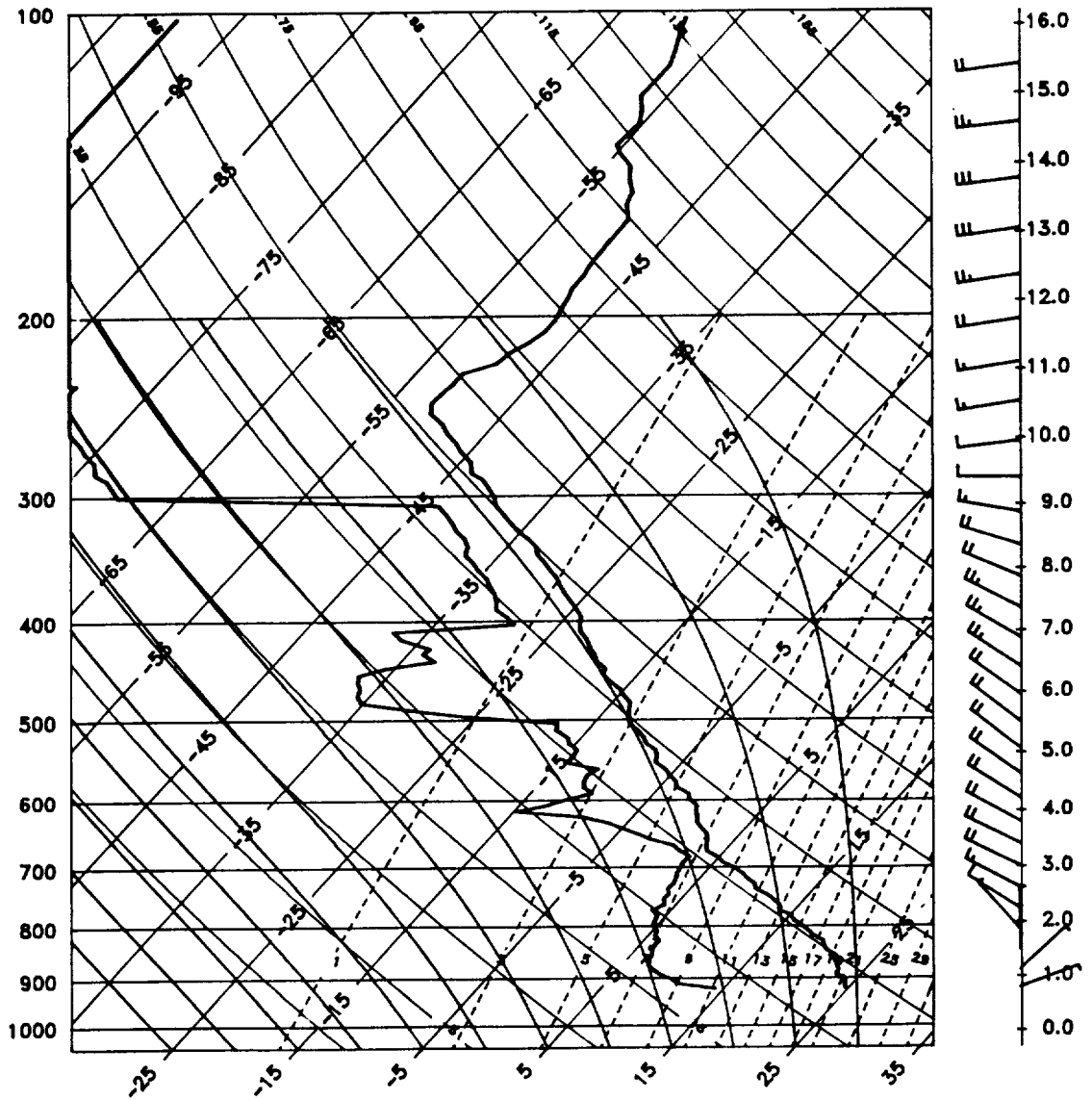


Fig. 10. Same as Fig. 1 but observed at Miles City, Montana on 19 July 1981 at 1440 MDT.

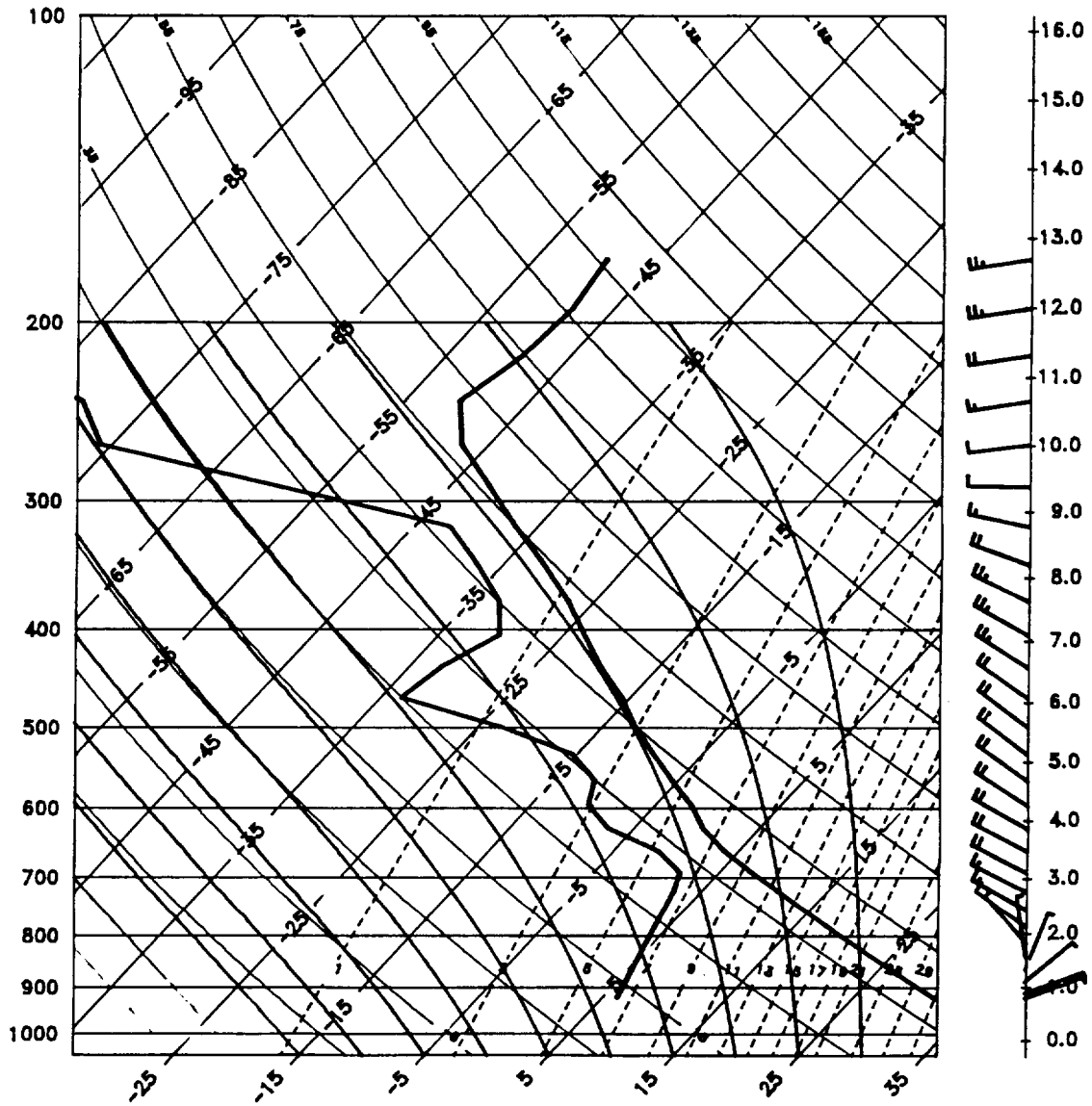


Fig. 11. Model input sounding for Case II. Modified from Fig. 10 to agree with observed cloud-base temperature and pressure.

RRF

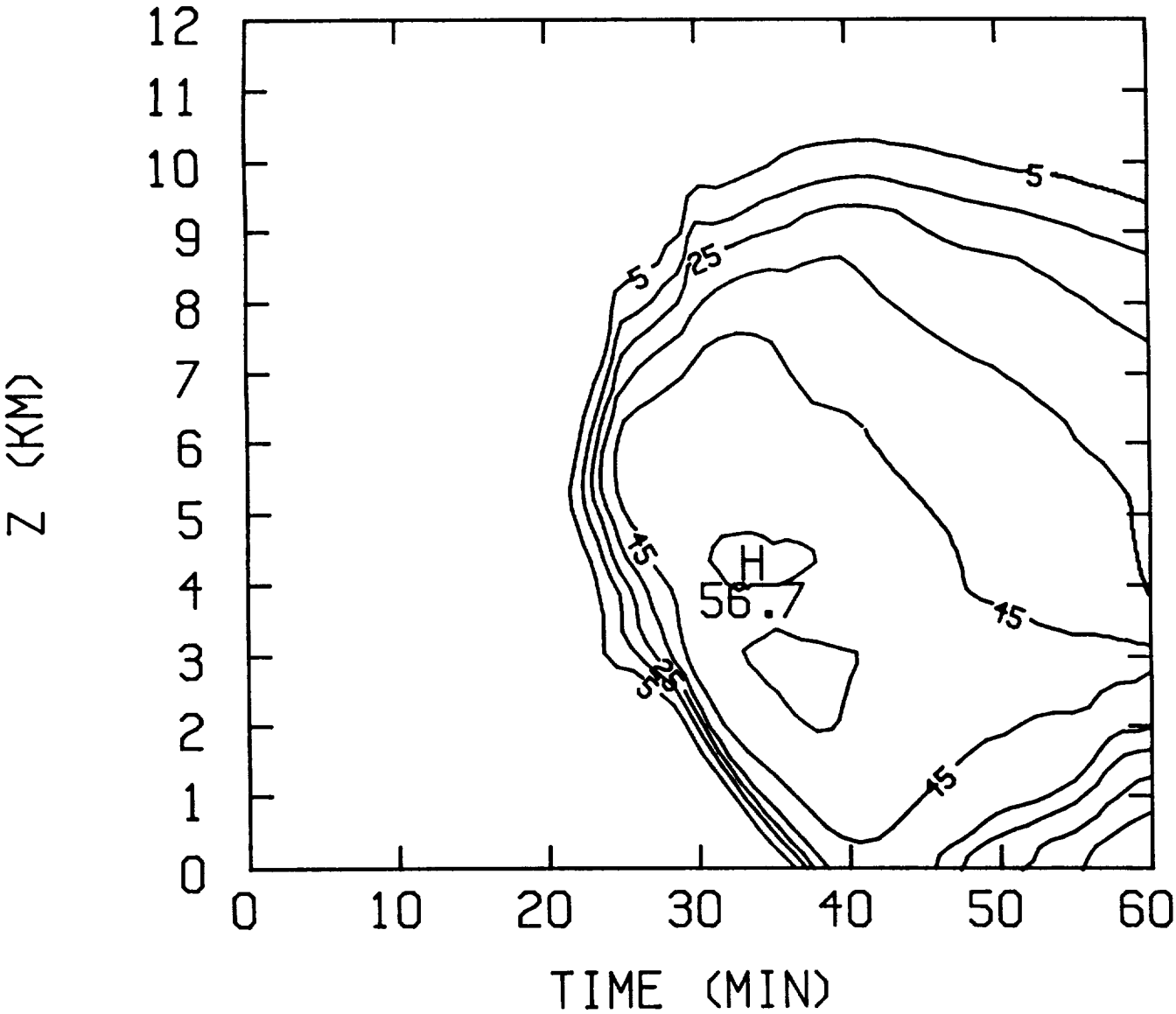


Fig. 12. Simulated maximum radar reflectivity at a given time and height above the ground for Case II. The contour interval is 10 dBZ.

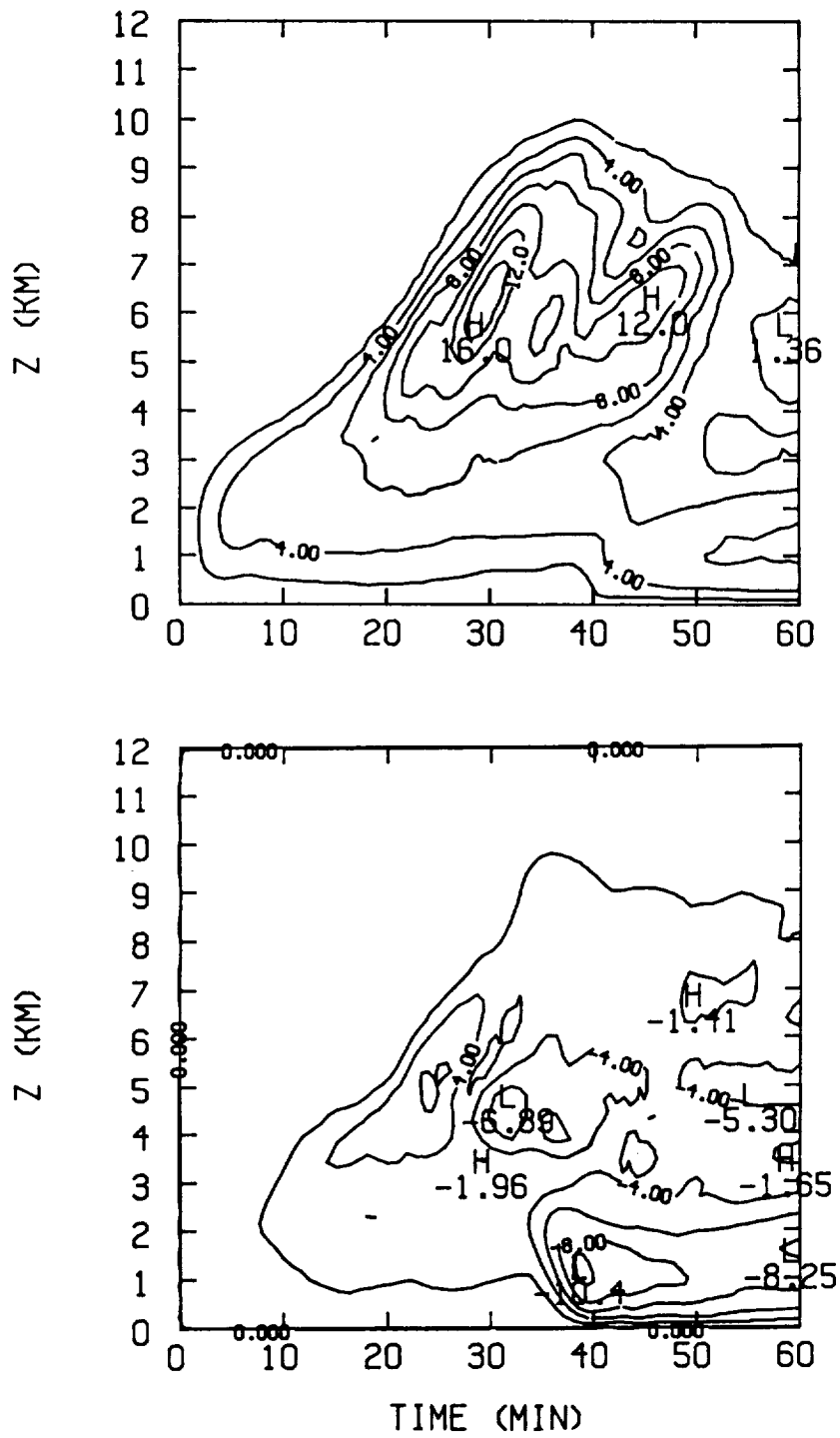


Fig. 13. Simulated maximum vertical velocity (upper) and minimum vertical velocity (lower) at a given time and height above the ground for Case II. The contour interval is  $2 \text{ m s}^{-1}$ .

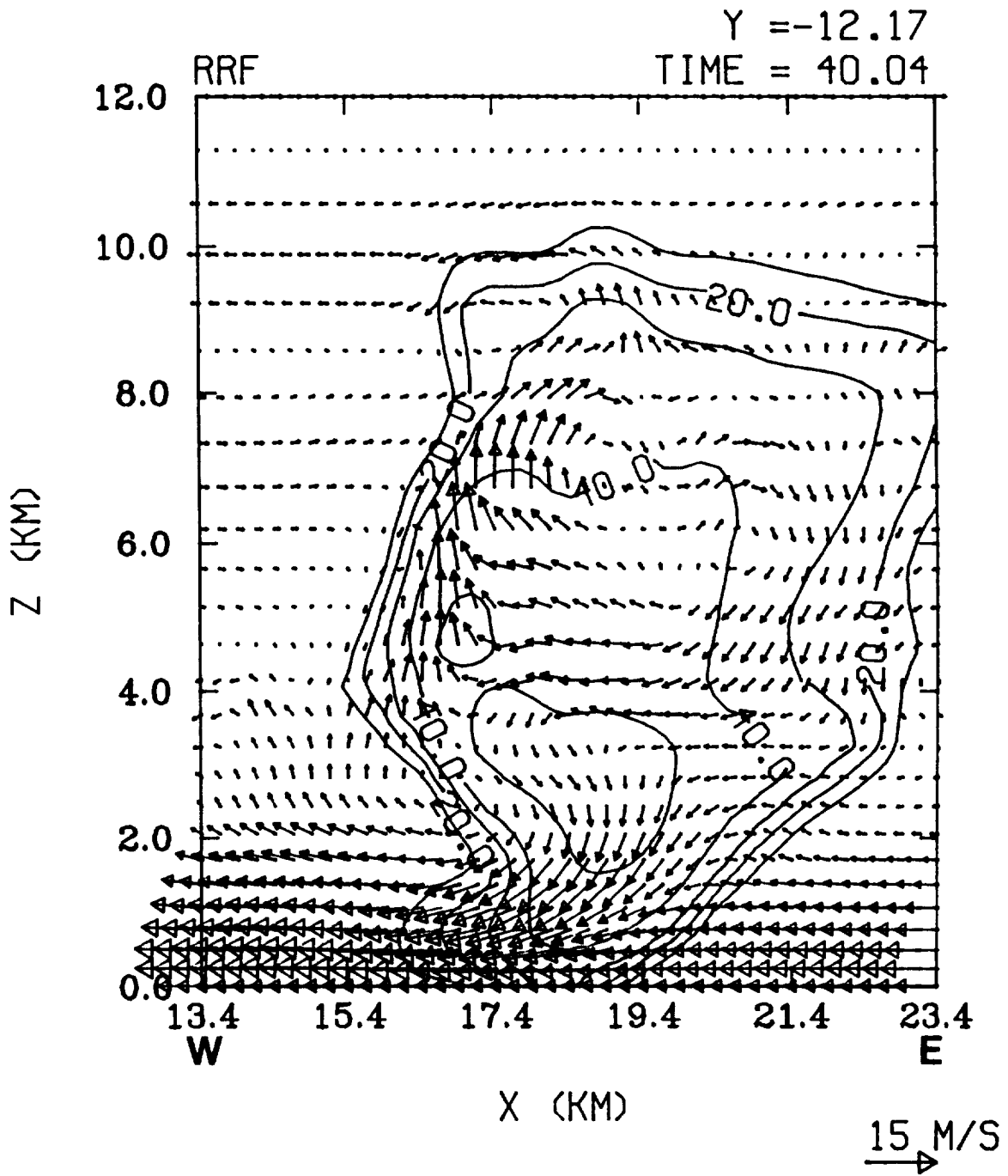


Fig. 14. Simulated west-east vertical cross section of radar reflectivity and storm-relative vector wind field at 40 minutes for Case II. The contour interval for radar reflectivity is 10 dBZ.

The vertical structure of the simulated storm during its mature phase is depicted in Figs. 14 and 15. The equivalent potential temperature is roughly conserved within the updraft, which was also indicated from aircraft measurements in the actual thunderstorm (Dye et al., 1986).

A horizontal cross section of the simulated radar reflectivity at 30 minutes and 6.1 km MSL (5.3 km AGL) is shown in Fig. 16. The diameter of the echo is roughly 6 to 8 km, as was true in the observed storm. The structure of simulated echo compares roughly to that observed with the PPI scan as shown in Fig. 17. The observed and simulated echo are both skewed toward the ESE and SSE; the simulated echo, however, has a broader area of greater than 40 dBZ reflectivity. The propagation of the radar echo in the simulation is very close to that which was observed. During the mature phase of the simulated storm (between 30 and 40 min), it moved from  $301^\circ$  at  $10.8 \text{ m s}^{-1}$ . In comparison, the observed storm (between 1630:43 and 1639:11 MDT) translated from  $293^\circ$  at  $10 \text{ m s}^{-1}$ .

The observed and simulated maximum radar reflectivity as a function of altitude and time are shown in Fig. 18. A comparison of the height of the first 5 dBZ echo (6-7 km), maximum altitude of the 35 and 45 dBZ echo (9-9.5 km and 8-8.5 km, respectively), and maximum radar reflectivity (just over 55 dBZ) shows good agreement. Also, both observation and simulation agree that the radar echo expands upward and downward with time, followed by a general decrease in intensity beginning in the upper parts of the clouds. The modeled storm, however, has a sharper temporal gradient. These and other differences are likely a consequence of the bulk parameterization assumptions, but other factors such as the choice of initial and environmental conditions and grid resolution may contribute as well.

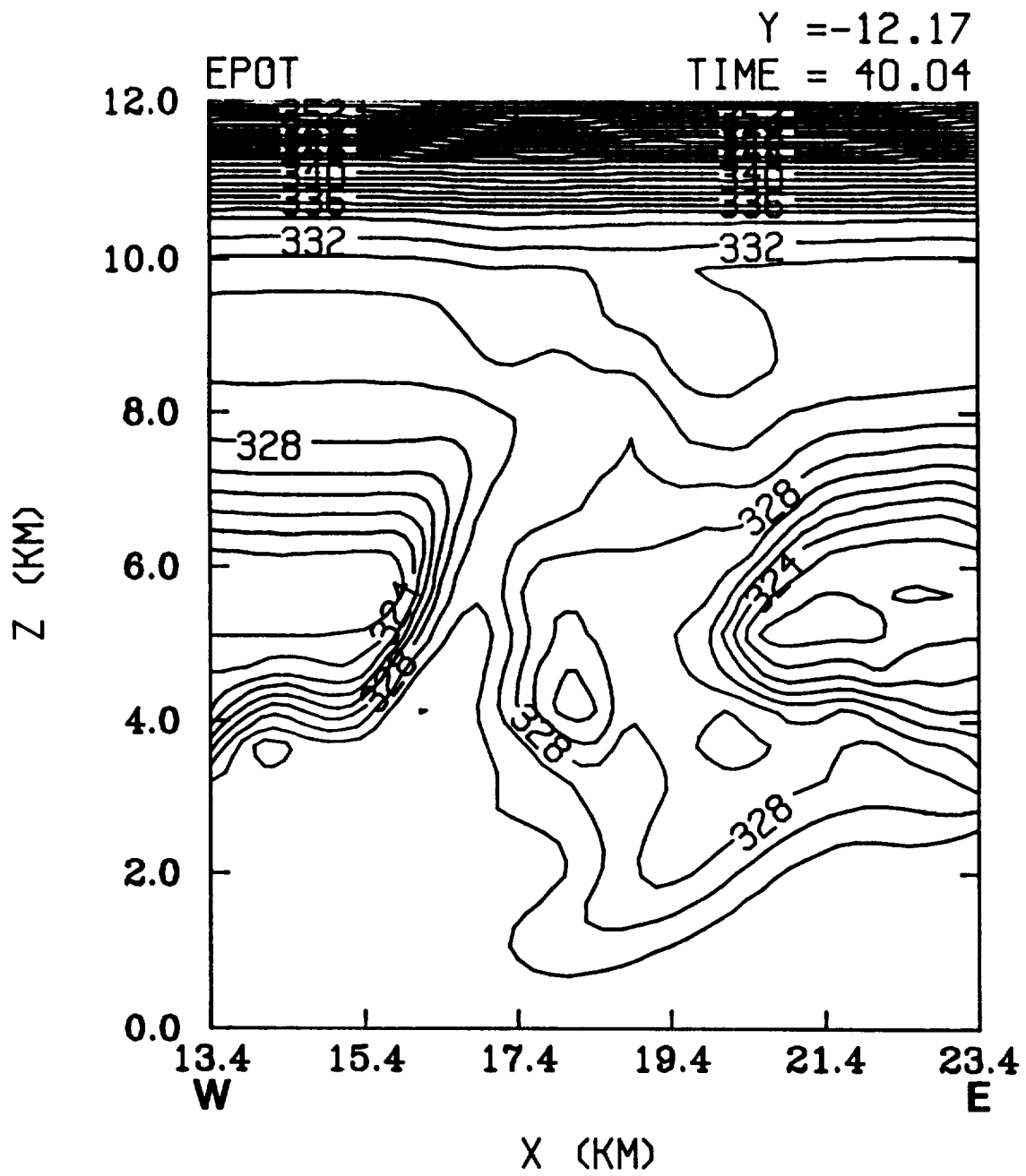


Fig. 15. Same as Fig. 14 but for equivalent potential temperature. The contour interval is  $1^{\circ}\text{C}$ .

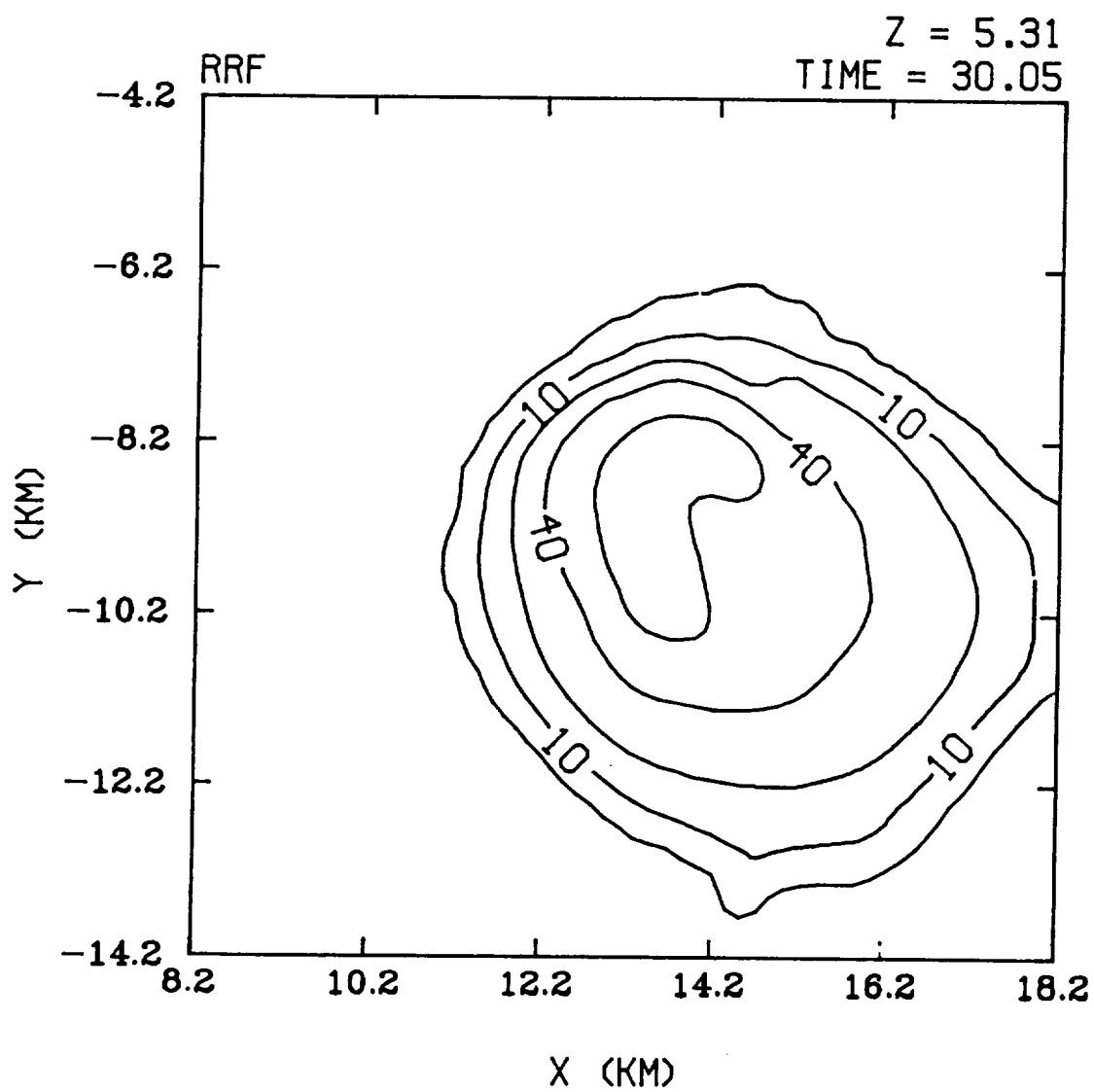


Fig. 16. Simulated horizontal field of radar reflectivity in Case II at 6.1 km MSL (5.3 km AGL). Contour intervals are 1, 10, 25, 40, and 50 dBZ.

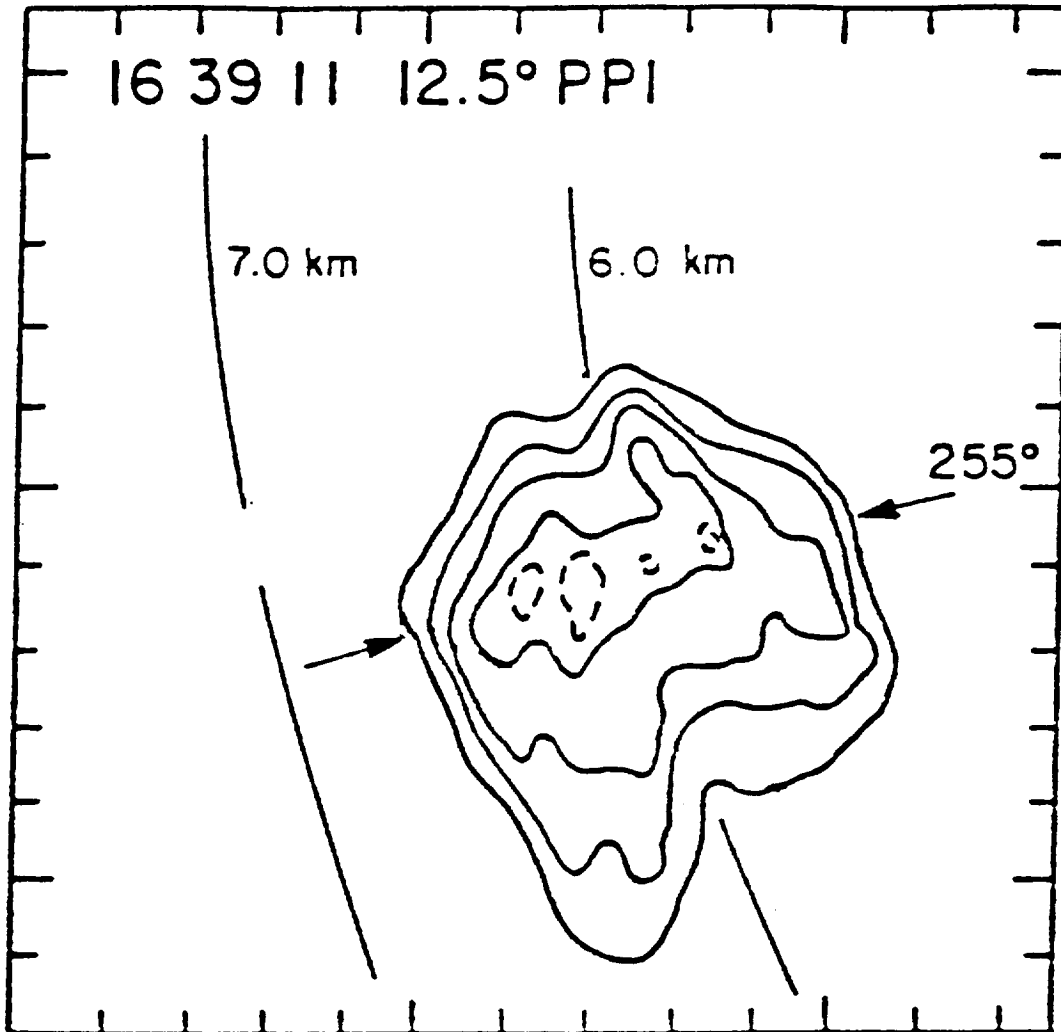


Fig. 17. Observed reflectivity from radar PPI sweep at 1639:11 MDT. Each tick mark represents 1 km. The solid contours start at -5 dBZ and increase by steps of 15 dBZ (from Dye et al., 1986).

19 JULY 1981

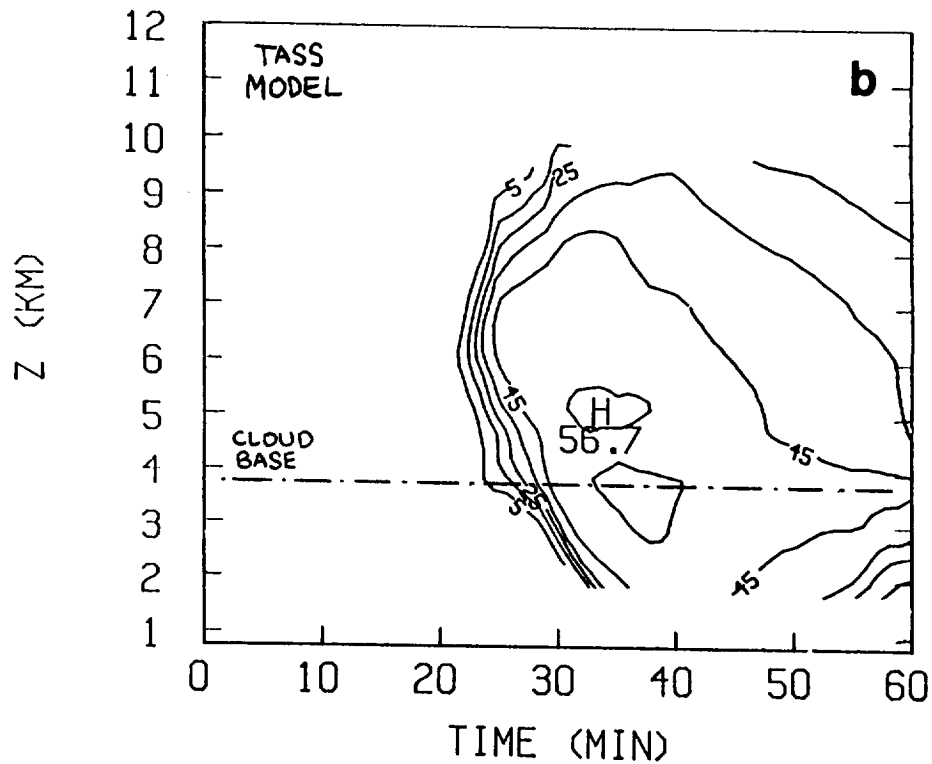
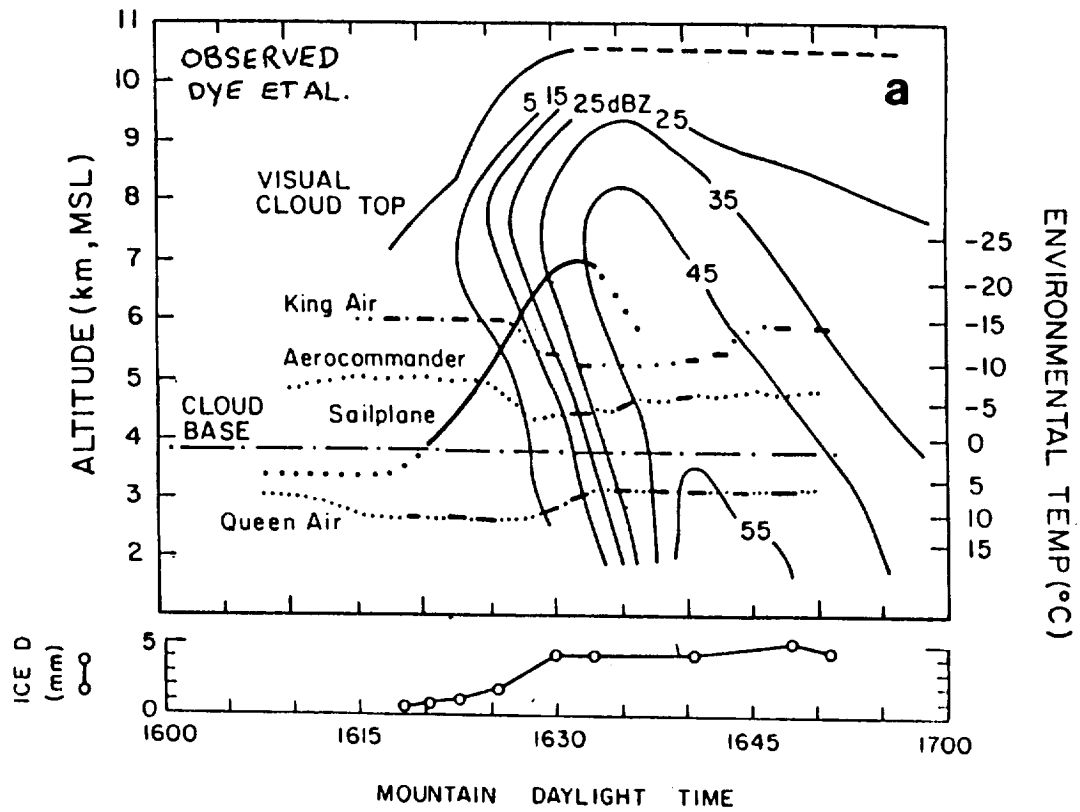


Fig. 18. Maximum radar reflectivity at a given time and altitude: (a) observed (from Dye et al., 1986); (b) simulated. Contour interval is 10 dBZ.

The three-dimensional perspectives of the simulated cloud (Fig. 19) illustrate the cloud life cycle. Within the first 30 minutes the cloud builds primarily upwards, after which time an anvil begins to form and spreads laterally. During the latter stage (after 40 min) the lower and mid-levels of the clouds dissipate, leaving only the anvil portion of the cloud and a trail of light precipitation.

#### Summary for Case II

The life cycle of a small continental cumulonimbus is simulated in this Case. Maximum updraft velocity, maximum radar reflectivity, echo width and shape, echo propagation, storm height, and altitude of first radar echo are consistent with observations. The simulated storm begins to dissipate after precipitation reaches the ground, and ends as a precipitating anvil, as was observed in the actual thunderstorm.

The ice phase plays a significant role in the microphysics of this storm. Precipitation developed according to Bergeron theory; both simulation and observation indicated little if any rain above the cloud base. The first echo in both simulation and observation occurred between 6 and 7 km (MSL) due to precipitation-sized ice particles.

The simulation produces a very small amount of rain and hail at the ground; simulated precipitation rates reached  $2 \text{ mm hr}^{-1}$  for a brief period of time. Maximum outflow speeds in excess of  $10 \text{ m s}^{-1}$  occur at 42 min in the simulation -- which is several minutes after precipitation initially reaches the ground and at a time when the radar reflectivity is decreasing throughout the storm (see Fig. 12). The simulated downdraft and subsequent outflow could be categorized as a dry microburst (Fujita and Wakimoto, 1983) since precipitation at the ground was very light. At the time of

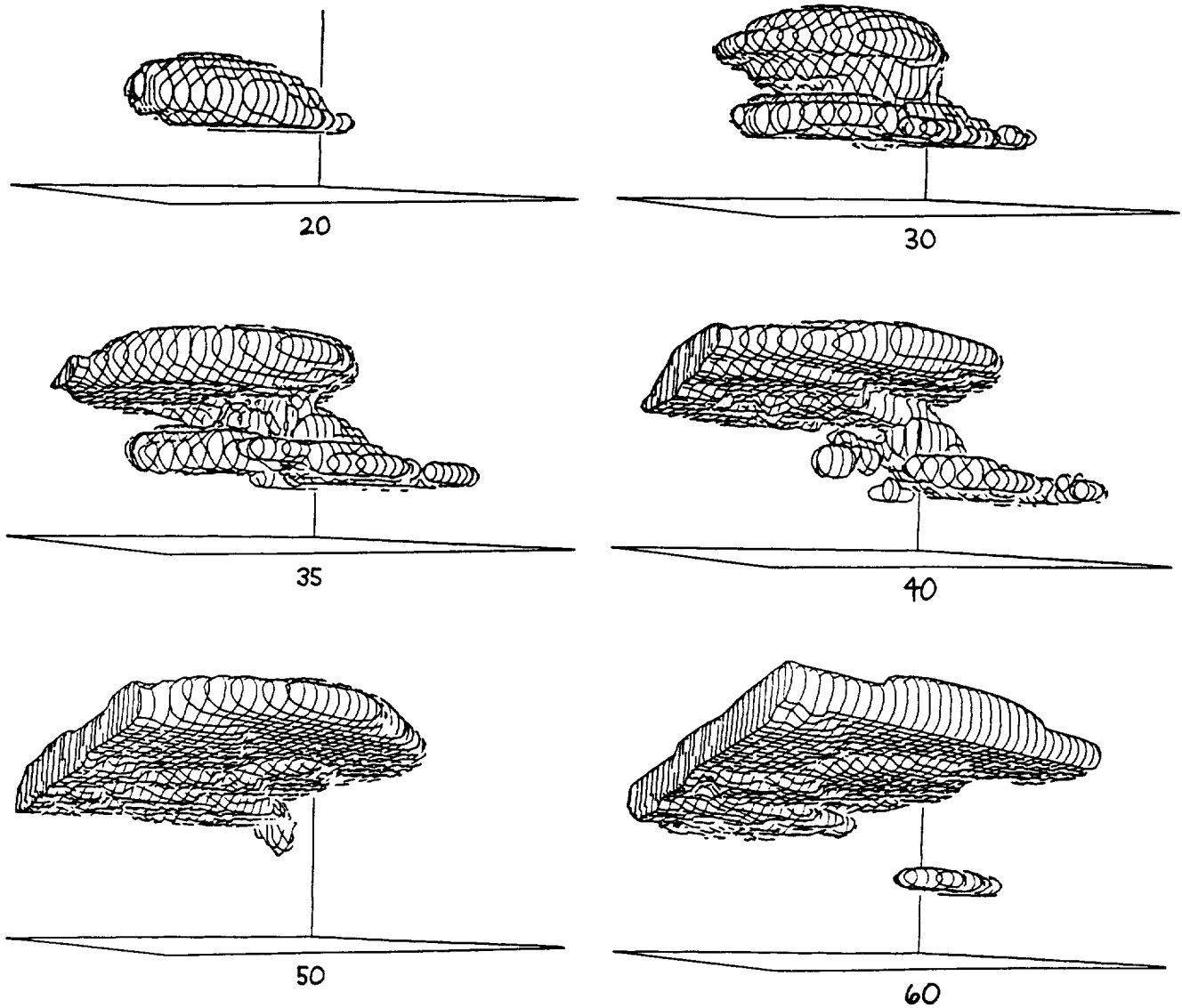


Fig. 19. Simulated three-dimensional cloud perspectives at 20, 30, 35, 40, 50, and 60 min for Case II. Perspectives are viewed from northeast and do not include precipitation.

writing, observed data was not available to verify the low-level wind velocity structure of the thunderstorm.

#### 4. CASE III: DALLAS MICROBURST

On 2 August 1985 a small, but intense thunderstorm rapidly developed near the approach path of Runway 17L at the Dallas - Ft. Worth (DWF) Airport. Strong windshear produced by this storm apparently led to the tragic crash of a commercial air carrier -- flight Delta 191.

The weather situation as compiled from observations near the time of the accident is summarized from Salottolo (1985) and Fujita (1986) as follows. The thunderstorm, which led to the crash at 1806 CDT, was described as small but intense. Its radar echo was first observed at 1752 CDT (14 min prior to crash), 5 km NE of Runway 17L, and the intensity of the cell increased from VIP level 2 (30 - 41 dBZ) to level 5+ (>50 dBZ) as it moved slowly to the south. The diameter of the radar echo was 4.5 - 9 km and contained a tight reflectivity gradient. According to the National Transportation Safety Board Report (Salottolo, 1985) the radar top of the thunderstorm was between 14.3 - 15.9 km. The thunderstorm produced heavy rain, quarter-size hail (Daily Press, 1985), and damaging winds with measured gust in excess of  $35 \text{ m s}^{-1}$ .

#### Initial Conditions for Case III

The horizontal size of the domain is chosen as  $12 \text{ km} \times 12 \text{ km}$  and is resolved by a 200 m grid size. The vertical depth is 18 km and is resolved by 31 levels. Stretching of the vertical grid is defined by Eq. (104) in VOLUME I, with  $C_1 = 0.18$  and  $C_2 = 64 \times 10^{-6} \text{ m}$ . This gives a vertical spacing which varies from approximately 100 m near the ground to 1100 m near the top boundary. The stretching is made greater in this case study so as to better resolve the low-level structure of the microburst-producing storm.

The sounding for Stephenville, Texas (Fig. 20) was observed near the time of the DFW microburst, but 135 km to the southwest. A simulation assuming this sounding was conducted, but the simulated storm had a direction of propagation and a radar echo structure that was different from that observed near DFW at approximately 1800 CDT.

A much more agreeable simulation (which is presented below) assumes the interpolated sounding for DFW shown in Fig. 21. This sounding was obtained by first running the preprocessor (initialization package) of the Mesoscale Atmospheric Simulation System<sup>1</sup> (Kaplan et al., 1982), and then adjusting the low-level temperature and humidity so as to agree with the 1800 CDT surface observations at DFW. The most significant differences between the computed DFW sounding and the observed SEP sounding can be found in the wind direction and low-level humidity.

Only the results from the DFW sounding are presented in this case study. Other initial specifications for this case can be found in Table 1.

### Results for Case III

The structure of the simulated radar echo at 3 km AGL is shown in Fig. 22. It has a shape very similar to the observed radar echo in Fig. 23; both simulation and observation show an elongation from the NW to SE direction. Salottolo (1985) reported that the observed echo was 4.5 km to 9.5 km wide, had a very tight reflectivity gradient, and contained a VIP level of 5 or 6 (>50 dBZ). The simulated echoes (see Figs. 22 and 24)

---

<sup>1</sup>The Mesoscale Atmospheric Simulation System (MASS) is a regional weather prediction model; it uses the LFM initial data base and current rawinsonde data as initial input.



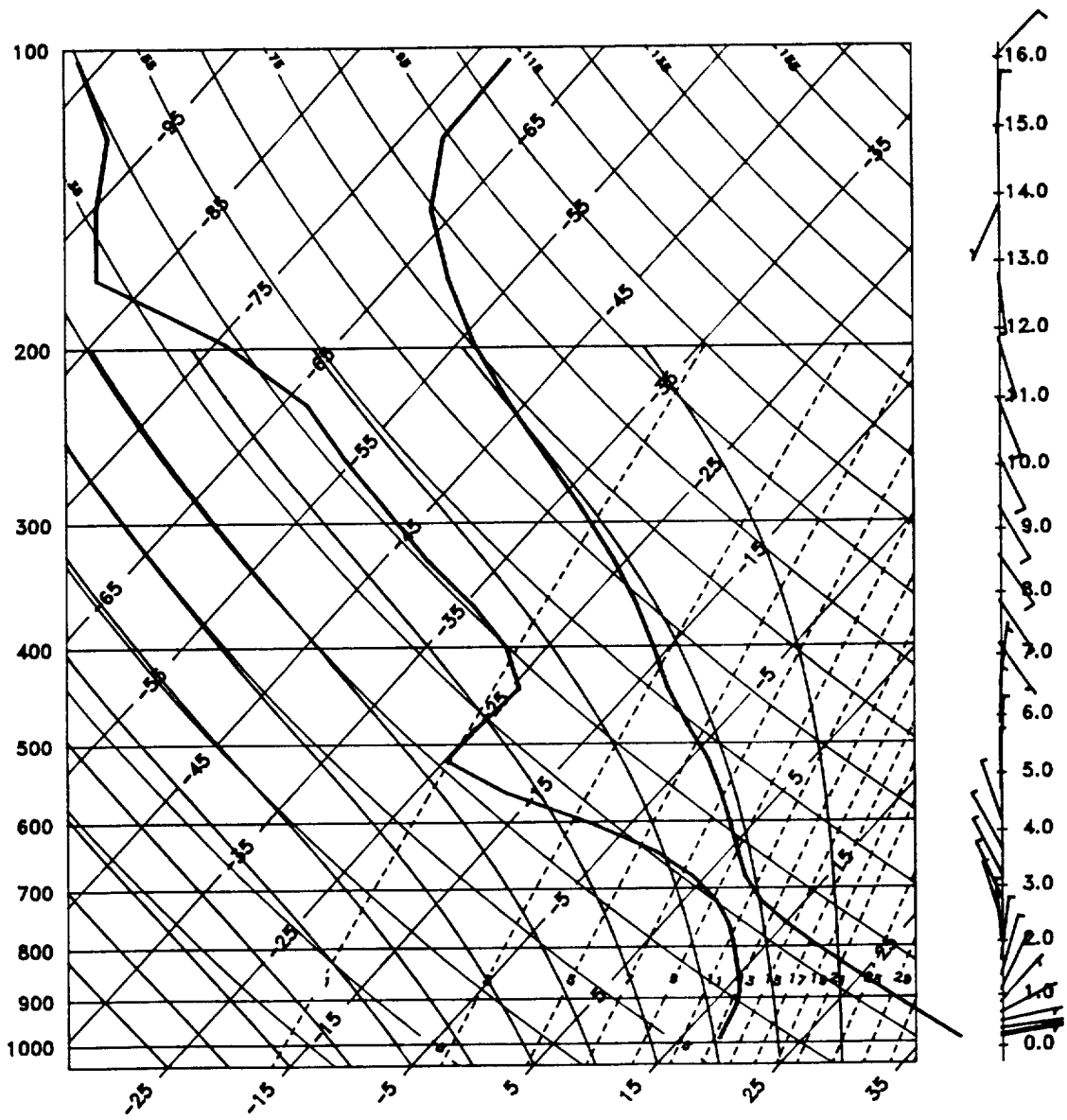


Fig. 21. Model input sounding for DFW on 2 August 1985 at 1800. Obtained from MASS preprocessor (see text).

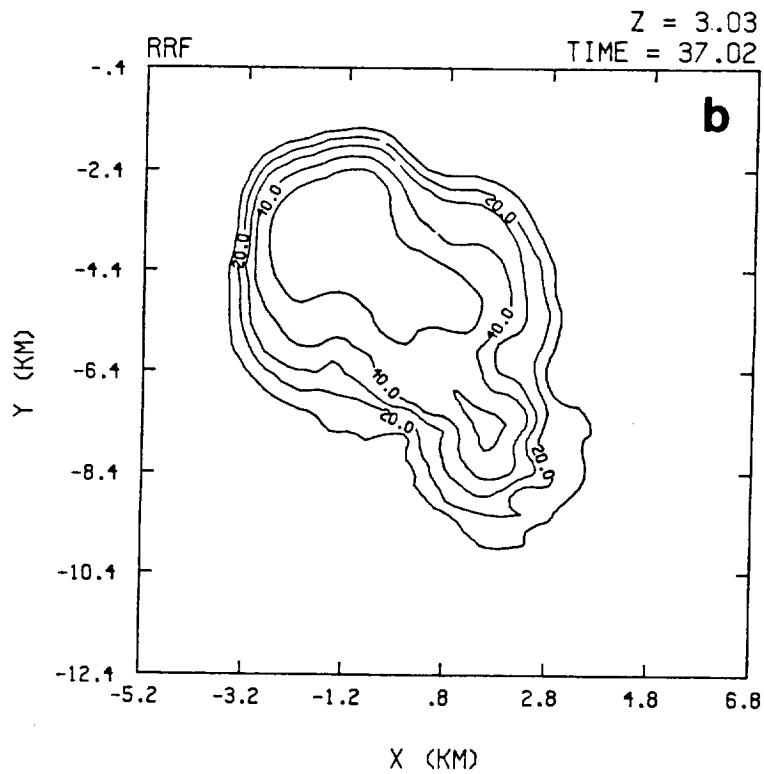
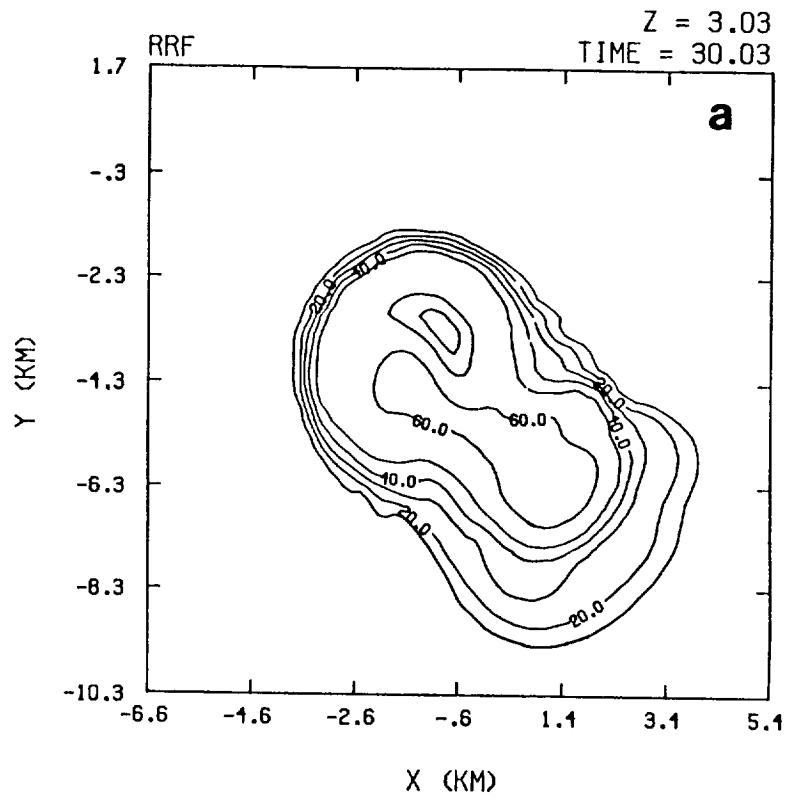


Fig. 22. Simulated radar reflectivity for Case III at 3 km AGL at (a) 30 min and (b) 37 min. The contour interval is 10 dBZ.

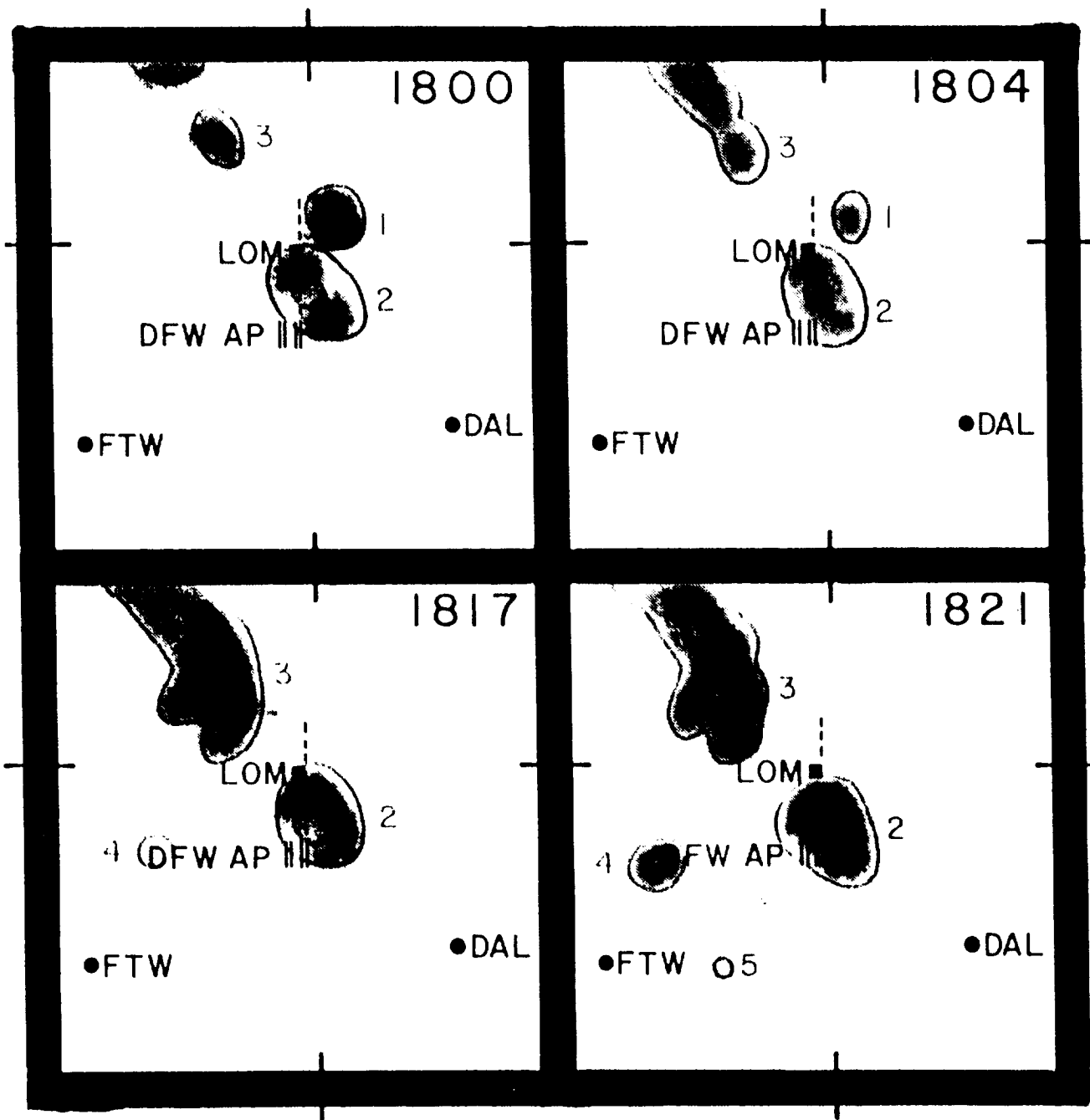


Fig. 23. A sequence of radar photos from Stephenville radar (from Fujita, 1986).

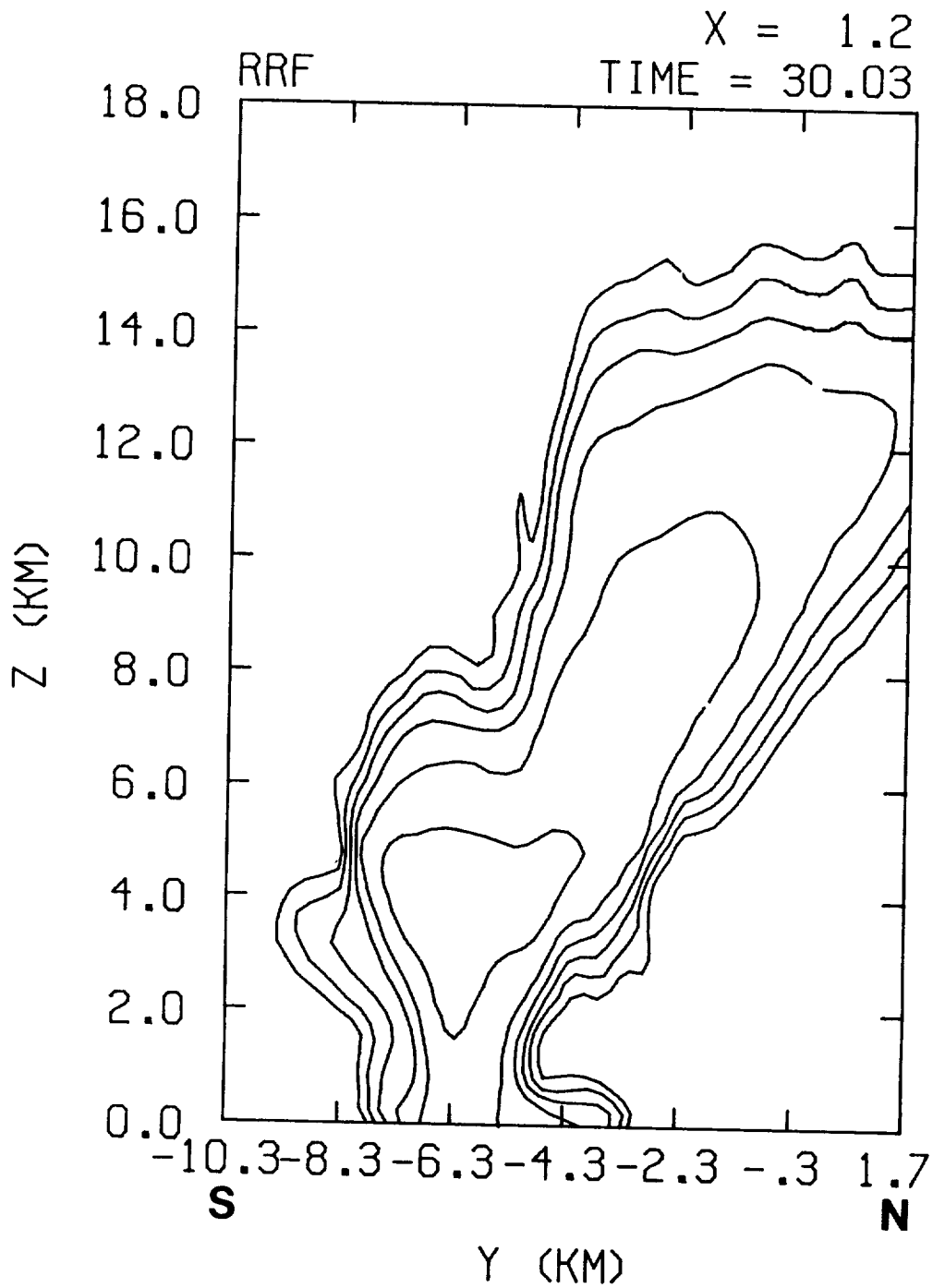


Fig. 24. South-north vertical cross section of the simulated radar reflectivity at 30 min for Case III. The contours begin at 10 dBZ and increment by 10 dBZ.

compare well with these values; its horizontal dimension is between 4.5 km and 8 km, has a tight reflectivity gradient, and has a peak radar reflectivity in excess of 60 dBZ. Propagation of the simulated cell agreed with observations; both the simulated and observed radar echo were nearly stationary with a slow movement toward the south.

The actual storm top was inferred from satellite data by Fujita (1986) as 7 km. However, Solottolo (1985) reported that Stephenville radar and two local TV-Weather radars observed the storm top at about 15.2 km (50,000 ft). The model simulated radar echo top was between 15 km and 16 km (e.g., Fig. 24), which is in agreement with Solottolo.

Also produced in the simulation was an intense microburst outflow. A time sequence of the simulated low-level wind field is shown in Figs. 25 - 27. Divergent outflow rapidly intensifies after the precipitation initially reaches the ground at 27 minutes. The microburst outflow expands rapidly in a near-symmetrical pattern, growing into a macroburst (Fujita, 1981) within several minutes. Multiple downdraft centers develop within the expanding outflow after 32 minutes, and by 37 minutes these downdraft centers appear as microbursts embedded within the expanding macroburst outflow (see Fig. 27b).

Peak outflow speeds in excess of  $22 \text{ m s}^{-1}$  are obtained at 31 minutes -- 4 minutes after the precipitation first reaches the ground. This lag time (between the initial precipitation and the peak outflow speed) is consistent with that of microbursts studied in the Joint Airport Weather Studies (JAWS) Project (see Wilson et al., 1984).

Heavy rainfall rates were associated with the simulated microburst. Peak values at the ground reached 80 mm/hour at approximately 31 min.

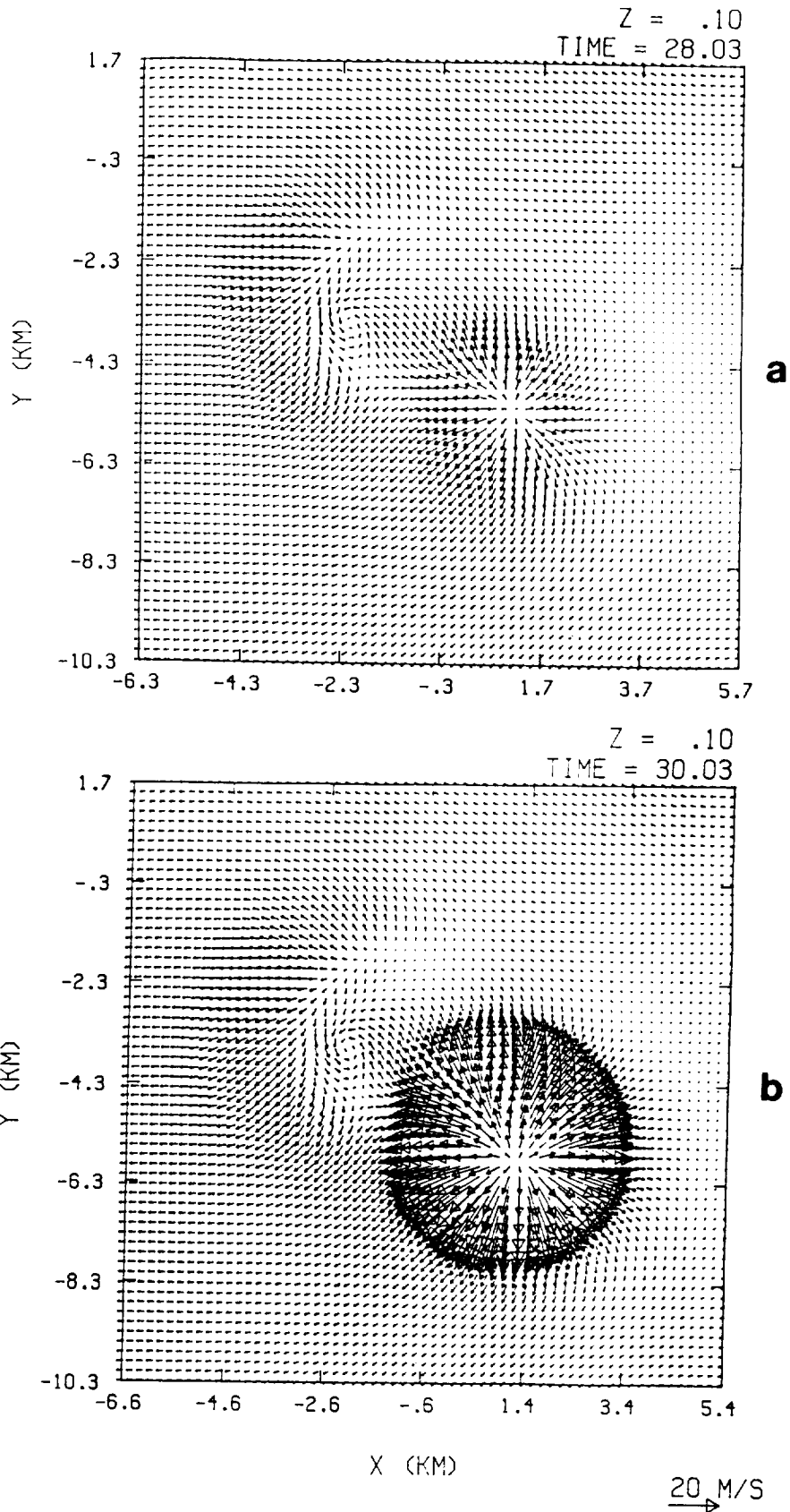


Fig. 25. Simulated low-level vector field for Case III at (a) 28 min and (b) 30 min.

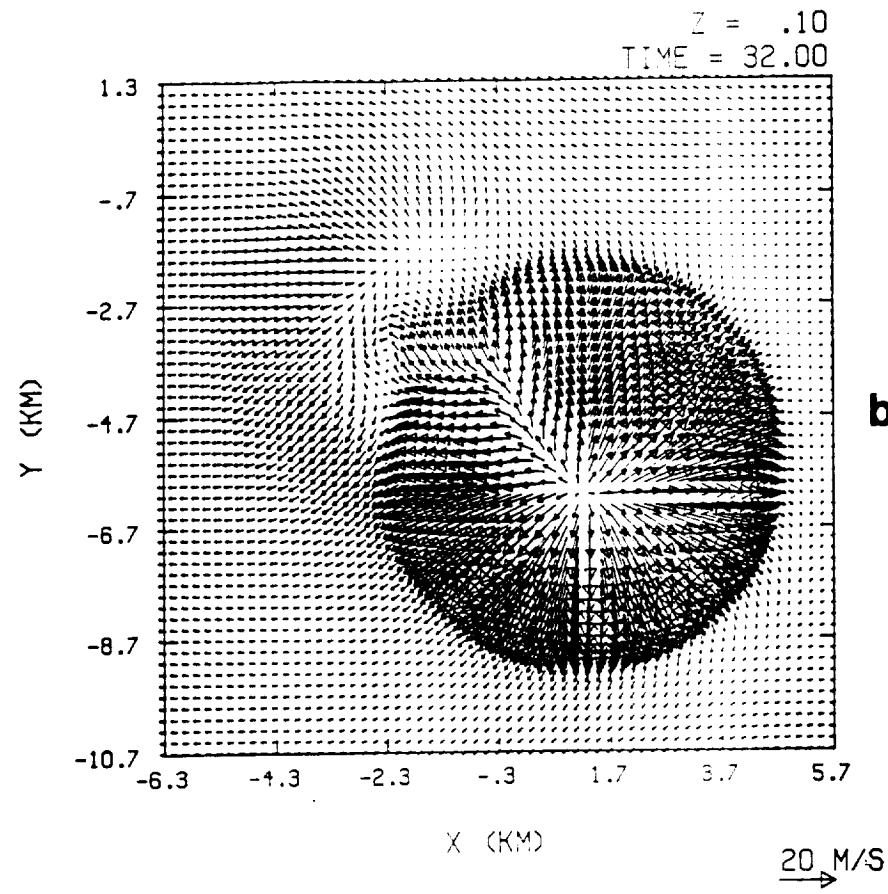
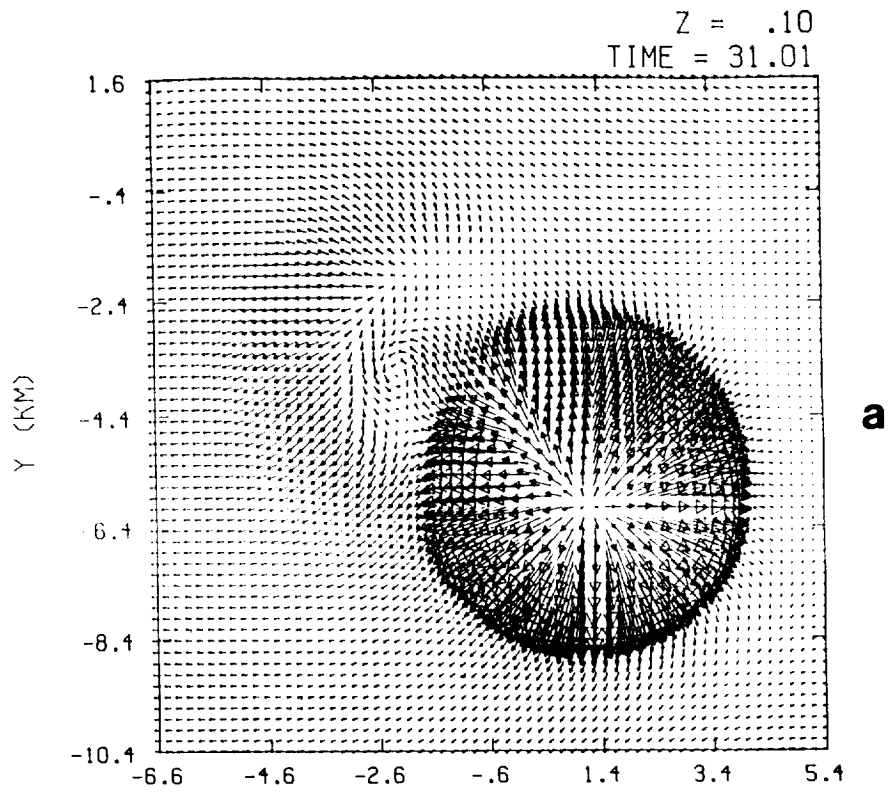
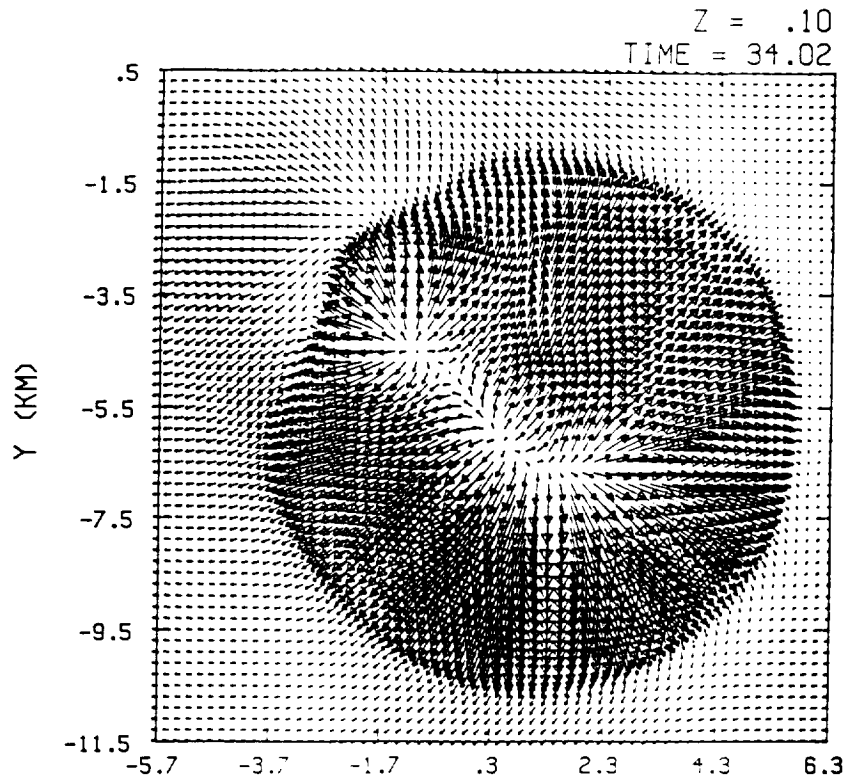
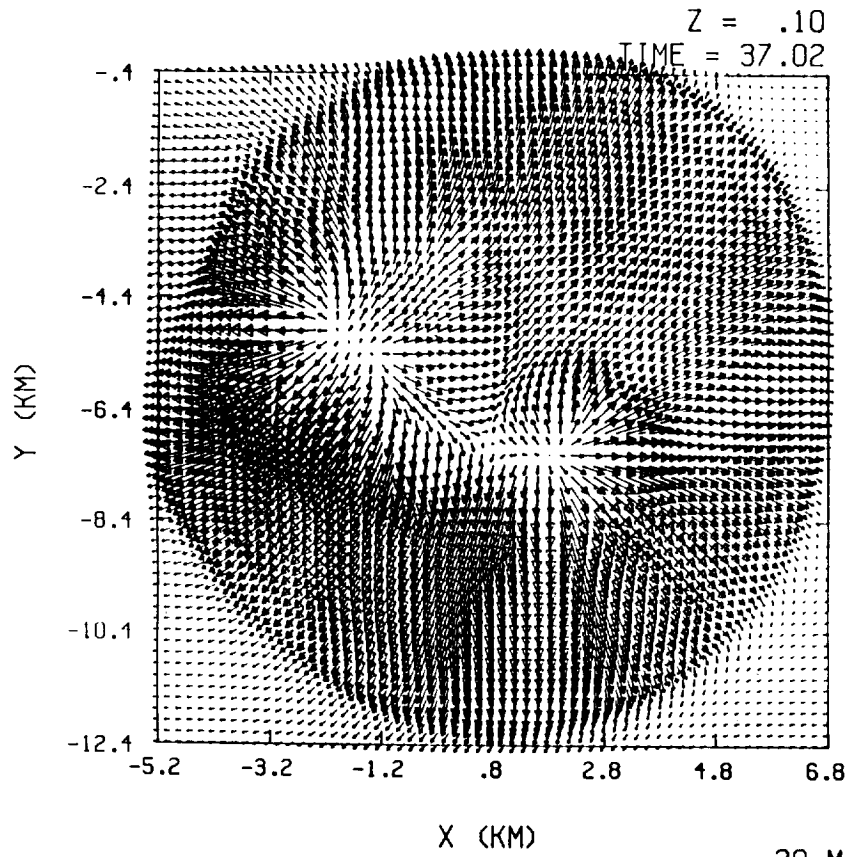


Fig. 26. Same as Fig. 25, but at (a) 31 min and (b) 32 min.



**a**



**b**

Fig. 27. Same as Fig. 25, but at (a) 34 min and (b) 37 min.

Figure 28 shows the low-level temperature perturbation field corresponding to the wind field in Fig. 27b. The temperature of the simulated downburst outflow ranges from 5°C to 12°C cooler than the environment; a general temperature drop of 8°C immediately follows the passage of the downburst gust front. These values compare favorably with an observed temperature drop of 7°C at DFW and an 8°C temperature drop based on the flight recorder of Delta 191 (Fujita, 1986).

An interesting feature evident in the sequence of low-level wind vectors (Figs. 25 - 27) is a cyclonic circulation NW of the initial downburst center. The circulation develops early in the thunderstorm lifetime, prior to the onset of any precipitation-cooled downdrafts. The circulation is collocated within an updraft, and adjacent to an arc-shaped area of subsiding air. The circulation apparently obtains its rotation from the shear induced by the region of warm, dry subsidence. The vortex intensifies with time until overtaken by the cold downburst outflow (see Figs. 26 and 27a). The simulated vortex occurred at the rear left flank of the storm (the storm is moving slowly southward), which is an area usually favored for tornado development. If a much finer grid resolution were to be assumed, a small, weak, and short-lived tornado might be resolved within this circulation. However, there were no reports of actual tornadoes; only strong winds were observed.

The diameter of the outflow at the ground, as derived from Fig. 5.9 in Fujita (1986) for the DFW microburst, is compared in Fig. 29 with the model simulation. Fujita's analysis of the DFW microburst dimensions was based on sparse data: three Low Level Wind Shear Alert System (LLWAS) anemometers to south and southwest of the microburst center, and data from the flight recorders of seven aircraft, including that from Delta 191. Despite the

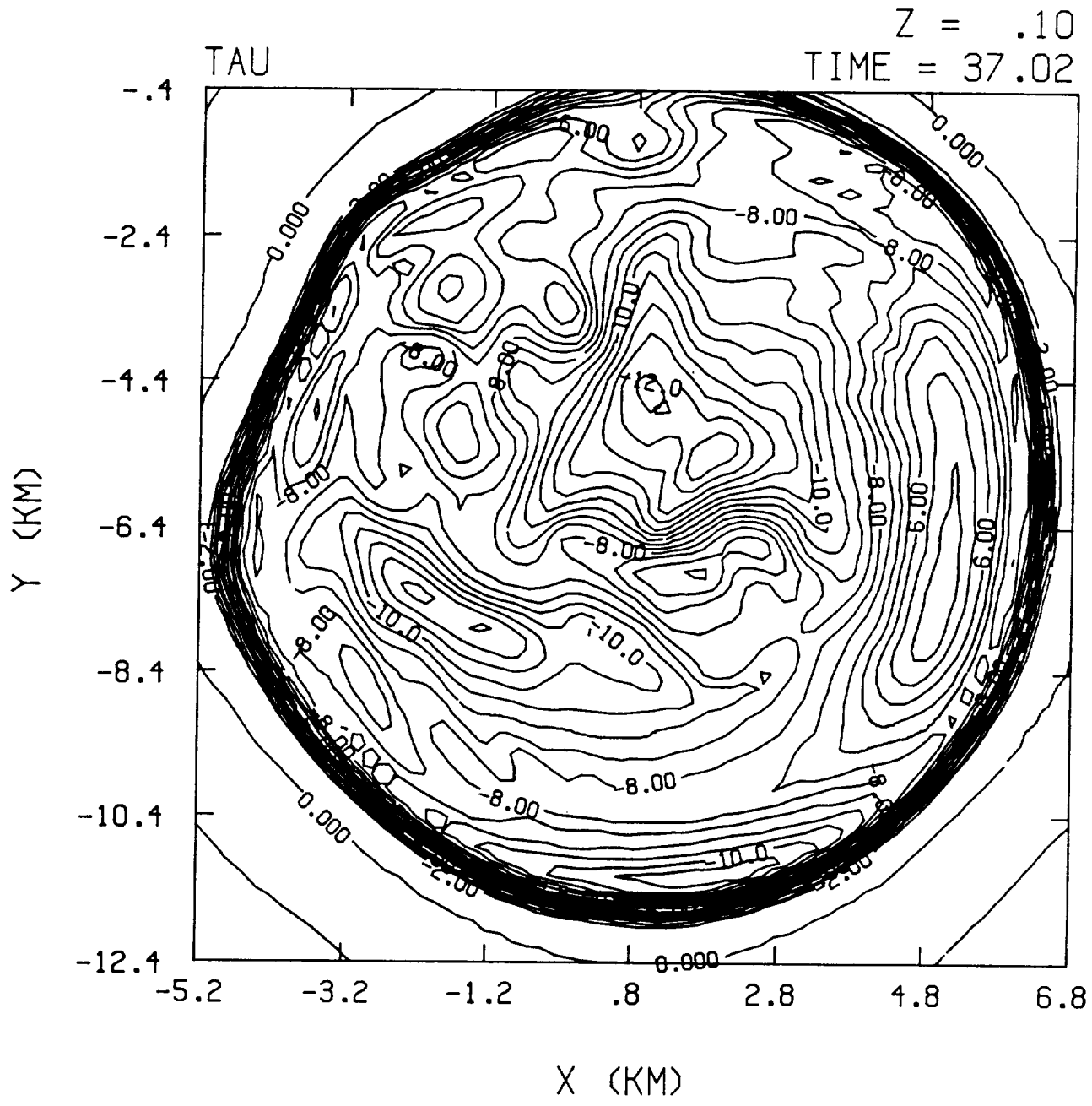


Fig. 28. Deviation of temperature from environment at 100 m AGL and 37 min. Contour interval is 0.5°C.

## DIAMETER OF THE OUTFLOW REGION AT GROUND

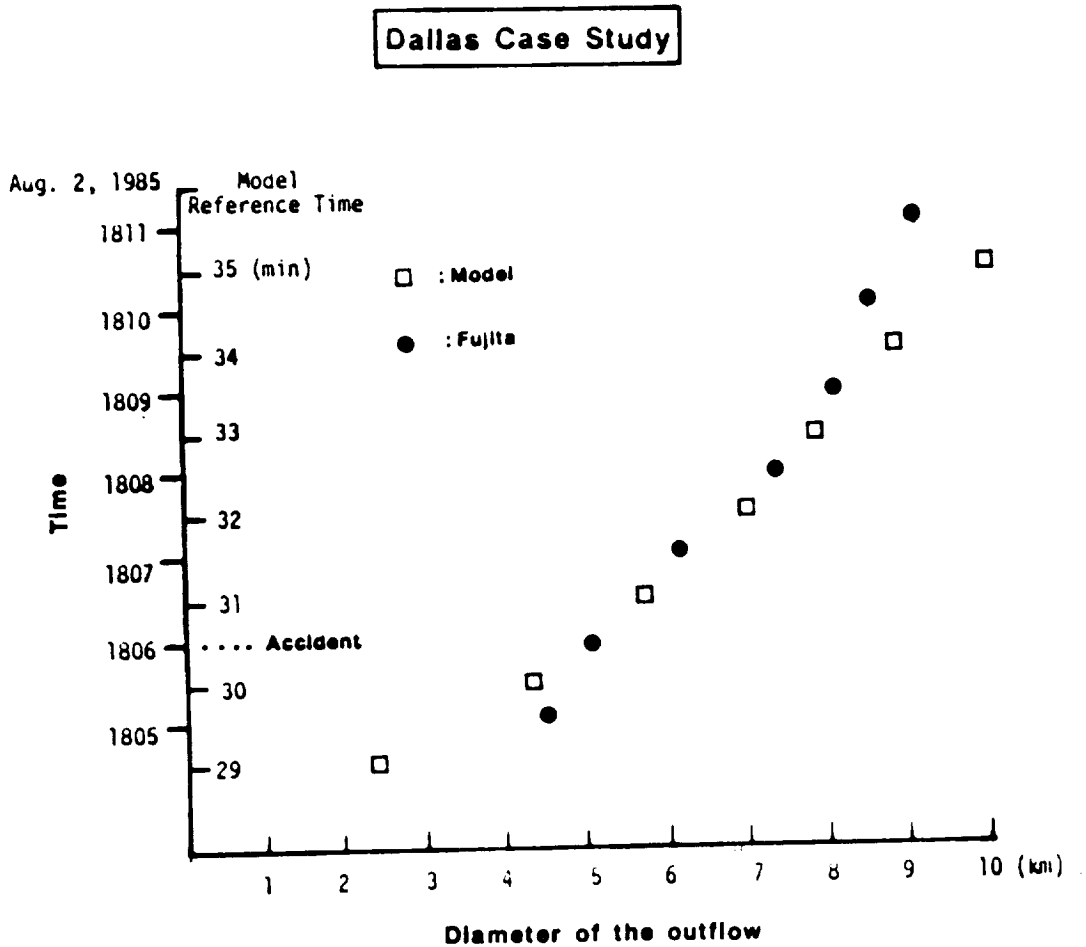


Fig. 29. Diameter of outflow at the ground as a function of time. Model data represented by squares. Solid circles represent estimated diameter of DFW microburst as computed from Fig. 5.9 in Fujita (1986).

sparsity of the observed data, the rate of expansion of the simulated microburst outflow is in good agreement with Fujita's estimations. Both show a rate of expansion of roughly  $20 \text{ m s}^{-1}$ . An even better agreement is found between the model results and Fujita's estimates, if the distance from the initial microburst center to the southernmost boundary of the outflow is plotted (Fig. 29). This parameter should be a more critical test of the model performance, since it is sensitive to the translation of the microburst. A closer agreement is found in Fig. 30 than Fig. 29, possibly because the observed data used in Fujita's estimates was less sparse on the south side of the microburst. The rate of southward propagation of the microburst gust front at its southernmost edge can be determined from Fig. 30 as approximately  $11.5 \text{ m s}^{-1}$ .

A matching of the observed time and the model simulation time is obtained by overlaying the curves for the outflow diameter, as in Figs. 29 and 30. The time of the aircraft accident (1806 CDT) can then be related to model time -- which is between 30 and 31 min. Hence according to the model simulation, the accident was approximately 3.5 min after the rain initially reached the ground; it is also at time when the outflow speed, rainfall rates, and wind shear are near their peak values (e.g., see Figs. 25 and 26). The time of the initial radar echo also matches well with observations. The simulated radar reflectivity first exceeded 30 dBZ at 13 min -- which is 17.5 min prior to the model time of the accident; the actual storm was first observed as a VIP level 2 (30 - 41 dBZ) cell, some 14 min prior to the crash (Salottolo, 1985; Fujita, 1986).

The simulated wind field near the time of the crash is depicted in Figs. 25b and 31. The latter figure is a Y-Z cross section taken through the center of the microburst. A ring vortex -- which is better resolved on

## DISTANCE FROM THE INITIAL MICROBURST CENTER TO SOUTHERNMOST BOUNDARY OF OUTFLOW

### Dallas Case Study

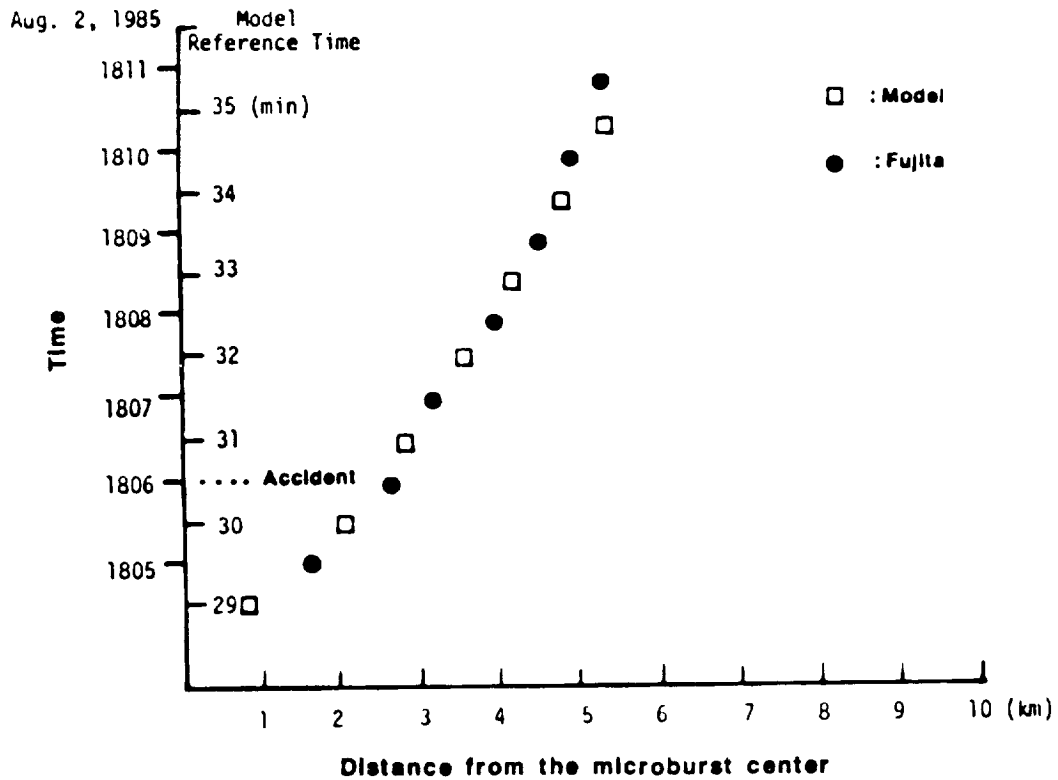


Fig. 30. Distance from the initial microburst center to the southernmost boundary of the outflow as a function of time. Symbols same as in Fig. 29.

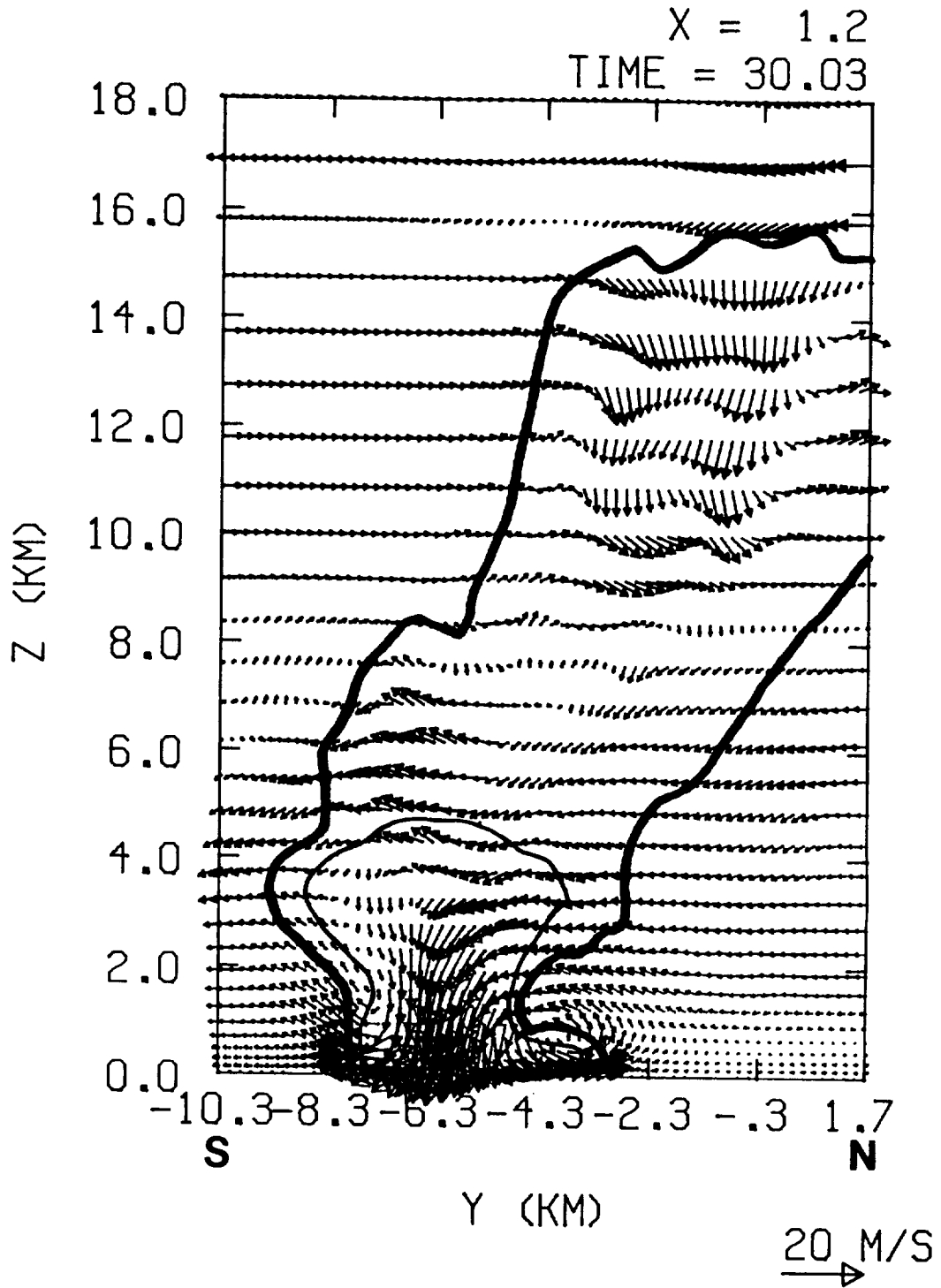


Fig. 31. South-north vertical cross section of the simulated wind vector field at 30 min for Case III. The thick curve outlines the 10 dBZ radar reflectivity contour, while the thin curve outlines  $0.2 \text{ g m}^{-3}$  rainwater contour.

the north side -- lags the leading edge of the expanding outflow. The downdraft which creates the strong outflow near the ground extends roughly up to the melting level (4.85 km AGL) and correlates well with the area occupied by rainwater (see Fig. 31). The intensity of this downdraft is strongly influenced by the evaporation of rain and the melting of hail. Downdrafts are found in the upper portions of the storm, but do not extend to the ground. Downdrafts are difficult to maintain above the melting level, since cooling due to sublimation of hail, graupel, or snow is usually not sufficient to compensate for the compressional warming experienced by the descending air (except in the case of very weak downdrafts).

Hail (Fig. 32) reaches the ground in the simulation, in spite of ambient surface temperatures of 38°C, and a melting level located at relatively high altitudes. Hail is able to reach the ground before completely melting, because the intense downdrafts -- with downward speeds of up to 18.5 m s<sup>-1</sup> -- greatly reduce the time for hail to fall to the ground. Thus, not surprisingly, the model simulation shows that hail at ground level is only found within the downdraft cores. The actual occurrence of hail in the DFW microburst was suspected from radar observations (Salottolo, 1985); and quarter-sized hail was observed following the accident by one of the surviving crash victims (Daily Press, 1985).

Ground-level pressure readings have been suggested by Bedard (1984) and Bedard and LeFebvre (1986) as a possible tool for the detection of microbursts in the Terminal Area. Fig. 33 shows the simulated pressure deviation at 2.5 min prior to the model time of the DFW crash. In Fig. 33, the pressure dome has a peak deviation of 1.7 mb and is roughly 5 km in diameter. The low-level wind field at this time (Fig. 25a) is still quite

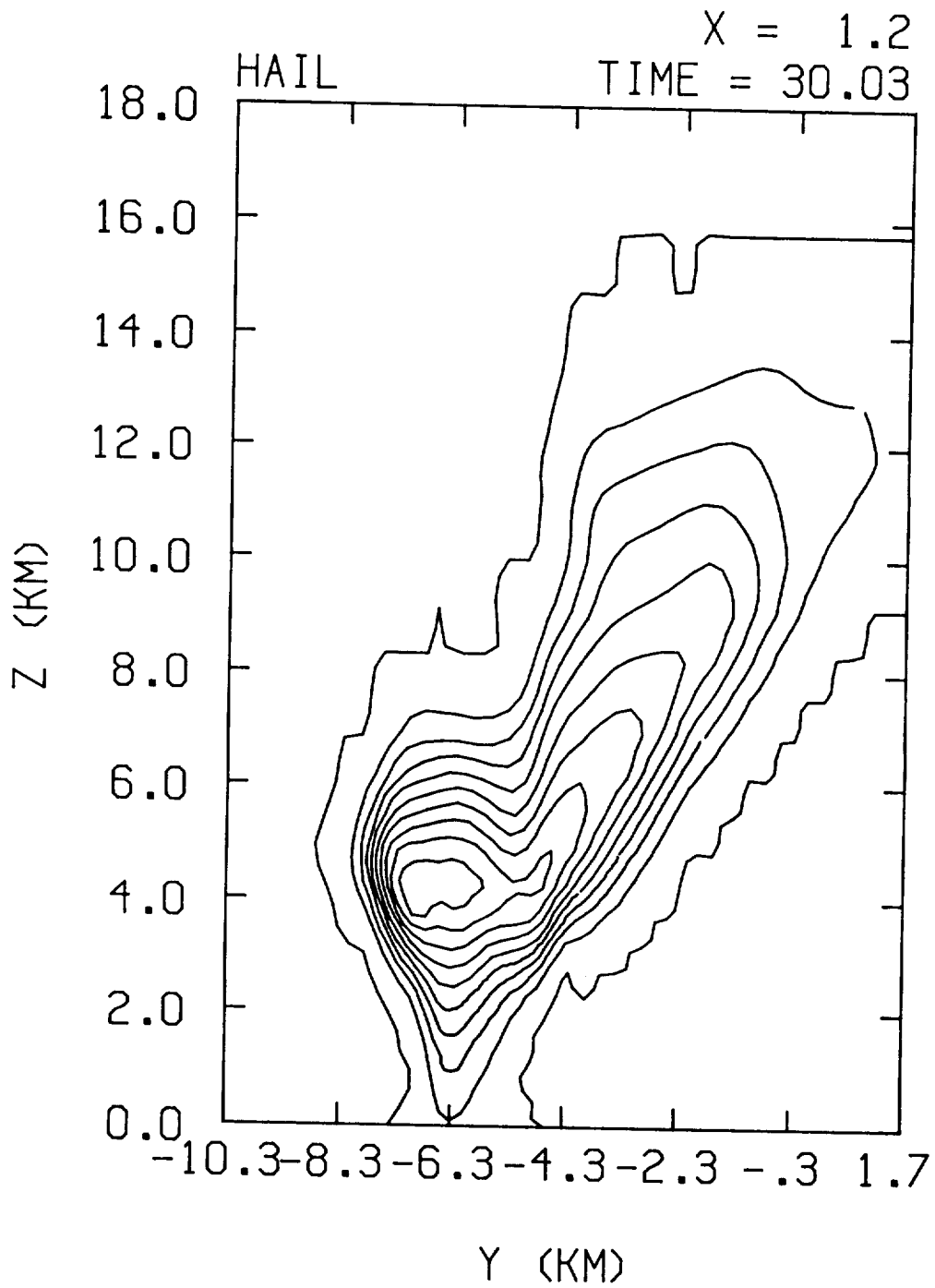


Fig. 32. Same as Fig. 31, but the field is for hail water. The contour interval is  $0.2 \text{ g m}^{-3}$  of hail water.

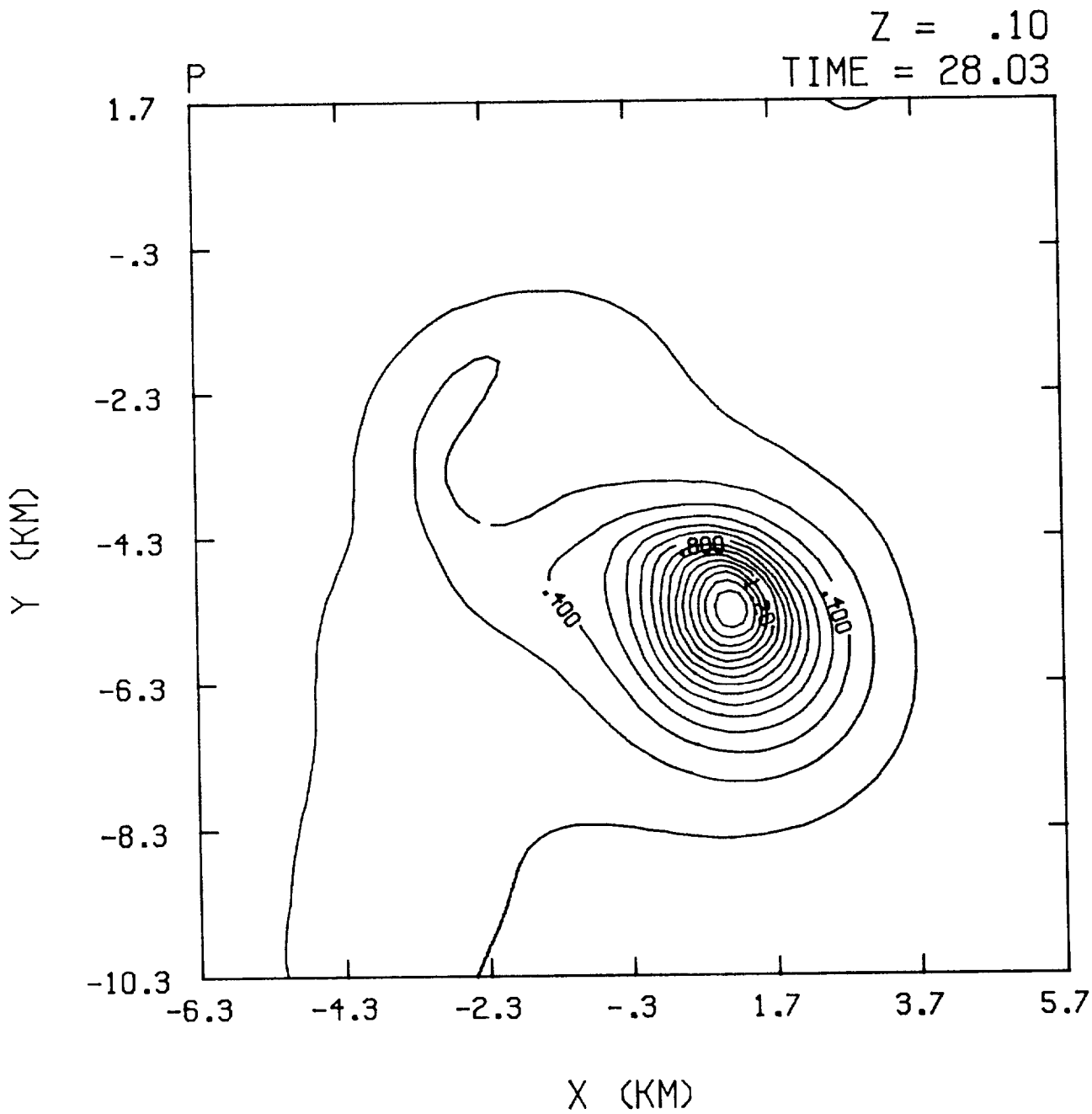


Fig. 33. The horizontal cross section of the simulated deviation pressure at 100 m AGL and 28 min for Case III. The contour interval is 0.1 mb.

weak. The pressure dome forms in order to accelerate the low-level air away from the impinging downdraft, and therefore, precedes the strong outflow winds. The model results suggest that the detection of the microburst pressure field could provide several minutes of warning time. But, a high-resolution network of pressure sensors would be needed in order to resolve the microburst pressure dome.

#### Summary for Case III

A downburst producing thunderstorm is simulated which has many of the characteristics of the storm that occurred at DFW on 2 August 1985. In agreement with observations, the horizontal scale of the model storm was relatively small (less than 9 km across), extended to an altitude of 15 to 16 km AGL, and had an intense radar echo. Good agreement was also found for: (1) the storm speed and direction of propagation, (2) the rate of expansion of the low-level outflow, (3) the propagation speed of the downburst gust front, (4) the presence of hail and heavy rain at the surface, (5) strong low-level outflow and large horizontal wind shears, and (6) a significant temperature drop (roughly 8°C) at the surface.

The model storm produced an intense microburst which rapidly expanded into a macroburst. The rate of expansion of the simulated downburst closely matched that analyzed by Fujita (1986) from flight recorder data and LLWAS anemometer data. In the simulation the peak outflow and downdraft speeds were  $22 \text{ m s}^{-1}$  and  $18.5 \text{ m s}^{-1}$ , respectively. The outflow expanded in a near symmetrical fashion at a rate of approximately  $20 \text{ m s}^{-1}$ . The peak horizontal wind shear contained in the outflow was  $35 \text{ m s}^{-1}$  over a distance of 3 km. As in other downburst simulations with the 2-D axisymmetric version of TASS (Chuang et al., 1984; Proctor, 1985a), the peak outflow

speeds were associated with a ring vortex which expanded outward lagging the leading edge of the outflow. As the simulated microburst expanded into a macroburst, multiple downdraft centers develop and appear as microbursts embedded within the macroburst outflow. Simulated downdrafts associated with the intense microburst outflow only extended upward to near the melting level. The evaporation of rain appears to provide a major driving force for the low-level downdrafts and associated outflow.

According to the simulation the microburst winds intensified suddenly, just prior to the accident time. The aircraft accident time was related to model time by matching the rate of expansion curves in Fig. 29. The accident time is near the time in which the simulated peak outflow speeds, wind shears, and precipitation rates occurred. According to the simulation, rainfall first reached the ground only 3.5 min prior to model accident time, and the peak low-level winds increased from  $6 \text{ m s}^{-1}$  to  $20 \text{ m s}^{-1}$  during the 2.5 min prior to the crash. Hence, these results indicate that very little warning time for a specific microburst event would be possible, if based only on the surface level winds. The warning time could be improved by the detection of the microburst pressure dome which precedes the peak winds by several minutes. However, successful detection of the pressure dome may require a high resolution network of pressure sensors.

## 5. CASE IV: SOUTH FLORIDA CONVECTIVE COMPLEX

Two cumulonimbus systems were observed in the Florida Area Cumulus Experiment (FACE) mesonetwork area on 25 August 1975. An investigation of these South Florida convective systems has been reported by Cuning et al. (1986a, 1986b). The first complex formed within a confluence zone and developed towers up to approximately 13 km; some of the cells, however, developed only up to 6 km. New cells formed along the north and south flanks of the older cells, possibly induced by the precipitation cooled outflow. The updrafts in the convective complex were reported to have a discrete bubble-like structure; this was also true for the downdrafts as well. The cumulonimbus complex maintained its size and intensity for several hours, as new cells replaced decaying cells. A second and more intense convective complex trailed the first system. The radar echo of the first system was elongated in an east-west direction, while the second system was elongated in a north-south direction. The second system may have been modified by the first system.

For this Case experiment we will attempt to simulate the first complex (Convective System I) only. According to Cuning et al. (1986a) the first complex was seeded with silver iodide flares soon after the initial towers had grown above 12 km. The second complex was seeded beginning with the growth of the initial towers. The effects of seeding are not included in the simulation, although it may have altered the development and intensity of the convection to some degree.

### Initial Conditions for Case IV

The horizontal size of the domain is chosen as 15 km  $\times$  15 km and is resolved by a 250 m grid size. The vertical depth of the domain is 16 km

and is resolved by 31 layers with the stretching coefficients specified as in Cases I and II. This gives a vertical spacing which varies from approximately 240 m near the ground to approximately 800 m near the top boundary.

The sounding for this case is shown in Fig. 34. The sounding was observed near the time and location of the development of the first convective system. Unfortunately, the winds above 825 mb level were unavailable and were instead taken from the 0800 EDT Miami sounding.

A maritime cloud droplet spectrum is assumed for this Case, even though Sax and Hudson (1981) have found that the cloud condensation nuclei over South Florida are characteristic of continental areas much of the time. Specifically,  $n_{CD}$  is set equal to  $100 \text{ m}^{-3}$  and  $\sigma$  is set equal to 0.35. The sensitivity of these parameters has not been examined.

Convection is triggered in the model simulation by a 2.5 km radius thermal impulse. Only the simulation of the first convective complex is attempted. Other initial parameters are depicted in Table 1.

#### Results for Case IV

In the early part of the simulation, a single updraft develops from the specification of the initial perturbation field. The surface pressure deviation beneath this cell drops to a minimum of -0.2 mb. This value compares reasonably with the minimum values observed in the FACE mesonet network: minimum pressure deviations of -0.13 mb and -0.30 mb were observed underneath developing cells in system I and II, respectively (Cunning et al., 1986a).

The simulated radar reflectivity structure at 33 min (Fig. 35) is somewhat similar to the observed radar reflectivity shown in Fig. 36. The

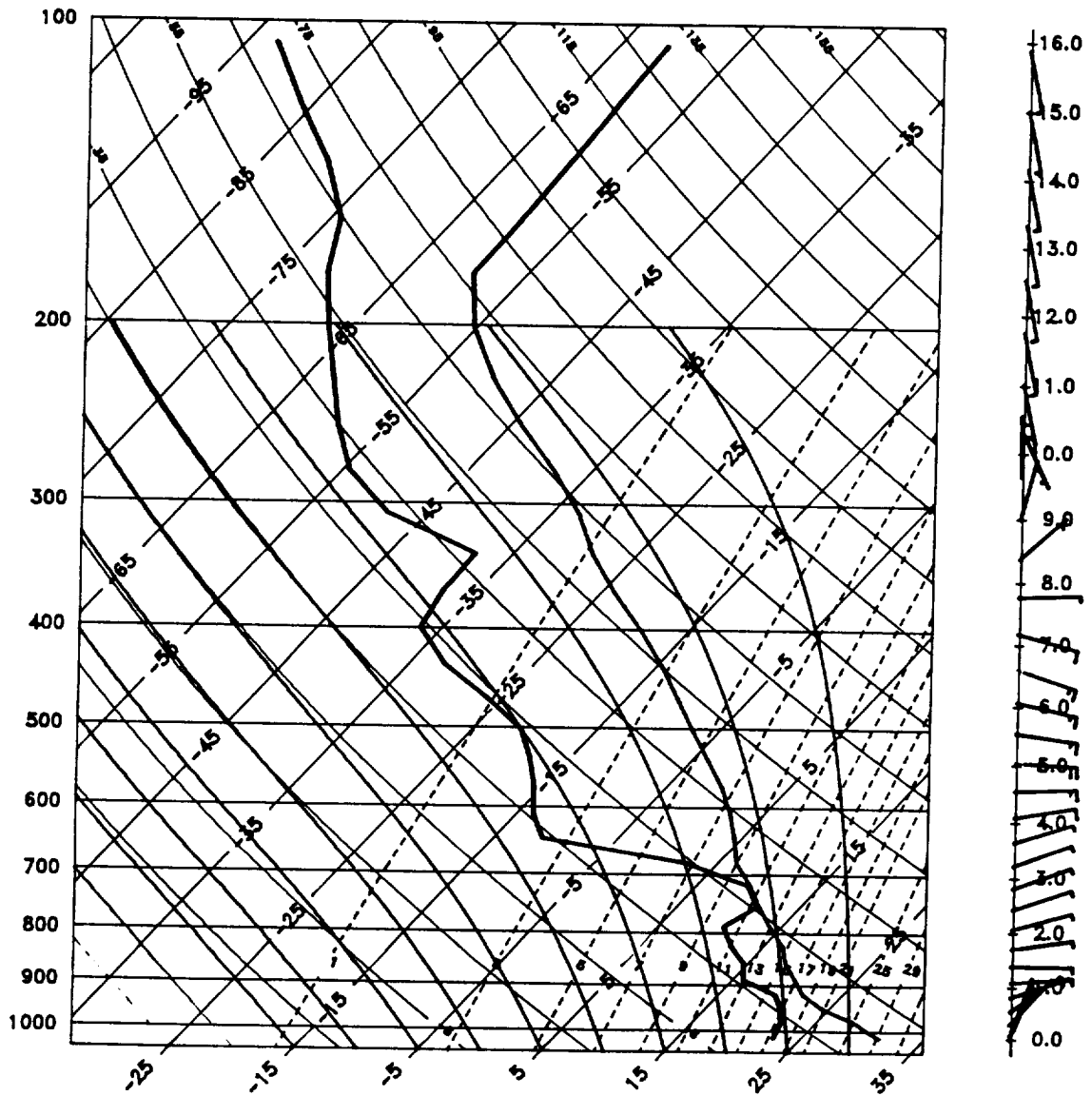


Fig. 34. Same as Fig. 1, but observed at Field Observing Site (FOS) in FACE network at 1345 EDT on 25 August 1975. Winds above 825 mb level taken from Miami 0800 EDT sounding.

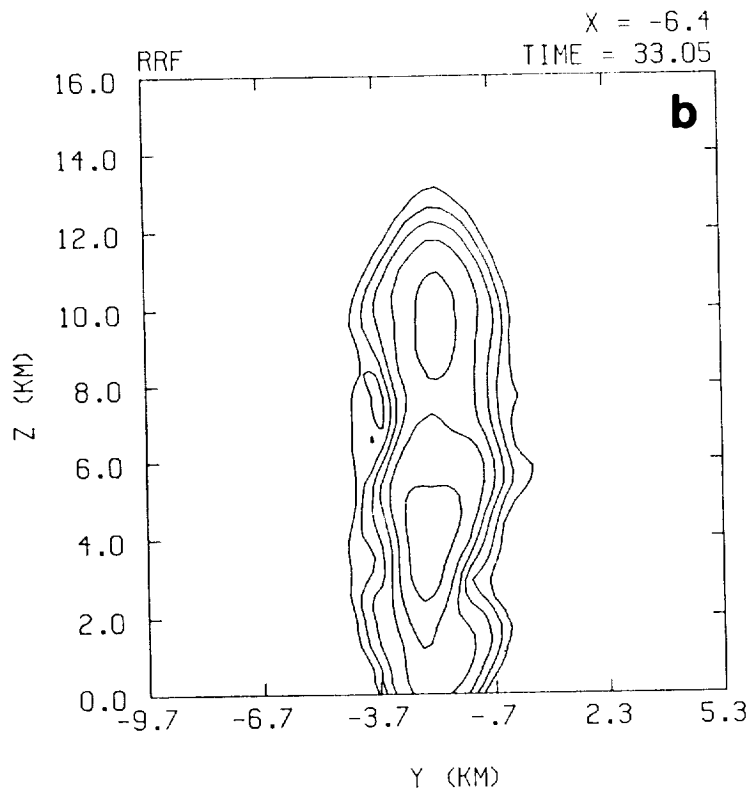
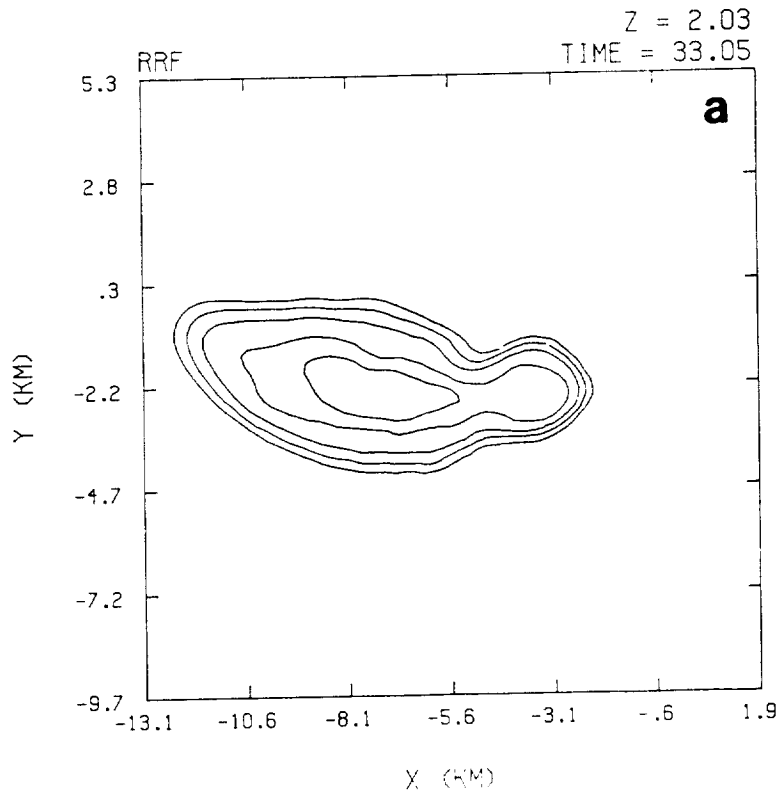


Fig. 35. Simulated radar reflectivity at 33 min for Case IV. The fields are (a) horizontal cross section at 2 km AGL and (b) vertical north-south cross section at  $x = -6.4$ . The contours begin at 10 dBZ and increment by 10 dBZ.

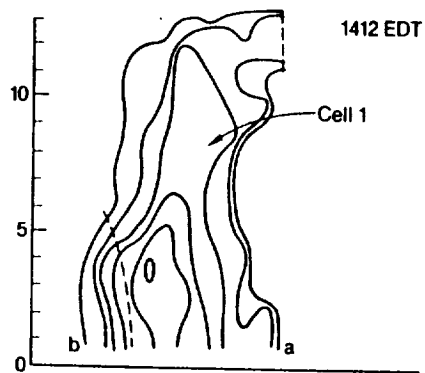
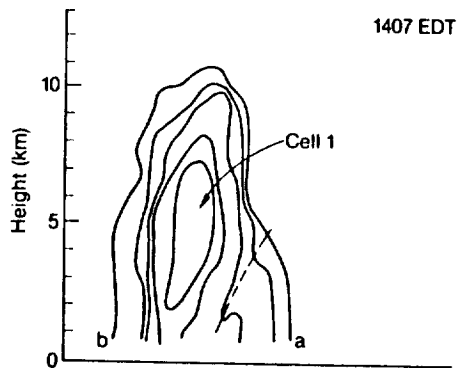
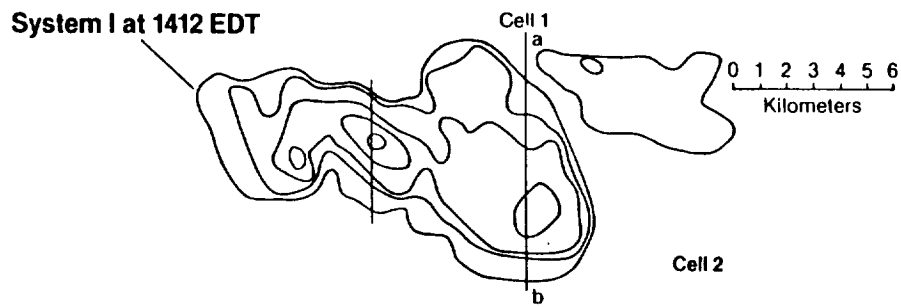


Fig. 36. The radar reflectivity of cell observed in FACE network. Contours are 10, 20, 30, 40, 45, and 50 dBZ (taken from Cuning et al., 1986).

simulated radar reflectivity is greater than 60 dBZ, which is about 10 dBZ larger than was observed. The structure of the simulated radar echo, including the horizontal and vertical dimensions, compare roughly with the observed echo in Convective System I. For instance, both the observed and simulated radar echoes in Figs. 35 and 36 are (1) elongated toward the WNW with a maximum near the center, (2) have a secondary maximum on the east side, (3) are much taller in the vertical than they are wide in the north-south direction, (4) have a peak altitude of approximately 13 km, and (5) have a peak reflectivity at about 4 km elevation.

The outflow from the simulated cell (Fig. 37) is much weaker than found in Case III (cf., Figs. 25 and 26), even though rainfall rates were comparable. The simulated peak outflow speed is  $8 \text{ m s}^{-1}$  and the peak rainfall rate is  $65 \text{ mm hr}^{-1}$ . The maximum rainfall rate observed in the FACE network for System I was  $40 \text{ mm hr}^{-1}$  (Cunning et al., 1986a). Peak winds in the FACE network were unavailable at the time of writing this report. No hail or graupel reached the ground in the simulation, nor was any observed.

In the simulation, precipitation-cooled outflow triggers the development of other cells, thus forming a convective complex. The convective complex was maintained throughout the 54 min simulation. However, only the initial cell developed to a height of 13 km, with the other cells developing no deeper than 6 km. The propagation of the simulated radar echo (at 2 km AGL) was  $6 \text{ m s}^{-1}$  from  $81^\circ$ . The observed propagation speed was from the east at  $6.5 \text{ m s}^{-1}$  (Cunning et al., 1986b). A comparison of the peak temperature departures was also favorable. The rain cooled air produced peak temperature departures of up to  $8^\circ\text{C}$  in both the observation (see Cunning et al., 1986a) and the simulation.

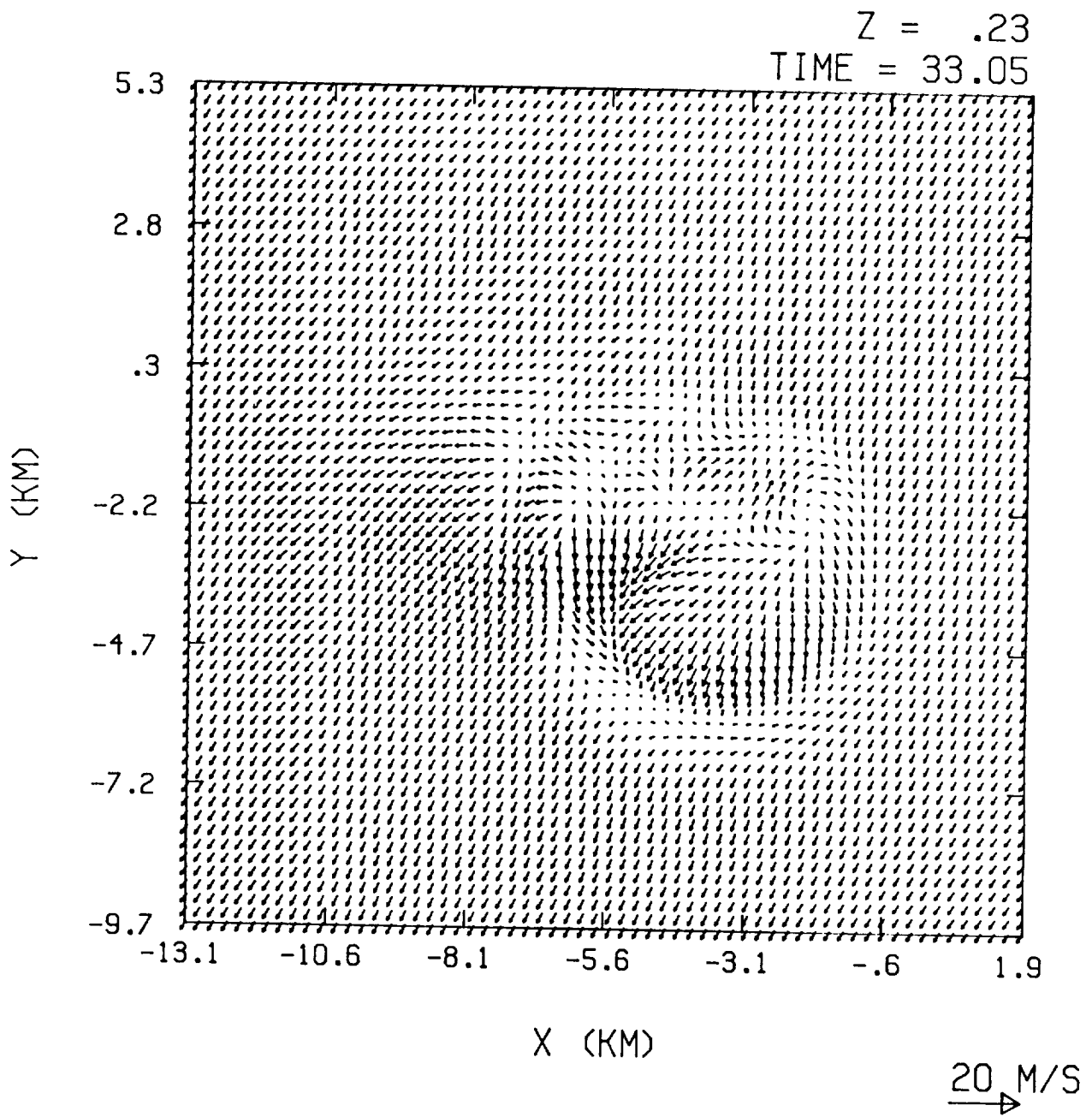


Fig. 37. Same as Fig. 25, but for Case IV at 33 min.

The simulated development of secondary cells adjacent to a precipitating anvil are depicted in Figs. 38 and 39. The time sequence of cloud perspectives in Fig. 38 depicts two developing lines of clouds to the north and south of the anvil cloud. The anvil is the only remaining part of the cloud from the initial cell. Fig. 39 shows a time sequence of south-north vertical cross sections through the most active cell, which is occurring along the southern flank of the outflow. Evident in Fig. 39 is a weak downdraft which coexists with precipitation falling underneath the anvil cloud, and discrete updraft bubbles located on the north and south flanks of the downdraft. From the actual observations, Cuning et al. (1986b) found that the updrafts and downdrafts had a discrete bubble-like structure and the radar reflectivity had a more continuous structure. This also is confirmed in the simulated fields shown in Fig. 39.

#### Summary for Case IV

A South Florida convective complex is simulated and has favorable comparisons with observations reported by Cuning et al. (1986a, 1986b). The simulation shows the development of updraft cells induced by precipitation-cooled outflow from the initial cell. As in the actual observations, the simulated updrafts and downdrafts appear as discrete bubbles. The simulated radar reflectivity structure, on the other hand, has a continuous structure.

The outflow simulated in this Case was much weaker than simulated for the DFW microburst in Case III, even though the peak rainfall rates were nearly the same ( $65 \text{ mm hr}^{-1}$  for this Case vs.  $80 \text{ mm hr}^{-1}$  for Case III). The peak outflow speed for this Case is  $8 \text{ m s}^{-1}$  which is considerably less than the  $22 \text{ m s}^{-1}$  simulated in Case III.

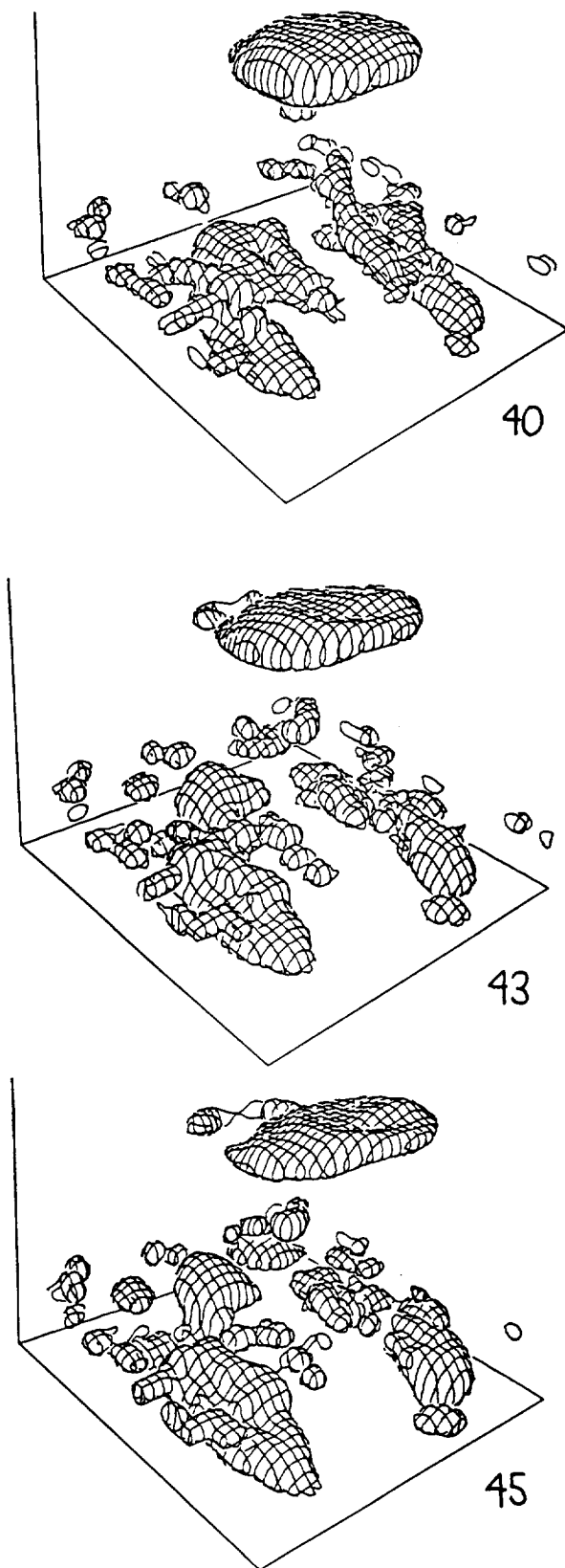


Fig. 38. Same as Fig. 19, but for Case IV at 40, 43, and 45 min. Perspectives viewed from southeast. The horizontal area is windowed to 40 km  $\times$  40 km.

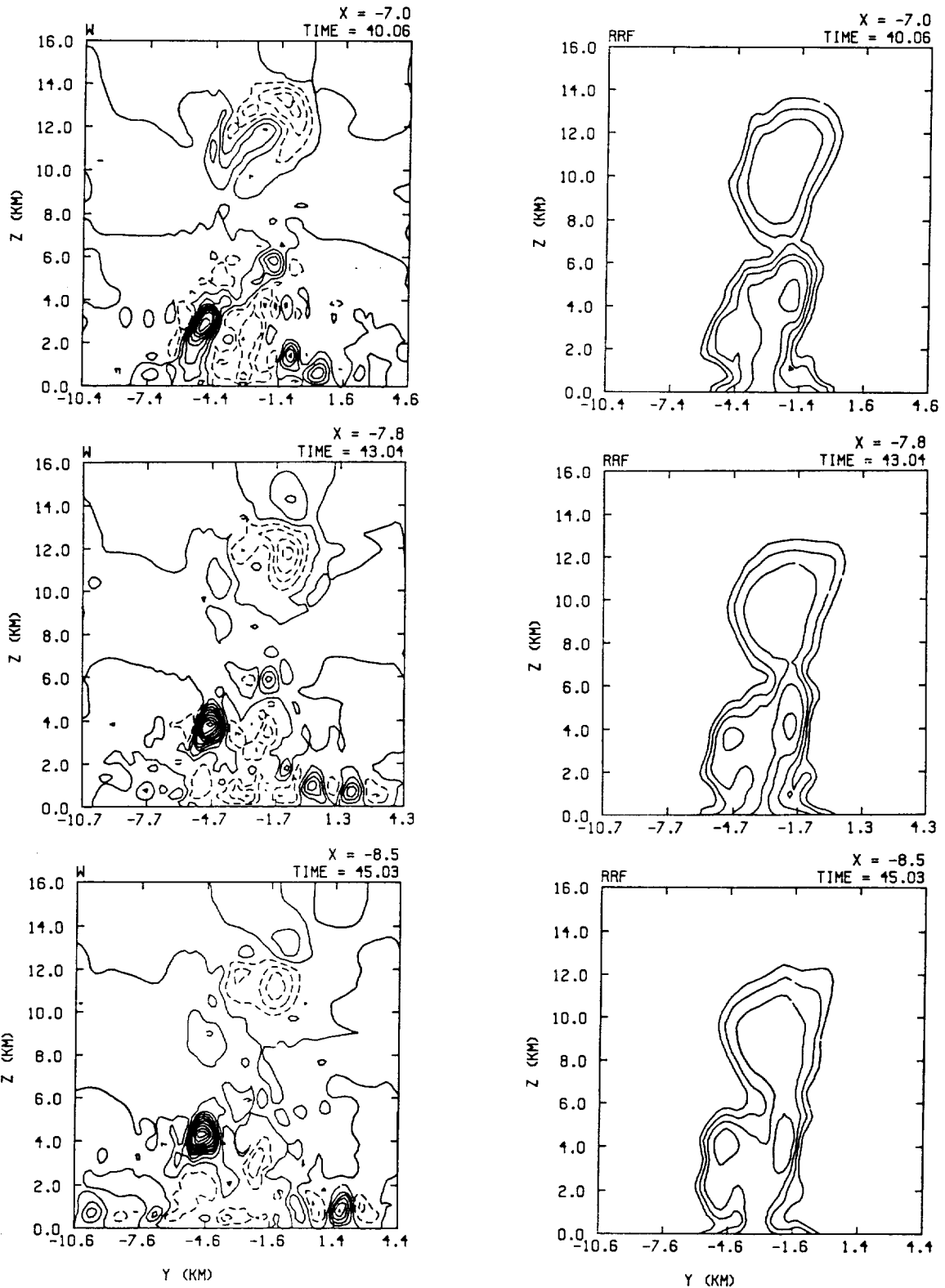


Fig. 39. Simulated north-south vertical cross sections of vertical velocity (left) and radar reflectivity (right) for Case IV. The top, middle, and bottom rows are taken at 40, 43, and 45 min, respectively. The contour interval for vertical velocity is  $1 \text{ m s}^{-1}$  with negative values dashed, and the contours for radar reflectivity start at 10 dBZ and increment by 10 dBZ.

The sensitivity of the results to the assumed cloud droplet spectrum and the initial perturbation field has not been investigated.

Levy and Cotton (1984) have conducted several simulations of this Case using the Colorado State University three-dimensional cloud/mesoscale model (e.g., Cotton et al., 1982; Tripoli and Cotton, 1982). Their experiments assumed a larger but more coarsely resolved domain, with horizontal and vertical grid sizes of between 500 m and 750 m. The results presented by Levy and Cotton did not appear to be similar to the TASS results for this Case.

## 6. CASE V: OKLAHOMA TORNADIC THUNDERSTORM

During the afternoon of 20 May 1977 and through the very early hours of the next day, severe storms in Oklahoma spawned at least 16 tornadoes. Several of these severe storms were observed during a significant portion of their lifetimes by as many as four Doppler radars. Ray et al. (1981) examined three of these storms, two of them tornadic and one of them a hailstorm, at various times during each storm's evolution. One of the storms, named the Del City storm, has also been studied by Brandes (1981, 1984) and Klemp et al. (1981). The analyzed storms possessed at least some of the characteristics of supercells during parts of their lifetimes; they developed mesocyclones and hook-echo radar signatures, and propagated to the right of the 700 mb wind. Although tornadoes were spawned by two of the storms, the tornado wind fields could not be resolved by the Doppler radars. However, areas of large vertical vorticity were detected in the regions of the mesocyclone where tornadoes did occur. The analysis of the Doppler radar data also showed that the horizontal configuration of the updraft changed near the time of tornadogenesis. The low-level updraft developed a horseshoe-like structure as a tongue of rainy downdraft air spiralled into the updraft center from the west and south. The peak vorticity and possibly the tornado occurred to the south and east of the storm updraft maximum -- between the updraft maximum and the tongue of inflowing downdraft air. Klemp et al. (1981), using the Klemp-Wilhelmson model (1978), were able to simulate many of the basic features of the Del City storm; but, with a horizontal grid mesh of 1 km, they were unable to resolve the horseshoe-shaped, low-level updraft structure, as well as many of the smaller scale features associated with the tornado phase. The above model experiment was further investigated by Klemp and Rotunno (1983); they

reduced the horizontal grid size by a factor of 4, and re-initialized at the intense phase of the coarser-grid simulation. With the 250 m horizontal grid size, they were able to resolve more detail, including the occlusion of the storm updraft by the rear downdraft. However, the grid mesh was still too coarse to resolve the tornado vortex.

The simulation of this case will allow us to evaluate how well the TASS model can simulate an Oklahoma tornadic thunderstorm. Although we do not expect to resolve the tornado, due to the coarseness of the mesh, we do expect to resolve many of the features of a tornadic supercell storm.

#### Initial Conditions for Case V

The domain size assumed for this Case is roughly comparable to that assumed by Klemp et al. (1981) in their simulation of the Del City storm. The horizontal size of the domain is 45 km  $\times$  45 km and the vertical depth of the domain is 18 km. The domain has a horizontal grid size of 750 m and a stretched vertical grid spacing which increases from approximately 240 m near the ground to approximately 900 m near the top boundary.

The model initial and reference conditions are based on the sounding shown in Fig. 40, which represents an estimate of the conditions near the Del City storm. The temperature and moisture profiles in Fig. 40 are composited from the 1500 CST Ft. Sill sounding and the 1622 CST Elmore City sounding, each of which are shown in Fig. 2 of Klemp et al. (1981). The composite sounding has a Lifted Index of  $-8^{\circ}\text{C}$  and may be biased toward having greater potential instability than what may have actually occurred. A smooth hodograph of the winds composited from the Ft. Sill and Elmore City soundings is shown in Fig. 3 of Klemp et al. The model ambient wind profile above 444 m AGL is based on this composite hodograph, while below 444 m the

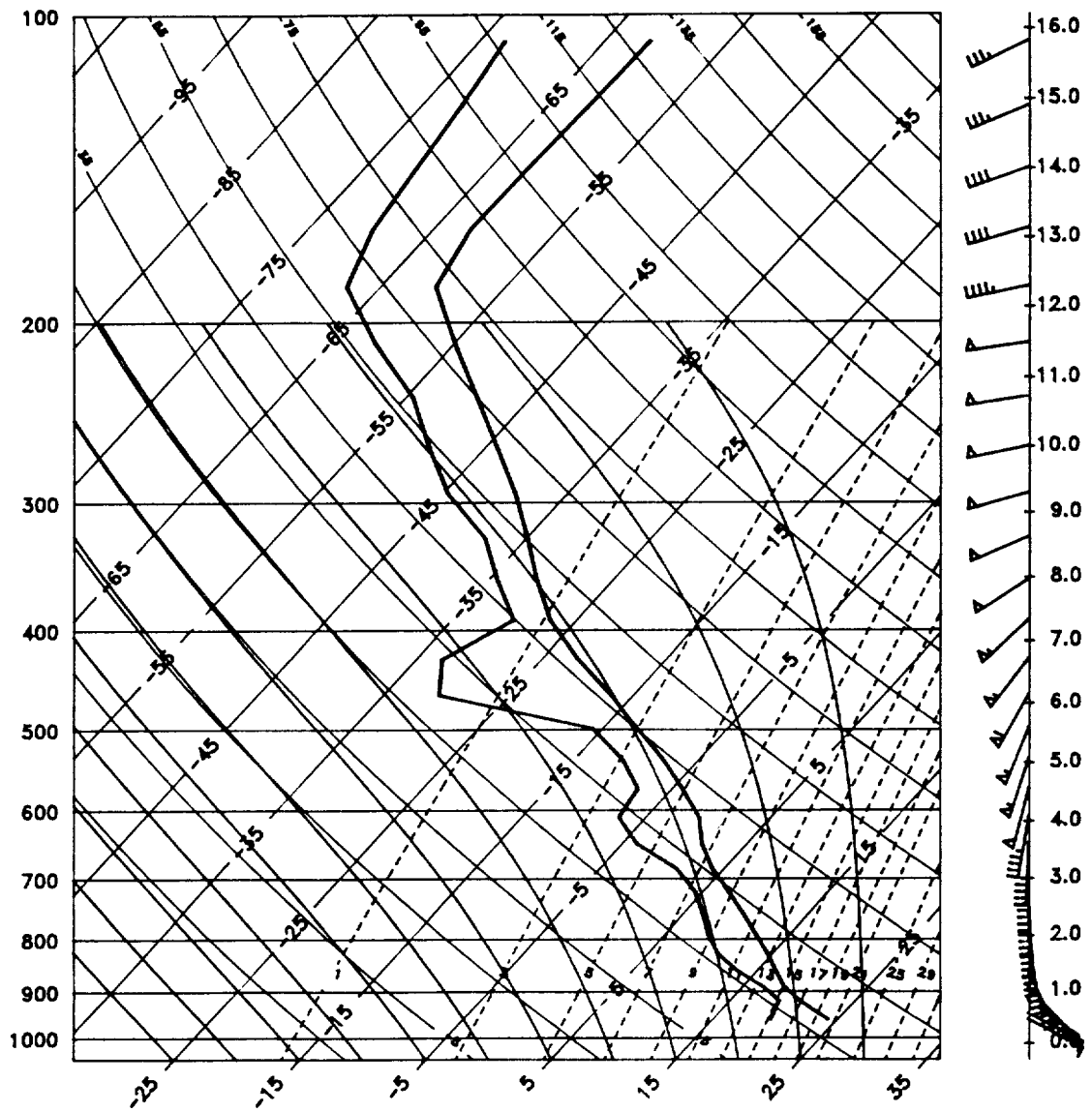


Fig. 40. Composite sounding for Del City, Oklahoma on 20 May 1977. Above 444 m AGL, composite winds taken from Fig. 3 in Klemp et al. (1981). Below 444 m, winds taken from mean tower data presented in Fig. 1 of Johnson (1985).

model profile is based on wind tower data observed near the Del City storm which is shown in Fig. 1 of Johnson (1985). Other initial specifications for this Case can be found in Table 1.

#### Results of Case V

This experiment produced a long-lasting storm having many characteristics of a supercell storm. The modeled storm had many similarities with the simulation described in Klemp et al. (1981).

The simulation of this Case was carried out through 175 min. During the first 50 min the modeled storm traveled with a mean speed of  $14 \text{ m s}^{-1}$  and toward a direction of  $352^\circ$ . Following this time, the propagation of the model storm deviated to the right, and the storm began to acquire a quasi-steady supercell structure. Between 50 and 170 min, the speed and direction of storm propagation was  $13 \text{ m s}^{-1}$  at  $11^\circ$ . This value is reasonably close to the observed values. Several of the severe storms during the 20 May outbreak were reported to be moving at  $11.5 - 17.5 \text{ m s}^{-1}$  toward  $10^\circ - 30^\circ$  (e.g., Ray et al., 1981; Brandes, 1981).

The model storm develops a well-defined radar hook-echo structure after 50 min and is maintained throughout the remainder of the simulation. Fig. 41 shows the simulated hook echo at 100 min. In Fig. 41 the modeled hook echo has an anticyclonic flare at its southernmost tip. A well-defined hook echo with an anticyclonic flare also appears in the Doppler analysis of the Del City storm (Brandes, 1981, 1984; Ray et al., 1981). This region is a potential area for secondary tornado formation. In the 3 June 1980 Grand Island, Nebraska tornado outbreak, Fujita (1981) detected an anticyclonically rotating tornado in association with an anticyclonic flare at the tip of an observed hook echo.

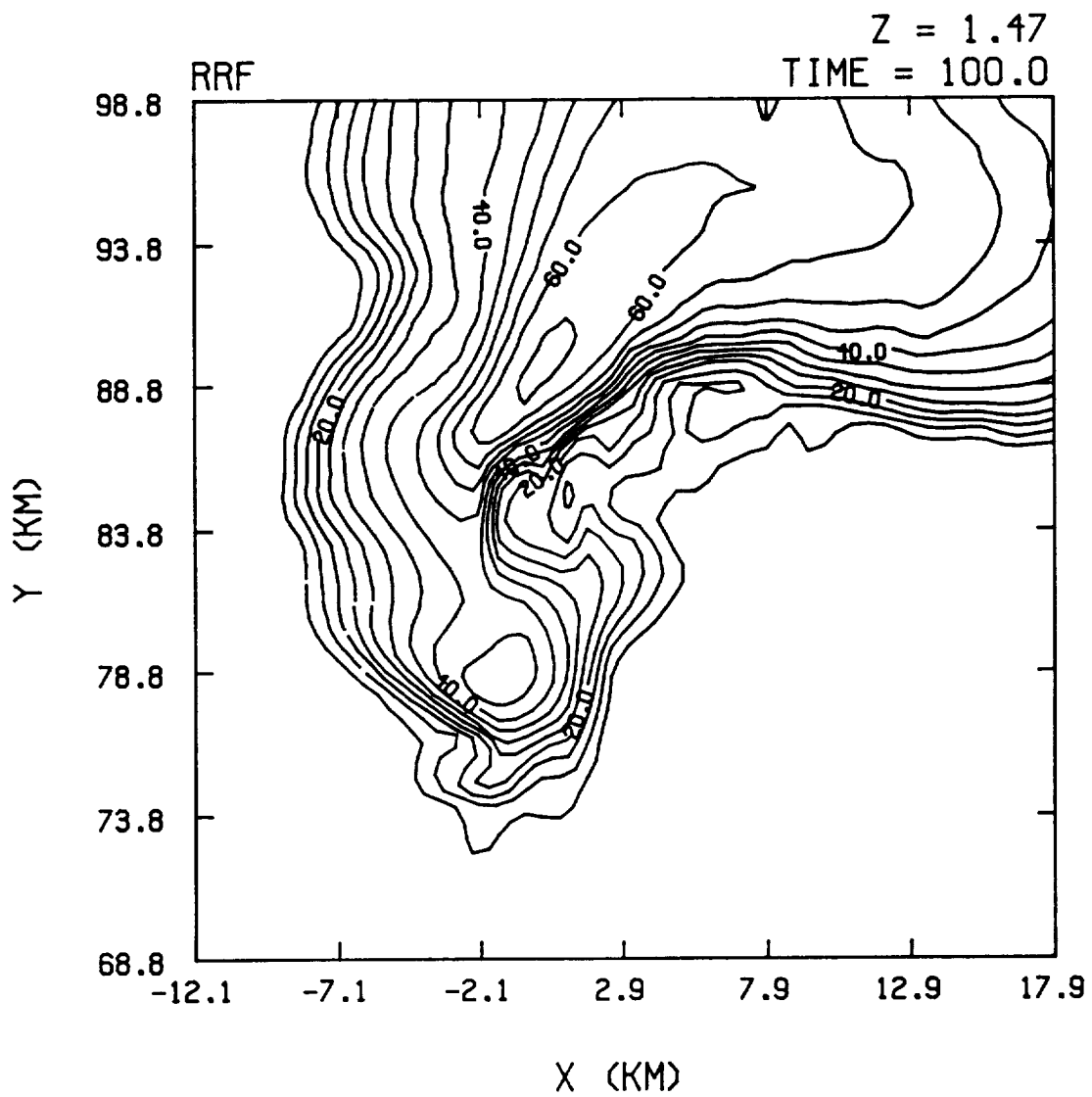


Fig. 41. Simulated radar reflectivity at 100 min and 1.5 km AGL for Case V. Area windowed to 30 km  $\times$  30 km. Contour interval is 5 dBZ.

Peak radar reflectivity of the modeled storm was in excess of 65 dBZ (e.g., Fig. 41). The modeled storm also produced hail at the ground. In comparison, the peak radar reflectivity of the observed Del City storm was less than 60 dBZ. However, at least one hailstorm with radar reflectivity in excess of 60 dBZ was observed during the 20 May outbreak (Ray et al., 1981).

A 3-D perspective of the modeled 35 dBZ reflectivity surface as viewed from the southeast is depicted in Fig. 42a. The radar reflectivity perspectives for the observed Del City storm (Figs. 42b and 42c) and the rainwater perspective for the Klemp et al. (1981) simulation (Fig. 42d) are shown for comparison. The overall structure of both of the model-simulated storms are very similar. Both are also comparable to the observed storm; they all exhibit a similar orientation of the hook echo and echo free vault. However, both model perspectives have greater upper-level overhang toward south than do the observed. This may be due to the fact that the northward component of the upper-level ambient winds is assumed too small. [Both model simulations assume nearly the same ambient wind profile.] A more intense northward component of the ambient winds between 6 - 12 km (as suggested by the 1330 CST Ft. Sill and the 1500 CST Oklahoma City sounding depicted in Fig. 4 of Ray et al., 1981) may have prevented the development of a southward overhang in the observed Del City storm.

Not unlike the simulations of Klemp et al. (1981) and Klemp and Rotunno (1983), the model could not resolve a tornado vortex; the horizontal grid size of 750 m is much too coarse. However, the model was able to simulate a region of peak low-level vorticity at the location (relative to the storm) where a tornado might have occurred. Fig. 43 shows a blow-up of the area surrounding the simulated low-level updraft at the time of peak low-level

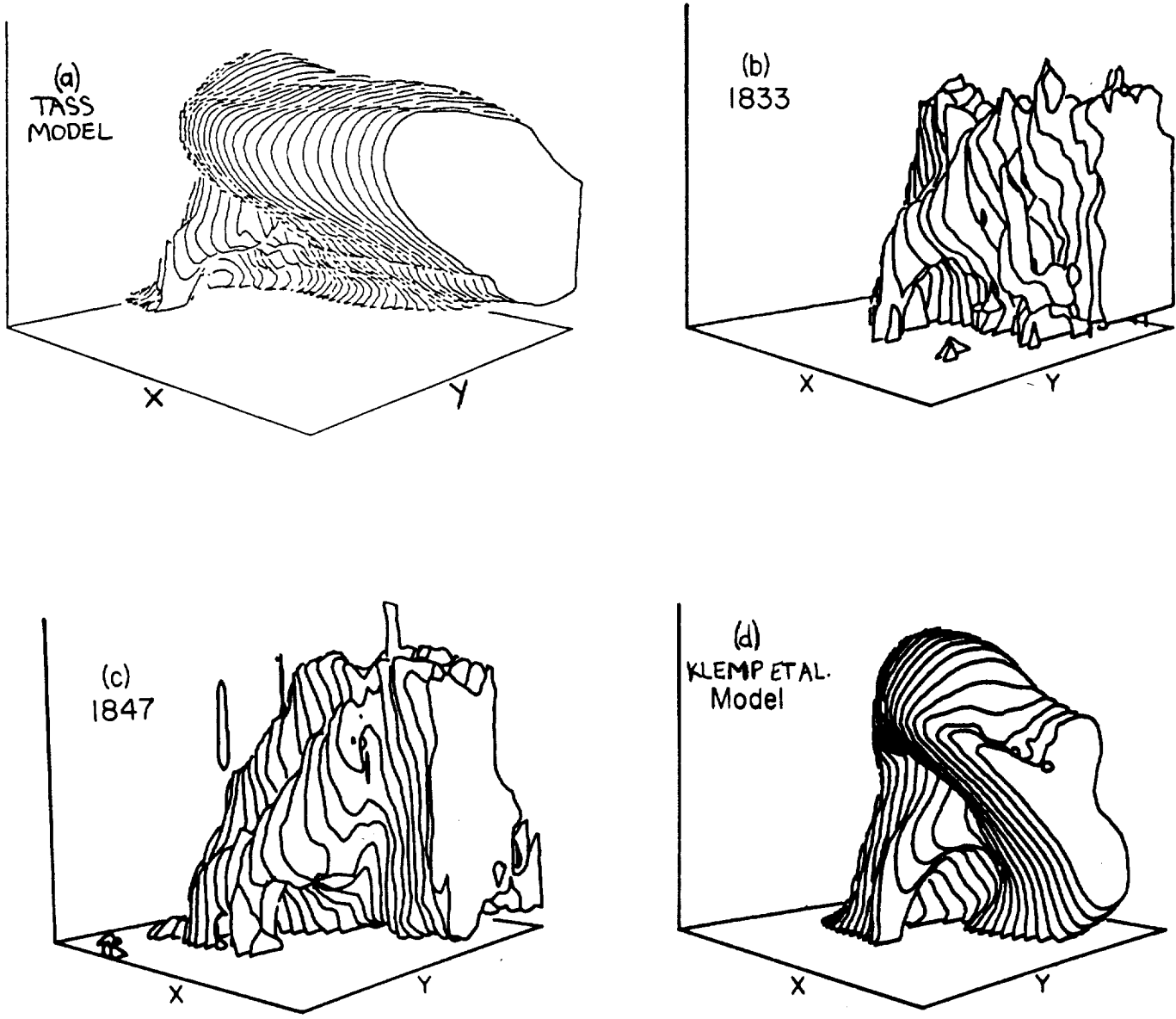


Fig. 42. Three-dimensional perspectives of the precipitation field within the modeled and observed storms as viewed from the southeast. The perspectives are (a) TASS model simulation, (b) Del City observed at 1833 CST, (c) Del City observed at 1847 CST, and (d) Klemp et al. (1981) model simulation. The contoured surfaces in (a)-(c) represent the 35 dBZ surface and in (d) represent the 0.5 g/kg rainwater surface. Figs. b-d are from Klemp et al. (1981).

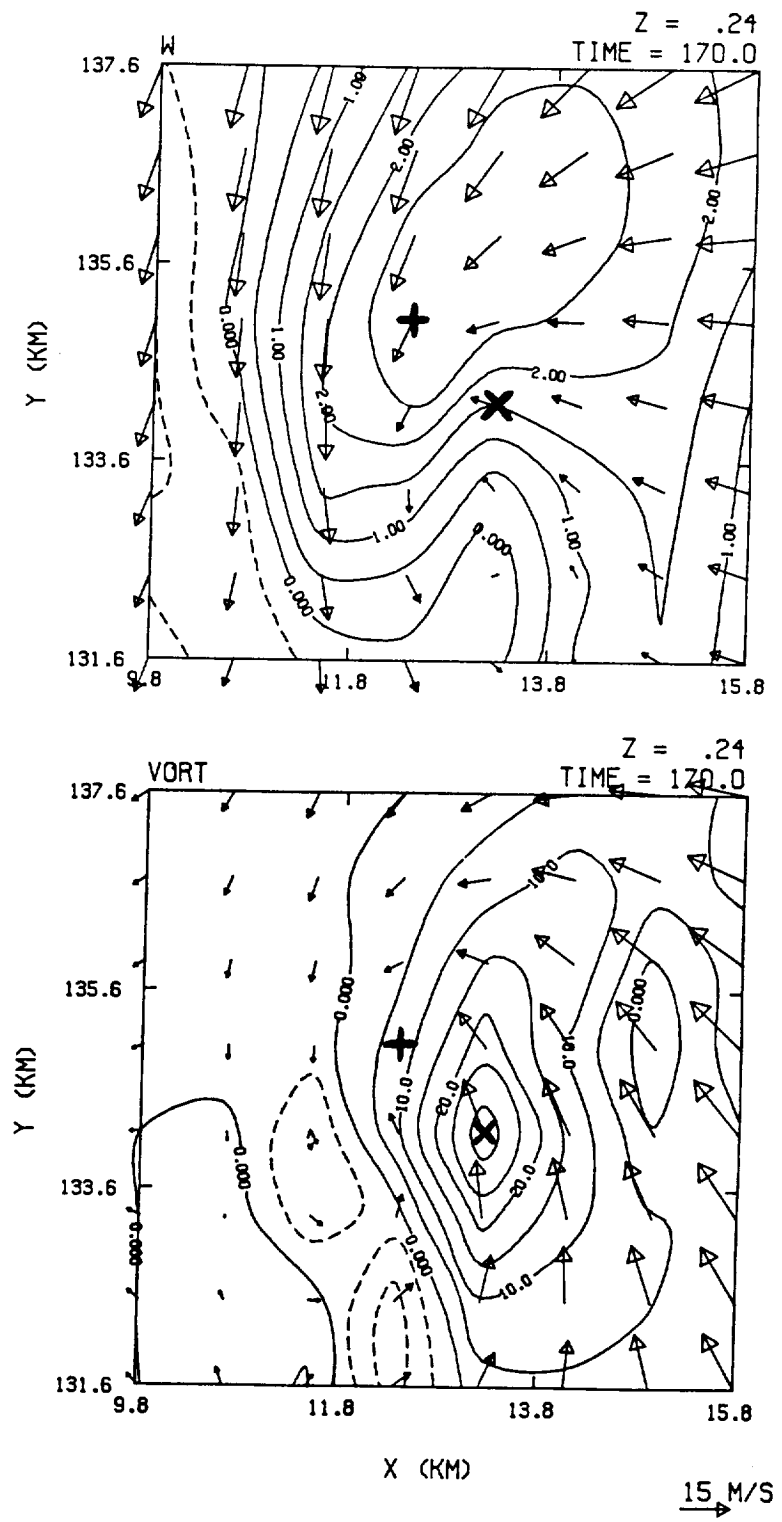


Fig. 43. Simulated low-level contour fields and superimposed wind vectors at 170 min for (a) vertical velocity and storm relative wind vectors, and (b) vertical vorticity and ground relative wind vectors for Case V. Area windowed to  $6 \text{ km} \times 6 \text{ km}$ . The contour interval for (a) is  $0.5 \text{ m s}^{-1}$ , and (b) is  $5 \times 10^{-2} \text{ s}^{-2}$ . Negative values contoured with a negative line. Labels in (b) scaled by a factor of 100. Vertical velocity peak designated by + and vorticity peak designated by x.

vorticity. Although barely resolved, the horseshoe-shaped structure of the updraft is apparent (Fig. 43a). This characteristic shape is due to the northward incursion of downdraft air just to the west of the flanking-line gust front. Fig. 43b shows that a peak vorticity of approximately  $3 \times 10^{-2} \text{ s}^{-1}$  is located southeast of the updraft peak. A horseshoe-shaped updraft structure and a vorticity center south to east of the updraft maximum was observed by Doppler radar at the time of tornadogenesis (Ray et al., 1981; Brandes, 1981, 1984).

Captured in the TASS simulation of this Case are cyclic phase changes in the quasi-steady structure of the mature storm. Fig. 44 shows the time history of the peak low-level vorticity and the height of the modeled storm top. The low-level vorticity attains peak values at roughly 70 min, 110 min, and 170 min; thus, the peak values are occurring at roughly 50 min ( $\pm 10$  min) intervals. Longlasting tornadic thunderstorms have been reported by Darkow and Roos (1970), Darkow (1971), and Fujita (1973) to produce tornadoes at periodic mean intervals of roughly 45 - 50 min. Fig. 44 also shows that the peak low-level vorticity occurs roughly 10 min after the storm top begins to collapse. Observed cases of storm top collapse preceding tornado formation have been reported by Fujita (1973), Fujita et al. (1976), and Umenhofer (1975). Umenhofer examined the overshooting tops in three tornadic thunderstorms and found that the tops commenced to collapse 6-21 min before associated tornadic events. Updraft weakening and storm collapse preceding tornado formation are also frequently observed in Doppler radar studies. Lemon and Doswell (1979) report that the strongest tornadoes, low-level winds, and downbursts occur during the collapse phase of supercell evolution.

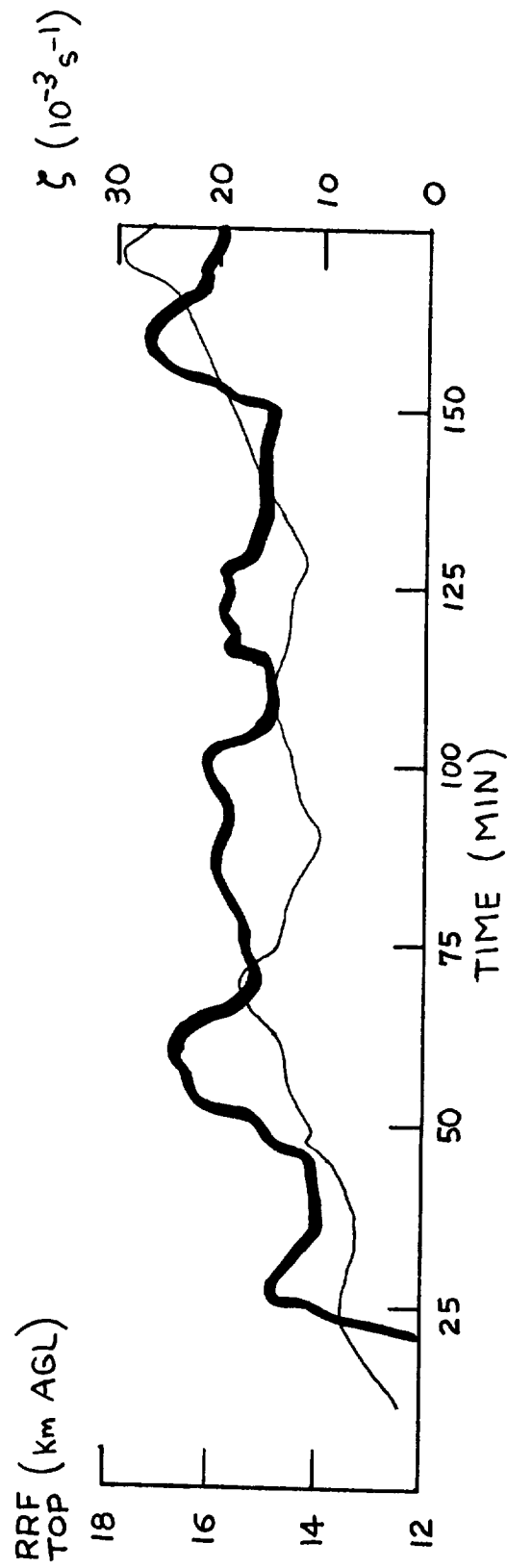


Fig. 44. Simulated time history of peak 10 dBZ radar reflectivity heights (thick curve) and peak low-level vertical vorticity (thin curve) for Case V.

Associated with the cyclic changes in the simulation of this Case are a forward bulging of the flanking-line gust front and an intensification of a downdraft located on the southwest side of the major storm updraft. The downdraft intensification and the pronounced bowing or forward bulging of the flanking-line gust front precede the time of the peak low-level vorticity. The forward bulging of the flanking-line gust front in the period preceding the vorticity peak at 170 min is shown in Fig. 45. [A similar change precedes the peaks at 70 min at 110 min.] Cyclic changes in the radar reflectivity also occur in the simulation. Immediately following the time of the low-level vorticity peak, the simulated mid-level hook echo (Fig. 46) completely wraps around the updraft, thus forming a doughnut shaped echo (Fujita, 1973) with a bounded weak echo region collocated with the updraft. [The change in the mid-level echo shown in Fig. 46 also reoccurs in both the previous and following cycles.] The cyclic nature of the simulated storm, however, was not apparent in the observed Del City storm. The Del City storm began to significantly weaken after the first collapse stage and later produced only one more tornado (Brandes, 1981). This discrepancy between model and observation may have resulted, because the actual storm was in, or moved into, a less unstable ambient environment. Unfortunately, the actual ambient conditions surrounding the Del City storm are unknown. The effect of the coarse grid resolution may also have a significant impact on the storm intensity and duration. A finer grid resolution would allow more intense circulations -- which in turn could greatly modify the vertical flow field. This effect was seen by Klemp and Rotunno (1983) by reducing the grid size by a factor of four in their simulation.

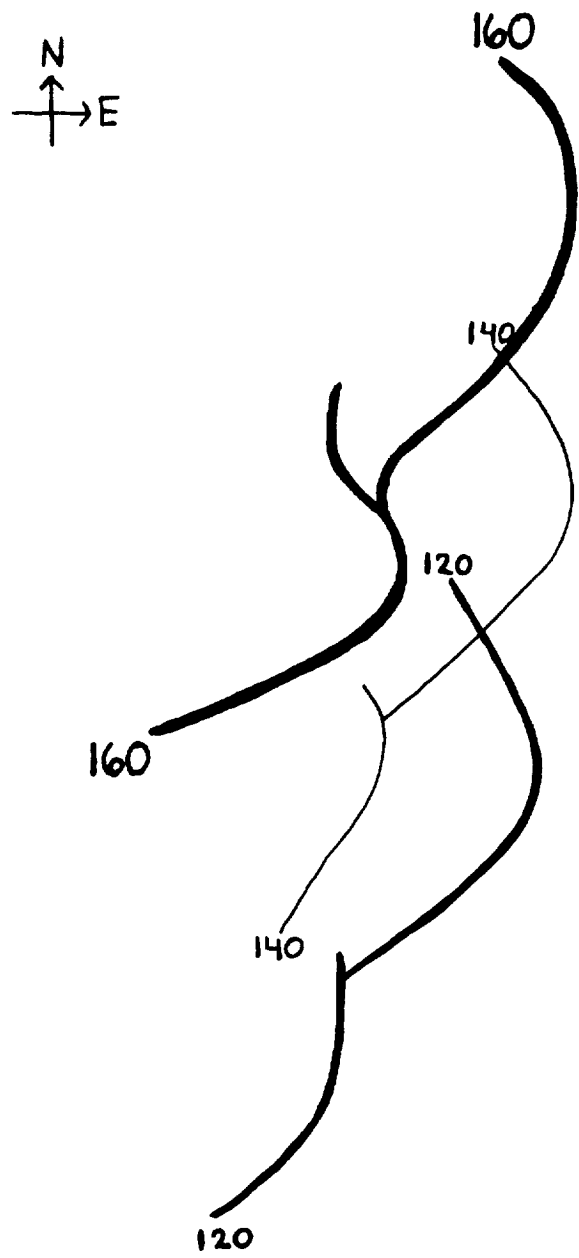


Fig. 45. Relative positions of simulated gust fronts at 120, 140, and 160 min in Case V.

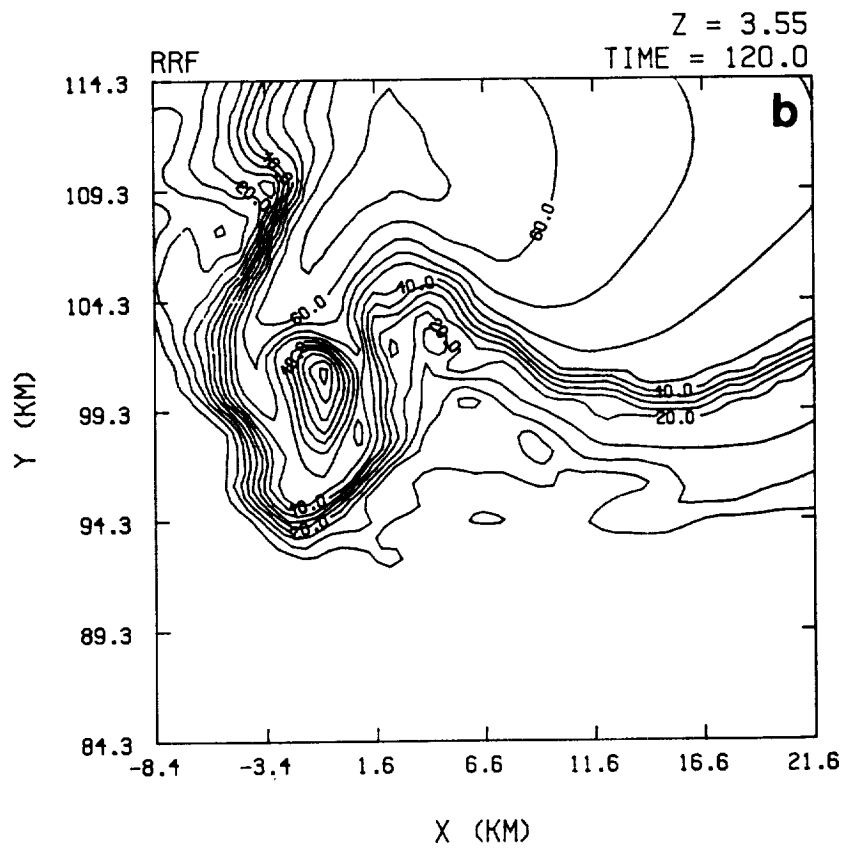
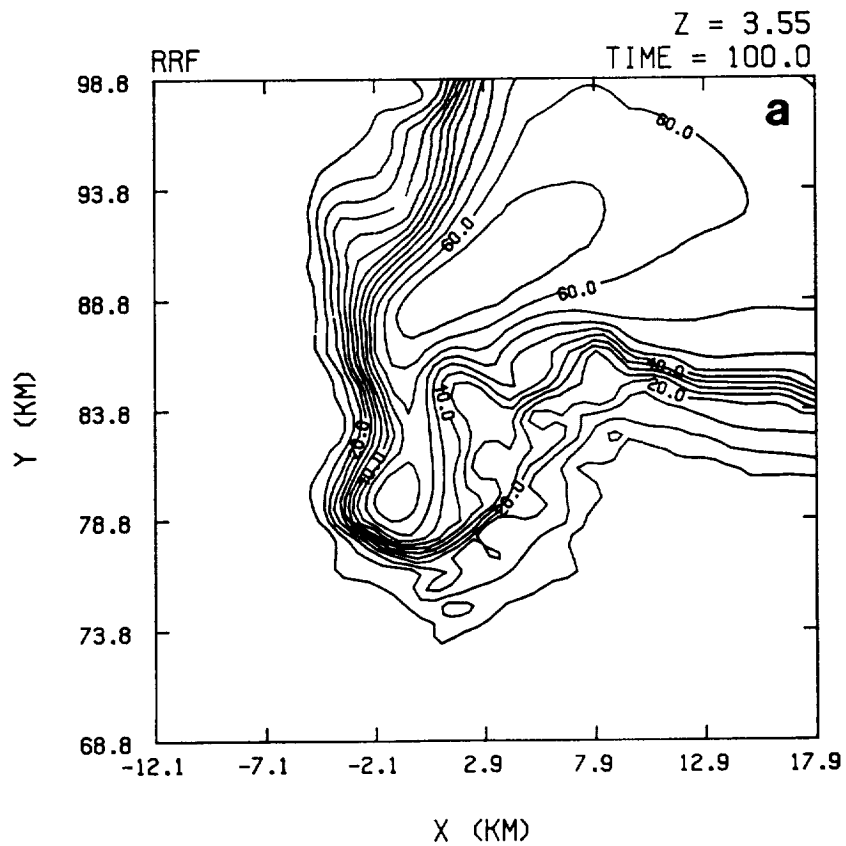


Fig. 46. Same as Fig. 41, but at 3.5 km AGL and at (a) 100 min and (b) 120 min.

### Summary for Case V

This case experiment was successful in simulating many of the features of a tornadic thunderstorm. Similarities with the observed Del City storm and the Klemp et al. (1981) simulation were noted. The modeled storm developed a persistent updraft, an echo free vault, BWER and a pronounced hook echo radar reflectivity structure. The low-level updraft developed a horseshoe-shaped structure at the time of peak low-level vorticity. This configuration occurred as downdraft air, moving in a cyclonically-curved path from the southwest, intruded into the updraft. The peak low-level vorticity occurred in the updraft region southeast of the updraft maximum, near the intrusion of downdraft air as is frequently observed in actual field studies.

The intensity of the modeled storm and its low-level vorticity field were cyclic once quasi-steady state was attained. Low-level vorticity peaks occurred at 70, 110, and 170 min. Each peak was preceded by: (1) the intensification of the southwestern downdraft, (2) a pronounced forward bulging of the flanking-line gust front, (3) a general weakening of the storm updraft, and (4) a collapse of the storm top. The latter occurred approximately 10 min prior to each of the low-level vorticity peaks. In the time following each of the vorticity peaks, the curvature of the flanking-line gust front decreased and the mid-level hook echo wrapped completely around the updraft. These structural changes in the storm reoccurred with each low-level vorticity peak in the simulation. Many of these cyclic changes have been observed in actual case studies.

## 7. SUMMARY AND CONCLUSIONS

In order to test and verify the Terminal Area Simulation System, five case experiments have been conducted. The numerical experiments were successful in simulating the following types of convective storms: (1) a long-lasting, High-Plains supercell hailstorm; (2) the life cycle of small High-Plains cumulonimbus; (3) an intense microburst producing cumulonimbus; (4) a multicell South Florida convective system; and (5) a tornadic Oklahoma supercell.

A comparison of each of these cases with available data allows us to answer each of the questions posed earlier.

Can the TASS model successfully simulate different modes of cumulonimbus convection? Yes; single-cell, multicell, and supercell storms were simulated.

Are the characteristic features of each storm type captured in the model simulation? Yes. The simulated single-cell storms began to dissipate soon after the precipitation reached the ground. The decay stage of the simulated single-cell storms was sometimes characterized by a trail of light precipitation falling from the remaining anvil cloud. The simulated multicell storm was characterized by the continuous development of new cells along the outflow boundary of the older cells. For supercells many of the actual characteristic features were simulated. For instance, the visual features which were simulated include: wall cloud, flanking-line towers, forward line cumulus, and an extensive overhanging anvil. The radar reflectivity features of a supercell which were simulated include: hook echo, echo free vault, BWER, V notch, streamer, and overhanging echo curtain. And, the kinematic features of a supercell storm which were simulated include: giant quasi-steady and undiluted updraft, rear-flank and

forward flank downdraft, forward-line and flanking-line gust fronts, and a mesocyclone.

How accurate are the storm fields simulated? Are the simulated fields consistent with observed data both aloft and near the ground? Although the simulated fields did not always exactly match the observed field, the comparisons were very reasonable. The DFW microburst simulation (Case III) produced strong low-level outflows; and the expansion of the microburst outflow matched available observed data surprisingly well. Temperatures in low-level outflow for Cases III and IV were consistent with sparse observed data. More accurate ambient data, better initial conditions, and a nonpassive interaction with the large-scale through a mesoscale model, could possibly improve the agreement between simulation and observation.

Is hail simulated at the ground when it is actually observed, and vice versa? Does the model not simulate hail at the ground when it is not observed? There are probably an insufficient number of cases in order to judge how well the model predicts hail at the ground. Hail was simulated at the ground for the CCOPE Supercell Hailstorm, and the DFW Microburst, as was confirmed by observations; and no hail was simulated at the ground for the South Florida Convective Complex, as also confirmed by observations. However, hail at the ground was simulated for the Oklahoma Tornadoic Thunderstorm, even though hail was not indicated in at least two of the observed tornadoic thunderstorms.

When simulating severe storms, can associated severe phenomena, such as downbursts, strong winds, and tornadoes be simulated? In spite of the coarse grid mesh used in these case studies, the model quite successfully simulated downbursts and strong low-level winds. But, as was true in the simulation by Klemp et al. (1981) and Klemp and Rotunno (1983), the grid size

was too coarse in order to resolve a tornado. The model did simulate a horseshoe-shaped updraft and peak low-level vorticity in the correct relative position to the updraft as is often observed in tornadic situations.

Does the model simulate the direction and speed of storm propagation correctly? Is the orientation and speed of propagation correct for the storm-induced gust fronts? The propagation of the simulated storms and gust fronts, and the orientation of the gust fronts compared very well with observations.

Does the model properly simulate the duration and life cycles of cumulonimbus convection? In the case experiments either short-lived storms or long-lived storms were produced, as was consistent with observations. The modeled long-lived storms did not prematurely decay. The simulated life cycle of the short-lived storm in Case II was consistent with the observed life cycle.

Are there any periodic tendencies or trends in the simulation of long-duration storms? Both the COOPE Supercell Hailstorm and the Tornadic Oklahoma Thunderstorm achieved a quasi-steady state, but possessed cyclic changes in intensity and structure. The cyclic character of the latter case produced low-level vorticity peaks at roughly 50 min intervals. Each of these peaks were preceded by a weakening of the storm updraft, a collapse of the storm top, an intensification of the right-flank downdraft, and a pronounced forward bulging of the flanking-line gust front. In the period immediately following each of the vorticity peaks, the curvature of the flanking-line gust front decreased and the mid-level hook echo wrapped completely around the updraft. All of these events reoccurred with each

low-level vorticity peak. Other studies have found many of these cyclic features in association with tornadogenesis (e.g., Lemon and Doswell, 1979).

How stable is the TASS model; does it remain numerically stable for long integrations? Are there any anomalous trends, such as in the pressure deviation field? Do the simulated results diverge from the observed data as the lifetime of the storm increases? Do the fields remain bounded? In two of the cases which involved long-lasting storms, the simulations occurred over several hours of model time (Case I lasting 4 1/3 hours). No anomalous trends or noncyclic patterns were detected in any of the simulations. The model remained numerically stable and the simulated fields maintained their quasi-steady structure. Also, at no time during the integration did we make any external adjustments, such as to the pressure field.

How do simulations with the TASS model compare to simulations with other numerical models? Although no rigorous comparison with any other model has been attempted, we do find that results from the TASS model appear roughly similar to those obtained with the Klemp-Wilhelmson (1978) model. In fact, the TASS results appear more similar to those obtained with the Klemp-Wilhelmson model than those obtained with the Colorado State University three-dimensional cloud/mesoscale model (Cotton et al., 1982; Tripoli and Cotton, 1982), even though the latter includes ice phase parameterization, while the former does not.

This report shows that the TASS model can be applied with reasonable success to a variety of cloud simulation problems.

#### ACKNOWLEDGMENTS

The work reported herein was primarily supported by the National Aeronautics and Space Administration under contract NAS1-17409. The work was performed at the Langley Research Center in Hampton, Virginia, under the direction of Dr. Roland Bowles of the Flight Management Branch. Additional support was provided by the Defense Nuclear Agency through an inter-agency agreement with NASA under contract NAS1-17661.

I would like to express special appreciation to Ms. Mary Bousquet for producing and preparing most of the figures, and Ms. Mary Edwards for typing the report. Also I would like to acknowledge my colleagues, Dr. Mike Kaplan, Ms. Pamela Price, and Dr. V. Mohan Karvampudi of MESO, Inc., for reviewing this manuscript.

Rawinsonde data for the CCOPE cases were provided by the Bureau of Reclamation, Denver, CO. The 25 August 1975 FOS special sounding, which was observed during the FACE project, was kindly provided by John B. Cuning of NOAA. Model computations were carried out on the NASA Langley CYBER VPS 32.

## REFERENCES

- Bedard, A. J., Jr., 1984: Optimizing the use of surface sensors for wind shear detection, J. Aircraft, 21, 971-977.
- Bedard, A. J., Jr., and T. J. LeFebvre, 1986: Surface measurements of gust fronts and microbursts during the JAWS project: Statistical results and implications for wind shear detection, prediction, and modeling, NOAA Technical Memorandum ERL WPL-135, Wave Propagation Laboratory, Boulder, Colorado, 112 pp.
- Brandes, E. A., 1981: Fine structure of the Del City-Edmond tornado meso-circulation, Mon. Wea. Rev., 109, 635-647.
- Brandes, E. A., 1984: Vertical vorticity generation and mesocyclone sustenance in tornadic thunderstorm: The observational evidence, Mon. Wea. Rev., 112, 2253-2269.
- Browning, K. A., 1964: Airflow and precipitation trajectories within severe local storms which travel to the right of the winds, J. Atmos. Sci., 21, 634-639.
- Browning, K. A., and R. J. Donaldson, Jr., 1963: Airflow and structure of a tornadic storm, J. Atmos. Sci., 20, 533-545.
- Byers, H. R., and R. R. Braham, Jr., 1949: The Thunderstorm, U.S. Government Printing Office, Washington, DC, 287 pp.
- Chisholm, A. J., 1973: Radar case studies and airflow models, Alberta Hailstorms, Meteor. Monogr., No. 36, Amer. Meteor. Soc., 1-36.

- Chuang, S., F. H. Proctor, J. W. Zack, and M. L. Kaplan, 1984: A numerical weather prediction system designed to simulate atmospheric downburst phenomena, AIAA 22nd Aerospace Science Meeting, AIAA-84-0352, Reno, Nevada, 15 pp.
- Cotton, W. R., M. A. Stephens, T. Nehr Korn, and G. J. Tripoli, 1982: The Colorado State University three-dimensional cloud/mesoscale model - 1982. Part II: An ice phase parameterization, J. de Rech. Atmos., 16, 295-320.
- Cunning, J. B., and M. DeMaria, 1986a: An investigation of the development of mesoscale convective systems. Part I: Boundary layer interactions, Mon. Wea. Rev., 114, 5-24.
- Cunning, J. B., M. DeMaria, and H. W. Poor, 1986b: An investigation of the development of cumulonimbus systems over south Florida. Part II: In-cloud structure, Mon. Wea. Rev., 114, 25-39.
- Daily Press (Newport News, Virginia), 1985: Relatives helping ID crash victims, 90th yr., no. A1, Aug. 4, 1985, pp. 1,4.
- Darkow, G. L., 1971: Periodic tornado production by long-lived parent thunderstorms, Preprints, 7th Conference on Severe Local Storms, Kansas City, Amer. Meteor. Soc., 194-197.
- Darkow, G. L., and J. C. Roos, 1970: Multiple tornado producing thunderstorms and their apparent cyclic variations in intensity, Preprints, 14th Radar Met. Conf., Amer. Meteor. Soc., 305-308.

- Dye, J. E., J. J. Jones, W. P. Winn, T. A. Cerni, B. Gardiner, D. Lamb, R. L. Pitter, J. Hallett, and C. P. R. Saunders, 1986: Early electrification and precipitation development in a small isolated Montana cumulonimbus, J. Geophys. Res., 91, 1231-1246.
- Fujita, T. T., 1973: Proposed mechanism of tornado formation from rotating thunderstorms, Preprints, 8th Conf. on Severe Local Storms, Denver, Amer. Meteor. Soc., 131-136.
- Fujita, T. T., 1981: Tornadoes and downbursts in the context of generalized planetary scales, J. Atmos. Sci., 38, 1511-1534.
- Fujita, T. T., 1986: DFW Microburst on August 2, 1985, Satellite and Mesometeorology Research Project, Dept. Geophysical Sciences, University of Chicago, 154 pp.
- Fujita, T. T., G. S. Forbes, and T. A. Umenhofer, 1976: Close-up view of 20 March 1976 tornadoes: Sinking cloud tops to suction vortices. Weatherwise, 29, 116-131, 145.
- Fujita, T. T., and R. M. Wakimoto, 1983: JAWS microburst revealed by triple-Doppler radar, Preprints, 13th Conf. on Severe Local Storms, Tulsa, Amer. Meteor. Soc., 97-100.
- Johnson, B. C., and E. A. Brandes, 1986: A study of barrier effects and shed eddy phenomenon associated with supercells, Preprints, Joint Session of 23rd Conf. on Radar Meteor. and Conf. on Cloud Physics, Snowmass, Co., Amer. Meteor. Soc., J65-J68.

- Johnson, K. W., 1985: The role of surface observations in defining the lower boundary condition for multiple-Doppler analysis, Preprints, 14th Conf. on Severe Local Storms, Indianapolis, Amer. Meteor. Soc., 44-47.
- Kaplan, M. L., J. W. Zack, V. C. Wong, and J. J. Tuccillo, 1982: Initial results from a Mesoscale Atmospheric Simulation System and comparison with the AVE-SESAME I data set, Mon. Wea. Rev., 110, 1564-1590.
- Klemp, J. B., and R. Rotunno, 1983: A study of the tornadic region within a supercell thunderstorm, J. Atmos. Sci., 40, 359-377.
- Klemp, J. B., and R. B. Wilhelmson, 1978: The simulation of three-dimensional convective storm dynamics, J. Atmos. Sci., 35, 1070-1096.
- Klemp, J. B., R. B. Wilhelmson, and P. S. Ray, 1981: Observed and numerically simulated structure of a mature supercell thunderstorm, J. Atmos. Sci., 38, 1558-1580.
- Knight, C. A. (Ed.), 1982: The Cooperative Convective Precipitation Experiment (CCOPE), 18 May - 7 August 1981, Bull. Amer. Meteor. Soc., 63, 386-398.
- Knight, C. A., M. B. Baker, G. M. Barnes, G. B. Foote, M. A. LeMone, and G. Vali, 1985: Summary of a meeting on the analysis and interpretation of CCOPE data, 1-4 October 1984, Boulder, Colorado, Bull. Amer. Meteor. Soc., 66, 663-667.

- Lemon, L. R., and C. A. Doswell III, 1979: Severe thunderstorm evolution and mesocyclone structure as related to tornadogenesis, Mon. Wea. Rev., 107, 1184-1197.
- Levy, G., and W. R. Cotton, 1984: A numerical investigation of mechanisms linking glaciation of the ice-phase to the boundary layer, J. Climate Appl. Meteor., 23, 1505-1519.
- Marwitz, J. D., 1972a: The structure and motion of severe hailstorms. Part I: Supercell storms, J. Appl. Meteor., 11, 166-179.
- Marwitz, J. D., 1972b: The structure and motion of severe hailstorms. Part II. Multi-cell storms, J. Appl. Meteor., 11, 180-188.
- Miller, L. J., 1985: The CCOPE hailstorm of 2 August 1981. International Cloud Modeling Workshop, Irsee, Federal Republic of Germany, World Meteor. Soc., 8 pp.
- Musil, D. J., A. J. Heymsfield, and P. L. Smith, 1986: Microphysical characteristics of a well-developed weak echo region in a High Plains supercell thunderstorm, J. Climate Appl. Meteor., 25, 1037-1051.
- Proctor, F. H., 1985a: Numerical simulation of precipitation induced downbursts, Second Int. Conf. on the Aviation Weather System, Montreal, Canada, Amer. Meteor. Soc., 257-264.
- Proctor, F. H., 1985b: Three-dimensional simulation of the 2 August CCOPE hailstorm with the Terminal Area Simulation System, Int. Cloud Modeling Workshop/Conf., Irsee, FRG, World Meteor. Soc., 14 pp.

- Proctor, F. H., 1987: The Terminal Area Simulation System. Volume I: Theoretical formulation, NASA CR-4046.
- Ray, P. S., B. C. Johnson, K. W. Johnson, J. S. Bradberry, J. J. Stephens, K. K. Wagner, R. B. Wilhelmson, and J. B. Klemp, 1981: The morphology of several tornadic storms on 20 May 1977, J. Atmos. Sci., 38, 1643-1663.
- Rotunno, R., and J. B. Klemp, 1985: On the rotation and propagation of simulated supercell thunderstorms. J. Atmos. Sci., 42, 271-292.
- Salottolo, G. D., 1985: Meteorological factual report of the accident involving Delta Air Lines, Inc., Lockheed 1011, N726DA, Dallas/Fort Worth International Airport, August 2, 1985, National Transportation Safety Board, Bureau of Technology, Washington, D.C., 29 pp.
- Sax, R. I., and J. G. Hudson, 1981: Continentality of the South Florida summertime CCN aerosol, J. Atmos. Sci., 38, 1467-1479.
- Tripoli, G. J., and W. R. Cotton, 1982: Colorado State University three-dimensional cloud/mesoscale model, 1982: Pt. 1, General theoretical framework and sensitivity experiments, J. de Rech. Atmos., 16, 185-219.
- Tripoli, G. J., and W. R. Cotton, 1986: An intense, quasi-steady thunderstorm over mountainous terrain. Part IV: Three-dimensional numerical simulation, J. Atmos. Sci., 43, 894-912.
- Umenhofer, T. A., 1975: Overshooting top behavior of three tornado-producing thunderstorms, Preprints, 9th Conf. on Severe Local Storms, Norman, OK, Amer. Meteor. Soc., 96-99.

Wade, C. G., 1982: A preliminary study of an intense thunderstorm which moved across the CCOPE research network in southeastern Montana, Preprints, 9th Conf. on Forecasting and Analysis, Seattle, Amer. Meteor. Soc., 388-395.

Weisman, M. L., and J. B. Klemp, 1982: The dependence of numerically simulated convective storms on vertical wind shear and buoyancy, Mon. Wea. Rev., 110, 504-520.

Weisman, M., and J. Klemp, 1984: The structure and classification of numerically simulated convective storms in directionally varying wind shears, Mon. Wea. Rev., 112, 2479-2498.

Weisman, M. L., J. B. Klemp, and J. Wilson, 1983a: Dynamic interpretation of notches, WERS, and mesocyclones simulated in a numerical cloud model. Preprints, 21st Conf. on Radar Meteor., Edmonton, Alberta, Amer. Meteor. Soc.

Weisman, M. L., J. B. Klemp, and L. J. Miller, 1983b: Modeling and Doppler analysis of the CCOPE August 2 supercell storm, Preprints, 13th Conf. on Severe Local Storms, Tulsa, Oklahoma, Amer. Meteor. Soc., 223-226.

Wilson, J. W., R. D. Roberts, C. Kessinger, and J. McCarthy, 1984: Microburst wind structure and evaluation of Doppler radar for airport wind shear detection, J. Clim. Appl. Meteorol., 23, 898-915.

Standard Bibliographic Page

1. Report No. DOT/FAA/PM-86/50, II NASA CR-4047		2. Government Accession No.		3. Recipient's Catalog No.	
4. Title and Subtitle The Terminal Area Simulation System Volume II: Verification Cases				5. Report Date April 1987	
				6. Performing Organization Code	
7. Author(s) F. H. Proctor				8. Performing Organization Report No.	
				10. Work Unit No.	
9. Performing Organization Name and Address ST Systems Corporation (STX) 17 Research Drive Hampton, VA 23666				11. Contract or Grant No. NAS1-17409	
				13. Type of Report and Period Covered Contractor Report	
12. Sponsoring Agency Name and Address National Aeronautics and U.S. Dept. of Transportation Space Administration and Federal Aviation Admin. Washington, DC 20546 Washington, DC 20591				14. Sponsoring Agency Code 505-67-41	
				13. Type of Report and Period Covered Contractor Report	
15. Supplementary Notes ST Systems Corporation (STX) formerly SASC Technologies, Inc. Langley Technical Monitor: Roland L. Bowles F. H. Proctor: MESO, Inc., Hampton, Virginia. Prepared under subcontract 85-6000-A1603. Volume I: NASA CR-4046					
16. Abstract The numerical simulation of five case studies are presented and are compared with available data in order to verify the three-dimensional version of the Terminal Area Simulation System (TASS). A spectrum of convective storm types are selected for the case studies. They are: (1) a High-Plains supercell hailstorm, (2) a small and relatively short-lived High-Plains cumulonimbus, (3) a convective storm which produced the 2 August 1985 DFW microburst, (4) a South Florida convective complex, and (5) a tornadic Oklahoma thunderstorm. For each of the cases the model results compared reasonably well with observed data. In the simulations of the supercell storms many of their characteristic features were modeled, such as the hook echo, BWER, mesocyclone, gust fronts, giant persistent updraft, wall cloud, flanking-line towers, anvil and radar reflectivity overhang, and rightward veering in the storm propagation. Also in the simulated supercell storms, heavy precipitation including hail fell to the west and north of the storm updraft. In the simulation of the tornadic storm a horseshoe-shaped updraft configuration and cyclic changes in storm intensity and structure were noted. The simulation of the DFW microburst agreed remarkably well with sparse observed data. The simulated outflow rapidly expanded in a nearly symmetrical pattern and was associated with a ring vortex. A South Florida convective complex was simulated and contained updrafts and downdrafts in the form of discrete bubbles. The numerical simulations, in all cases, always remained stable and bounded with no anomalous trends.					
17. Key Words (Suggested by Authors(s)) Numerical cloud model Cumulus convection Tornadic Hailstorms thunderstorm Supercell storms Gust fronts Downbursts Microburst Wind shear Convective complex				18. Distribution Statement  Unclassified - Unlimited  Subject Category 03	
19. Security Classif.(of this report) Unclassified		20. Security Classif.(of this page) Unclassified		21. No. of Pages 112	22. Price A06